Synthetic hackmanites as detection materials for ionizing radiation

Master's thesis
Sami Vuori
Inorganic Materials Chemistry Group
Department of Chemistry
University of Turku
June 2019
Supervisor: Mika Lastusaari

Abstract

UNIVERSITY OF TURKU

Faculty of Science and Engineering, Department of Chemistry, Laboratory of Materials Chemistry and Chemical Analysis

VUORI, SAMI: Synthetic hackmanites as detection materials for ionizing radiation

Master's thesis, 92 p.

June 2019

Hackmanite ($Na_8Al_6Si_6O_{24}(Cl,S)_2$) exhibits reversible photochromism or tenebrescence (Latin *tenebra*, shadow), which can be induced by exposure to UV light. In this phenomenon the off-white mineral turns pink or purple, and the original color can be restored with visible light or heat. For this to happen, there must be traps in the material's crystal structure, and in hackmanite the traps are chloride vacancies which are sites where a chloride ion should reside, but due to sulfur anions being present, the charge balance does not allow a chloride ion to enter the structure at some point near the sulfur ion. The incident UV photon excites a sulfur atom's electron which gets trapped in the vacancy. This creates an F center (German *Farbzentrum*, color center) which absorbs visible light in the green-yellow part (520−540 nm) of the spectrum, causing the coloration of the material.

The aim of this study was to gain knowledge on how particle radiation, exposure to X-rays and gamma radiation induce tenebrescence in hackmanites. The theoretical background reviews different types of radiation, current trends in radiation dosimetry and the use of thermoluminescence and optically stimulated luminescence in the ionizing radiation monitoring. Some theory about color spaces and representation models are discussed shortly. Finally, the X-ray analysis techniques used in the experimental section are reviewed.

The experimental section focuses on the synthetically prepared hackmanite to gain knowledge on whether the material could be used as a novel application in the field of radiation detection and dosimetry. The section also contains specific instructions on how to make hackmanites and cast them as flexible tapes via the doctor blading method.

Keywords: chemistry, tenebrescence, photochromism, X-ray, tape casting, hackmanite

Tiivistelmä

TURUN YLIOPISTO
Luonnontieteiden ja tekniikan tiedekunta, Kemian laitos, Materiaalikemian ja kemiallisen analyysin laboratorio

VUORI, SAMI: Synteettiset hackmaniitit ionisoivan säteilyn havaitsemismateriaaleina
Pro gradu -tutkielma, 92 s.
Kesäkuu 2019

Hackmaniitti ($Na_8Al_6Si_6O_{24}(Cl,S)_2$) on mineraali, jolla on erityinen UV-valon avulla aikaansaatava värinvaihto-ominaisuus, josta käytetään nimitystä palautuva fotokromismi tai tenebresenssi (lat. *tenebra*, varjo). Ilmiössä vaalean värinen mineraali vaihtaa väriään pinkiksi tai violetiksi, ja se voidaan palauttaa takaisin alkuperäiseen väriinsä näkyvällä valolla tai lämmöllä. Tenebresenssiä varten täytyy materiaalin kiderakenteessa olla loukkuja, ja hackmaniitissa ne ovat kloridivakansseja eli paikkoja, joissa normaalisti sijaitsisi klooriatomi, mutta ei lähellä sijaitsevan rikin vuoksi varaustasapainon vallitessa ole. Rikki-ioniin kohdistuva UV-fotoni virittää sen elektronin, joka loukkuuntuu kloridivakanssiin. Tämä luo vakanssiin F-keskuksen (saks. *Farbzentrum*, värikeskus), joka absorboi näkyvää valoa keltavihreällä alueella (n. 520−540 nm) ja aiheuttaa materiaalin värin.

Tutkielmassa tutkittiin hackmaniitissa tavattavaa tenebresenssiä hiukkas-, röntgen- ja gammasäteilyaltistuksessa. Teoreettisesta pohjatietoa avaavassa kappaleessa käydään läpi erilaisia säteilylajeja, dosimetrian nykysovelluksia ja termoluminesenssin ja optisesti stimuloidun luminesenssin käyttöä ionisoivan säteilyn havaitsemisessa. Myös väriavaruuksia ja värien esittämistapoja käsitellään lyhyesti. Kappaleen lopussa on myös katsaus tutkielman kokeellisessa osassa hyödynnettyihin röntgenanalyysitekniikoihin.

Kokeellinen osuus keskittyy synteettisen hackmaniitin valmistusmenetelmiin ja taipuisaksi kalvoksi valamiseen. Säteilyaltistusmittaukset pureutuvat pääosin siihen, miten hyvin hackmaniitit soveltuvat säteilylajien havaitsemiseen ja säteilyannosmittauksiin.

Asiasanat: kemia, tenebresenssi, fotokromismi, röntgen, tape casting, hackmaniitti

Table of Contents

Preface

The measurements included in this thesis were conducted in the Laboratory of Materials Chemistry and Chemical Analysis at the University of Turku and as a cooperation project with Karlsruhe Institute of Technology (KIT) in Karlsruhe, Germany. Business Finland provided financial aid for the project. Without the funding the thesis would not have included the broad range of measurements described in the experimental section.

I want to thank my thesis advisor, adjunct professor Mika Lastusaari for his untiring helpfulness, prompt replies to my emails, the fruitful brainstorming sessions in the lab and most of all for believing in me to the extent that I got to experience a trip to a synchrotron facility in Germany.

The second part of the thanks go to Dr. Isabella Norrbo who originally introduced me to the world of hackmanites in the lab, has been a positive spirit throughout the whole thesis process and knows everything about everything I have asked.

This thesis was completed on the same date when Finland won the World Championship in ice hockey. Way to go, Leijonat.

Abbreviations

□	vacancy
a.u.	Arbitrary unit
D	absorbed dose
DC	direct current
DSLR	Digital single-lens reflex camera
FW	firmware
I	current, intensity
IR	Infrared
KIT	Karlsruhe Institute of Technology
P	power
pp	percentage point
RGB	Red, green, blue
SEM	Scanning electron microscopy
TEM	Transmission electron microscopy
U	voltage
UV	Ultraviolet
XANES	X-ray absorption near-edge structure
XRD	X-ray diffraction
XRF	X-ray fluorescence
XPS	X-ray photoelectron spectroscopy

1. Introduction

Although the Universe is full of different types of radiation, humans can sense only a small part of the electromagnetic spectrum. We see the visible light, we feel the infrared photons as a warm sensation on our skin, yet we have very limited means to sense ionizing radiation as we have not evolved to feel X-rays or gamma rays. This is why we need to rely on materials that are able to sense ionizing radiation before the levels create a stochastic risk or a direct radiation hazard.

Different types of dosimeters have been invented for ionizing radiation, with the most important ones being electronic ones that are constantly monitoring the radiation levels, but also long exposure personal dosimeters that can store the radiation energy for long periods of time and be read with a specific instrument are used on a daily basis for occupational risk assessments and monitoring.

Hackmanites ($Na_8Al_6Si_6O_{24}Cl_{2-2x},S_x\square_x$ where x is typically ~0.1) are sulfur-containing variations of minerals that belong to the sodalite ($Na_8Al_6Si_6O_{24}Cl_2$) family [1, 2]. The earliest record of their existence is from 1834 [3], but the research started from 1920s [4]. The number of publications has been scarce, considering the exciting properties they possess. However, in 2010s Norrbo *et al.* have been investigating their properties and characteristics comprehensively. Hackmanites are materials exhibiting persistent luminescence with long fading times, and also reversible photochromism, also known as tenebrescence (Latin *tenebra*, "shadow") which appears as purple or pink coloration upon exposure to UV light. They can thus be considered as magnificent materials for novel optical solutions. [5-7]

One example of inorganic photochromism is a phenomenon which is based on electrons being excited from an atom to traps in a solid material's lattice. The traps can be crystal defects, impurities or other lattice-related anomalies with energy levels residing in the forbidden gap between the valence band and the conduction band. An electron entering the trap creates an F center (German *Farbzentrum*, "color center") which absorbs wavelengths in the visible light region, causing the material's coloration. The electron can be freed from the trap either with heat or light but stays trapped if the material is not exposed to light in room temperature. [7]

2. Theoretical background

2.1. Ionizing radiation

According to International Union of Pure and Applied Chemistry (IUPAC), radiation is defined as "a term embracing electromagnetic waves as well as fast moving particles" [8], thus including the photons and particles. Ionizing radiation is the species of radiation that is able to ionize compounds, i.e. detach electrons from atoms. The electromagnetic spectrum showing all electromagnetic radiation is depicted in Figure 1.

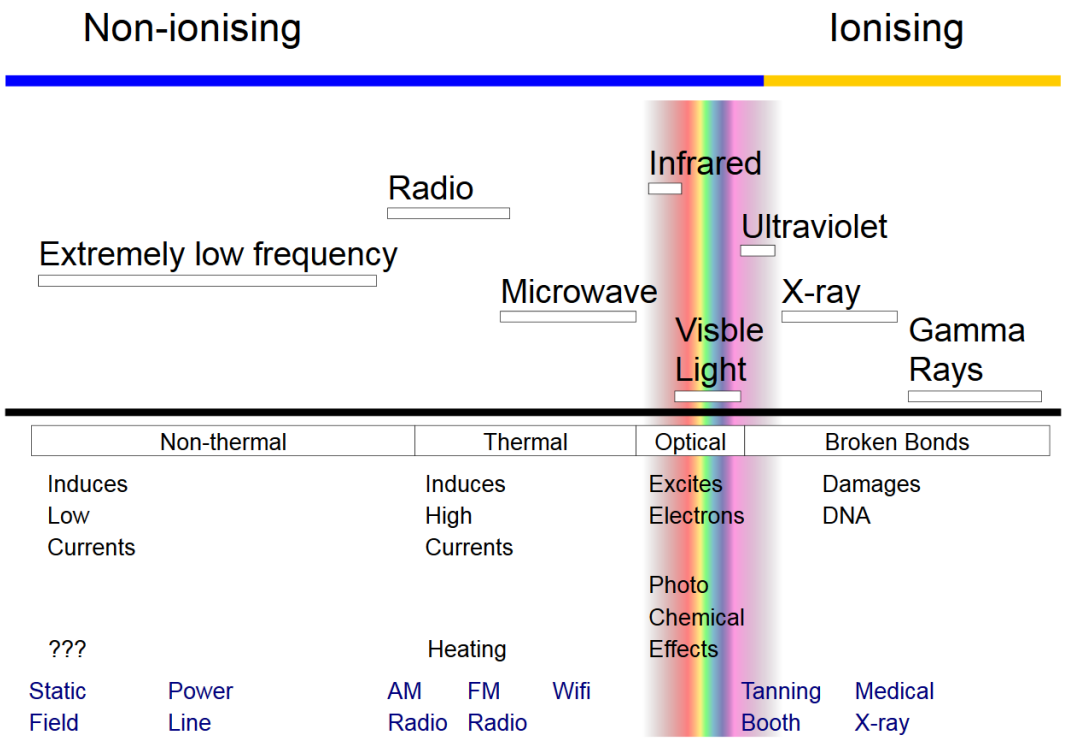

Figure 1. The electromagnetic spectrum. Figure by Wikimedia Commons user Spazturtle, license CC BY-SA 2.0.

The Universe is full of radiation, and the Sun is responsible for the most radiation hitting the Earth. The solar radiation consists of a range from the far infrared to X-rays, yet 99.9 % of all the radiation falls between 200−8000 nm, i.e. from the UV part to the far infrared [9]. Fortunately for the living species, the occasional high-energy gamma ray bursts that occur through the solar flare processes attenuate in the stratosphere [10]. For the animal kingdom and humans, some of the electromagnetic radiation is vital, some fatal and some have been harnessed for technological achievements.

2.1.1. UV radiation

Some amounts of the ionizing solar UV radiation are able to pass through the Earth's magnetic field, and this can be harmful for living creatures. According to Fitzpatrick, there are six human skin types, and with von Luschan's system all these are divided into 36 types (Figure 2). The most delicate types are the ones that have the least amount of melanin pigment (Greek *melas*, "dark, black") in them. [11]

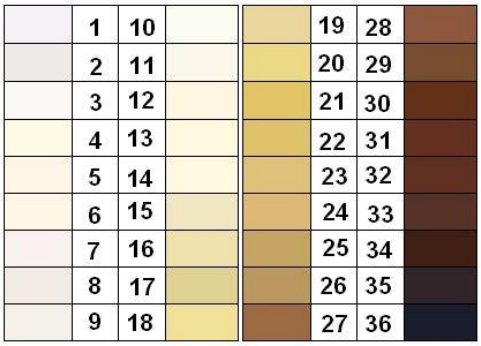

Figure 2. Von Luschan's skin type matrix. Figure by Wikimedia Commons user Matthias M., license CC BY-SA 2.0.

The pigment absorbs photons and is able to dissipate 99.9 % of the UV radiation as heat. This mechanism protects the cells from the damages done by the UV light, and as Meredith *et al*. have stated, the amount of melanin pigment is reciprocally proportional to the occurrence of skin cancers. [12]

According to WHO, there are 132,000 melanoma cases reported each year, and the number is growing constantly. One speculated reason is the ozone layer's depletion, but a significant factor is the increase of the recreational use of UV light, whether it be in solariums or during sunbathing. [13]

A risk assessment for skin cancer incidence can be made according to different skin types. Higher-risk types include e.g. fair skin, blue or green eyes, light hair color, burn tendency of the skin, the number of moles and freckles and cancer occurrence in the family. The biggest risk is for people with the fairest skin color, i.e. Fitzpatrick system types I–III. [13]

Since the effect of UV radiation to people's health has given rise to concern over sunlight-induced cancers, cost-efficient and reusable solutions to monitor hyperlocal UV levels are currently being and have been investigated. [7]

2.1.2. X-rays

Compared to UV, X-ray radiation is a higher-energy species which has a more uncommon natural occurrence on Earth than UV. Because X-rays are more energetic and humans or other species have not developed melanin pigment-like shielding mechanism for this type of radiation, X-rays are potentially more harmful for living organisms than UV radiation. While the protection mechanisms in the cells can repair damaged structures to some extent, in a case of high doses the mechanisms cannot keep up with the damages caused by the overwhelming ionizing radiation, resulting in radiation sickness or even necrosis or fatality. [14]

In a laboratory setup, X-rays are generally produced with an X-ray tube where electrons are accelerated in an electric field in vacuum. The electrons detach from the hot cathode and when they enter the electric field of an atomic orbital in the anode's material, the kinetic energy loss results in the release of energy as X-ray photons (Figure 3), either as a continuous *bremsstrahlung* (braking radiation) or in the case of exceeding the binding energy of an electron, characteristic radiation which occurs as peaks in an X-ray energy spectrum. [15]

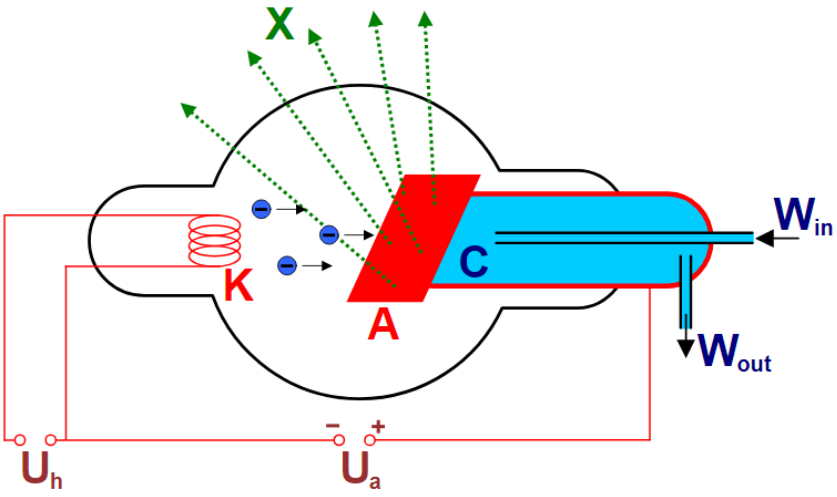

Figure 3. An X-ray tube where X = X-rays, K = cathode, A = anode, W_{in} = water cooling in, W_{out} = water cooling out, C = water cooler, U_h = cathode heater voltage, U_a = anode voltage. Figure by Wikimedia Commons user HMilch, public domain license.

Another way to produce X-rays is a synchrotron where the radiation is generated by bending the electron's path in a high-velocity storage ring. While an X-ray tube produces the

photons by tangential acceleration (or deceleration), synchrotron produces the radiation by centripetal acceleration. The available energy range in a synchrotron varies from IR to hard X-rays, and the spectral distribution is continuous and smooth. [16]

As with every type of radiation, the X-ray photons attenuate when they encounter obstacles in their path; attenuation varies depending on different radiation type and the material. In ionizing radiation's case the molar attenuation coefficient lowers as a function of energy, i.e. the more energy a photon has, the higher the probability to penetrate deeper into the material − or in a case of a very thin sample − the higher the probability for the photon to go through the material. [17]

X-rays can interact with matter through the following effects:

a) Photoelectric absorption or photoelectric effect, where the incident photon is absorbed completely into an electron in an atom, creating enough kinetic energy for the photon to exceed the threshold energy to bind it into an atom, i.e. escaping the atom. Another electron from an outer electron shell subsequently fills the hole left by the escaped electron, creating characteristic X-rays which depend on the ejected and the filler electron's shell. [17, 18]
b) Compton scattering which occurs when an incident photon hits an electron in the material, loses energy upon the collision and scatters deflected as a photon with lower energy and longer wavelength [18, 19].
c) Rayleigh scattering, Thomson scattering, coherent scattering, unmodified scattering, elastic scattering or classical scattering, where the X-ray photon travels through the material with deflections in its path, but without losing its energy [18, 20].
d) Pair production, which occurs when the photon energy is higher than 1.02 MeV. In this phenomenon an X-ray photon is annihilated completely and a resulting pair – an electron and a positron – is formed [18].
e) Photodisintegration, which occurs only at very high energy levels. The X-ray photon hits the nucleus and is absorbed completely, ejecting a particle from the nucleus [18].

2.1.3. Alpha radiation

Alpha decay creates particles equivalent to helium atoms with two electrons missing, denoted as $^{4}_{2}\mathrm{He}$ or $^{4}_{2}\mathrm{He}^{2+}$ or with the symbol α and is considered as a heavy particle source. Certain

heavy elements have unstable nuclei, which upon decay emit an alpha particle typically possessing an energy level of 4−10 MeV [21]. There is a heavy correlation between the alpha particle's energy and the half-life of the parent nucleus [22]. Figure 4 depicts a general alpha decay process.

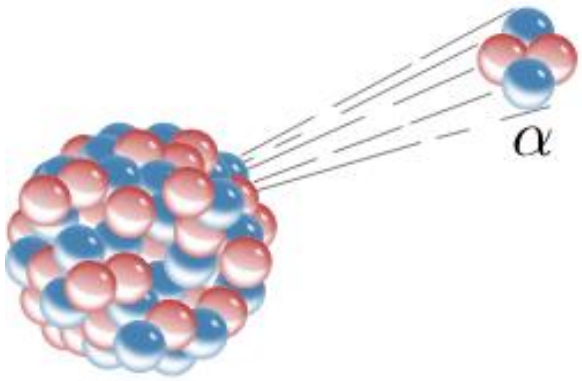

Figure 4. An illustration of alpha decay; red = protons and blue = neutrons. Figure by Wikimedia Commons user Inductiveload, public domain license.

An alpha decay example from daily life is the ^{241}Am nuclide found in fire alarms where the americium decays according to the following equation:

$$^{241}_{95}\mathrm{Am} \rightarrow {}^{237}_{93}\mathrm{Np} + {}^{4}_{2}\mathrm{He} + 5.63\ \mathrm{MeV} \qquad \text{(Eq. 1)}$$

The alpha radiation ionizes oxygen and nitrogen in the air, and the detector senses a small current which is applied through the ionized gas. When smoke enters the chamber, the detector detects a drop in electrical current, triggering an alarm switch or a programmatical loop break in the device. [23, 24]

The amount of energy in Equation 1 is calculated with Einstein's popular equation

$$E = mc^2 \qquad \text{(Eq. 2)}$$

where E = energy, m = mass and c = the speed of light in vacuum ($3.00 \cdot 10^8$ m·s^{-1}). The energy equivalence for mass can be transformed to

$$Q = \left(M_{241_{Am}} - M_{237_{Np}} - M_{\alpha}\right) c^2 \qquad \text{(Eq. 3)}$$

where Q = disintegration energy released in joules, M_x = masses of the atoms and particles in kg. The energy calculations are solved more conveniently by using the atomic mass unit, u. Plugging the numbers into the Equation 3 gives

$$Q = (241.056822u - 237.048166u - 4.00260325u)(931.494\ MeV \cdot u^{-1})$$
$$= (0.0060527u)(931.494\ MeV \cdot u^{-1})$$
$$= 5.63\ MeV.$$

The liberated energy is distributed between the daughter nucleus (^{237}Np) and the alpha particle. Since the ^{237}Np's mass is enormous compared to the alpha particle, most of the energy released is translated to the alpha particle's kinetic energy. [23]

The alpha particle has two protons making it doubly positively charged. When atoms get into the particle's trajectory, it ionizes them with either colliding with the electrons or ejecting them by coulombic attraction. This creates ion pairs, and one alpha particle can render thousands of atoms positively charged. One ion pair formation decreases the alpha particle's kinetic energy 35 eV on average, although it is also possible that the alpha particle fails to impose this amount of energy to eject an electron from the colliding atom, keeping the electron in the atom but rendering it into excited energy states. [23]

The alpha particle ejected from ^{241}Am can travel approximately 4 cm in air before losing its kinetic energy, acquiring two electrons by coulombic attraction and becoming helium gas. This short range of alpha particles limits the detection of this type of radiation, but in addition to an alpha particle, in the case of the nuclear decay reaction of ^{241}Am a gamma photon equivalent to 0.059 MeV is also emitted. Designing a dosimeter requires this to be taken into consideration, as a nuclide emitting a gamma photon will go through any obstacle and travel further and deeper than the alpha particles, i.e. the alpha radiation dose always includes some exposure to gamma. [23]

2.1.4. Beta particles and electrons

Similar to alpha, beta radiation is another example of particle radiation – the beta particle can eject electrons by colliding with them or coming into close proximity to it, but it is much smaller and lighter compared to the alpha particle: a beta particle has the same mass as an electron and the charge can be either negative (a *negatron*) or positive (a *positron*). Since a negatron has the same mass and charge as an electron, it is essentially a synonym for an electron. [23] Unstable nuclei are the cause for beta radiation, i.e. the proton-to-neutron ratio in the nucleus is too high or low [25]. Figure 5 shows an illustration of beta decay.

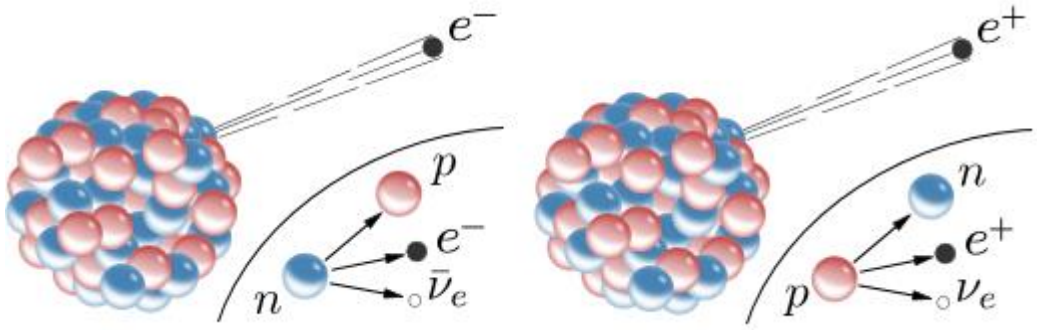

Figure 5. An illustration of beta decay; n = neutron (blue), p = proton (red), e^- = negatron or electron, e^+ = positron, $\bar{\nu}_e$ = antineutrino and ν_e = neutrino. Figure by Wikimedia Commons users Inductiveload and Master-m1000, public domain license.

Beta particles are formed by radioactive decay (Figure 5) or by pair production − a negatron and a positron are formed from gamma photons in the vicinity of a nucleus. During radioactive decay the formation of a beta particle can be expressed with Equations 4 (negatron) and 5 (positron). [23]

$$\mathrm{n} \rightarrow \mathrm{p}^+ + \beta^- + \bar{\nu}_e \qquad \text{(Eq. 4)}$$

$$\mathrm{p}^+ \rightarrow \mathrm{n} + \beta^+ + \nu_e \qquad \text{(Eq. 5)}$$

Beta particles do not ionize materials as much as alpha particles. Their speed can be close to the speed of light and are able to travel for tens of centimeters in air with pedesis, depending on the energy. An example of a beta-decaying isotope is technetium-99 which

decays to ruthenium-99 according to Equation 4. In some decay schemes, if the beta decay leaves extra energy to the nucleus, it is emitted as a gamma photon. [25]

For the case of electron bombardment, there exists a lot of methods to produce a beam. The most important ones are discharge sources, such as hot-filament-cathode effusive sources, effusive hollow-cathode discharge/sputter sources, gas-dynamic sources and supersonic DC discharge sources, or with charge-transfer sources, optical pumping sources or thermal sources [26]. The electron beam is controlled with magnets and the intensity can be measured with laser-induced fluorescence and quenching [27], chemical reactions [28], static electromagnetic field quenching [29] or Auger electron emission from solid surfaces [27].

2.1.5. Gamma rays

There is no consensus on the overlapping energy regions of X-rays and gamma radiation, but as a rule of thumb, theoretically gamma rays can be distinguished from X-rays by their origin – X-rays are generally produced from high-energy electrons, while gamma rays are a product of a nuclear reactions, although the properties are identical. In the electromagnetic spectrum, gamma rays have the highest energy (shortest wavelength, highest frequency). [30-32] Because of this, gamma radiation is able to cause damage to the intracellular molecules and is thus used as a sterilizing agent to kill microorganisms in e.g. consumables [33].

While gamma photons are high on energy, the penetrability of a gamma photon depends on its energy, and many materials become relatively gamma-transparent for the highest-energy photons. For imaging solutions, low energy 100−511 keV gamma rays are utilized because while they are able to penetrate the tissue, they are also easily measured with detectors. [32]

The cross section of interactions, otherwise known as the absorption coefficient, depends on the atomic number of the material. High Z results in higher statistical probability for the gamma photon to interact with the electron orbital, nucleus or the nuclear field. With orbital electrons the gamma photon is either absorbed, creating a photoelectric effect or scattered elastically or coherently, creating Rayleigh or Thomson scattering, or Compton scattering in the case of inelastic or incoherent scattering. In the nuclear field the absorption results in pair formation, and when the gamma photon hits the nucleus directly, the resulting phenomena

are nuclear reactions, resonance absorption or Mössbauer effect. If the photon is scattered from the nucleus, the effects are again nuclear reactions. [21]

2.2. Radiation dosimetry

Radiation interacts with matter by the photoelectric effect, positron-electron pair and triplet production, coherent or incoherent scattering or photonuclear processes, and these processes result in the emission of electrons that can ionize or excite atoms. In addition to generating heat, these effects can lead to the formation of new compounds which in turn can lead to problems in living tissue. [34] For these reasons, dosimetric applications have been developed to measure the intensity of the radiation for risk assessment, environmental monitoring and diagnostic radiology. [35]

For the dosimetric applications to have a practical purpose, the radiation intensity or dose must be measured accurately. If long-term exposure is monitored, another requirement for the dosimeter material is its ability to store the radiation's energy for long periods of time. If the trapped energy fades quickly, the dosimeter has no practical purpose. [35]

Commonly used dosimeters are electrical devices with live readout and warning alarms (a Geiger counter), but for measuring a longer period of exposure, radiochromic film dosimeters are an interesting alternative. Typically, the film dosimeters are comprised of organic molecules and the radiation-induced changes in the molecular structure are irreversible, i.e. the readout can be done only once, although a reversible organic dosimeter using polyvinyl alcohol and 10,12-pentacosadiynoic acid or a representative tetrazolium salt was recently successfully made by Kozicki *et al*. [36]

2.2.1. Electronic dosimeters

Commercially available ionizing radiation detectors include gas-filled tubes where the gas molecules are ionized, and the separate ions are attracted to the anode and cathode. This induces an electric current which can be measured. Another field includes the family of scintillation detectors where the ionizing radiation is converted to measurable photons. Other detector types are semiconductor detectors, track detectors (cloud chambers, autoradiography) and other types (solid-state detectors, chemical dosimeters). [21]

2.2.2. Thermoluminescence (TL) and optically stimulated luminescence (OSL)

In the experimental section of this thesis, the material's thermoluminescence and optically stimulated luminescence is studied. The theory of TL and OSL is based on the energy-band theory of solid materials where charge carriers – electrons or holes – get stuck in otherwise forbidden band gap regions called traps, which are occasional defects in the material. When the sample is irradiated with some types of radiation, it renders its charge carriers into a metastable state i.e. traps. This state is metastable for the fact that the charge carriers can be released and subsequently recombined with either a hole or an electron, depending on the charge carrier originally trapped and the stationary species residing in the original position. This process releases energy and produces visible, measurable luminescence. [37] An exemplified TL process is depicted in Figure 6.

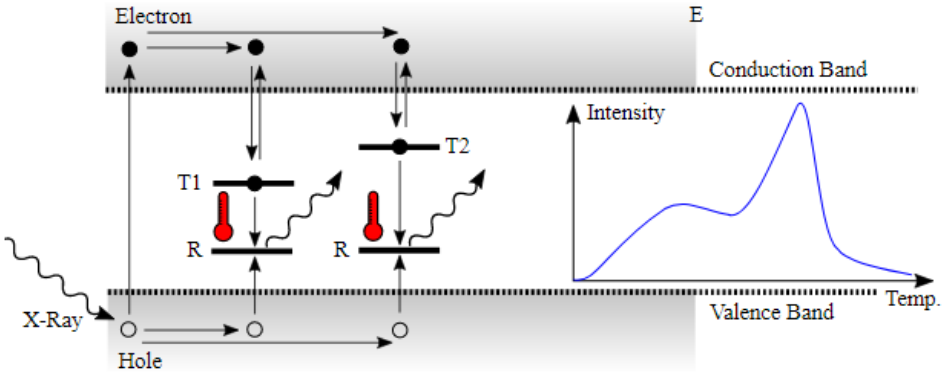

Figure 6. An illustration of thermoluminescence's principle. When an X-ray hits an atom in the valence band, it excites the electron into a trap (T1 = a deep trap or T2 = a shallow trap) via the conduction band. When the material is heated, the recombination occurs at the recombination center, R. Deeper traps are emptied with higher temperatures and shallower with lower. Figure by Wikimedia Commons users Michael Weinold, license Creative Commons Attribution-Share Alike 4.0 International.

The measurements are always relative to the sample and radiation type, meaning that e.g. in dating the measurement must be calibrated with the sample which has been irradiated with relevant radiation. In an ideal case, the TL measurements produce a linear dependency for the radiation dose, but sometimes they do not; e.g. a long exposure to gamma rays may

deteriorate the substance, meaning that there will be less sites for the charge carriers to get trapped, thus eventually producing less thermoluminescence. [37]

In TL measurements it is important to note that the charge carriers can get out of the traps spontaneously in time, especially in the case of shallow traps. When the sample is in ambient temperature, thermal movement is bound to occur, resulting in charge carriers' escape and thus lower TL signal. In addition to this, another phenomenon to consider is anomalous fading, where the TL signal fades more rapidly than what can be predicted by examining the trapping parameters. This is possibly related to quantum tunneling. [38]

Thermoluminescence has been widely studied for dosimetry applications at least from the 1950s. According to Kortov, the requirements for a perfect material would be high TL sensitivity per unit of absorbed dose, a wide linear response, low signal fading over time, a simple TL curve, low signal dependency on the radiation energy, luminescence spectrum matching photomultiplier tube response and appropriate physical properties. Some materials possessing these characteristics are currently LiF:Mg,Ti, LiF:Mg,Cu,P, ^{6}LiF:Mg,Ti, ^{6}LiF:Mg,Cu,P, CaF_2:Dy, CaF_2:Mn and Al_2O_3:C. [39]

2.3. Photochromism and cathodochromism

Photochromism is a material's property where the color changes with photon radiation. In organic media the phenomenon is based on the alteration of chemical bonds: exposure to UV light induces excitons which can break and induce chemical bonds or alter the relative arrangement of the molecules. This mechanism has been used in different types of photoresponsive materials, such as photodetectors, photoreceptors, photoswitches, phototranistors, solar cells and data storage. [40, 41] However, the mechanism usually allows the transition to happen only once and going back to the original state requires great amounts of energy. Usually the organic photochromism is based on extended π-electron systems which are not stable at high temperatures. One example is spiro-naphthoxazines or naphthopyrans which are normally positioned perpendicular against another molecule, but upon UV exposure they occupy the same plane. [42, 43]

In inorganic materials the photochromism can be reversible and the underlying principle in e.g. hackmanites is based on the formation of F centers (German *Farbzentrum*, "color center") where an electron gets trapped into an atom vacancy in the crystal lattice and absorbs

certain wavelengths specific to the F center in question, rendering the material colored. The electron can be relaxed to its original ground state with either heat or light, and contrary to organic ones, the inorganic materials are stable at a broad range of temperatures. Some well-known photochromic materials are WO_3 [44], MoO_3 [45] and doped TiO_2 [46], and hackmanite.

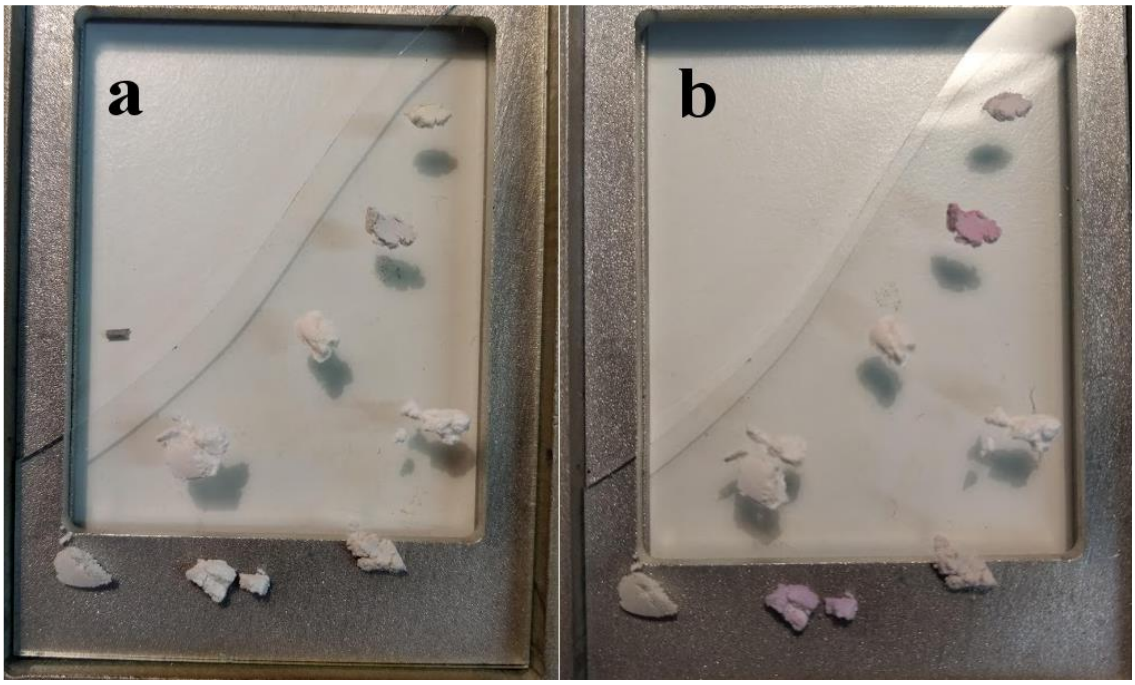

Figure 7. Various hackmanite samples a) before exposure b) after exposure to an electron beam in a cathodoluminescence setup.

X-ray induced photochromism is a rarely studied subject, although Jin *et al.* were successful at creating a $[Zn(OOCH)_2(4,4'\text{-bipyridine})]_n$ metal-organic framework which changes its color from white to blue upon exposure to X-rays [47]. However, the molecule is once again an organic derivative with uneconomical reversibility, unlike with inorganic materials.

Cathodochromism is the photochromism's corresponding alternative where the material changes its color upon exposure to high-energy electrons. It has been observed in $CaTiO_3$ powder, which can be bleached by light and is thus reversible. [48] Also alpha particle-induced coloration has been successfully tested on $SrTiO_3$ doped with Fe [49]. Figure 7 shows the cathodochromic effect in hackmanites.

The photochromic variety of sodalite ($Na_8Al_6Si_6O_{24}Cl_2$), the sulfur-containing hackmanite ($Na_8Al_6Si_6O_{24}Cl_{2-2x},S_x\square_x$ where x is typically ~0.1) and its variations exhibit reversible photochromism or tenebrescence [1, 2]. When the material is exposed to UV light for a short period of time, it changes its color to pink or purple [42]. The material can then be bleached with white light and the cycle repeated indefinitely [50]. The mechanism is based on color-centre formation in chloride vacancies in the structure. When the material is exposed to UV light, an electron from sulfur excites and trapped to a chloride vacancy in the lattice (Figure 8). [5, 51]

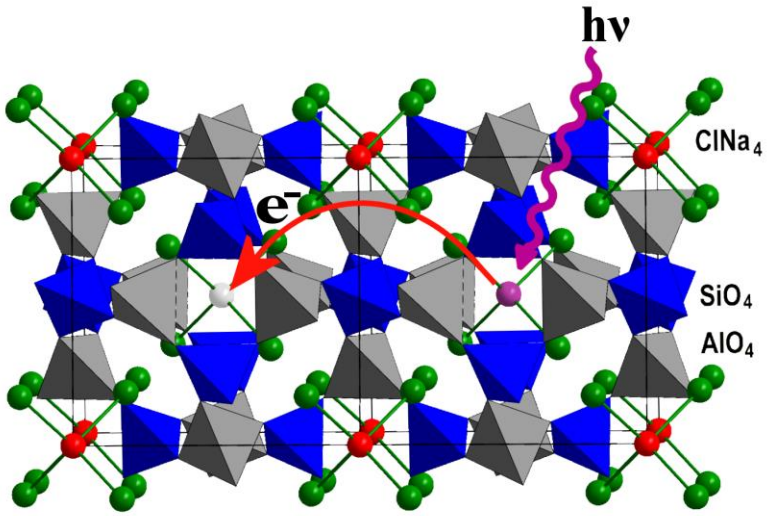

Figure 8. The sodalite cage in hackmanite ($Na_8Al_6Si_6O_{24}(Cl,S)_2$). Purple = sulfur, white = chloride vacancy. The incident photon (denoted as hν) interacts with sulfur's electron and excites it to the chloride vacancy, forming an F center.

Hackmanite's crystal structure is cubic, and the space group is $P\bar{4}3n$ [52], with each side of the cube measuring 8.877 Å [42]. As can be seen from Figure 8, the crystal lattice consists of $ClNa_4$, SiO_4 and AlO_4 cages. The chloride vacancy forms a lattice defect when sulfur is present because the charges are not balanced if a chloride ion enters the vacancy [53].

In addition to the typical hackmanite, species that have the sulfur replaced with selenium and tellurium have been reported. The Se-doped species exhibits a permanent red coloration, while the Te-doped one has a greenish-blue coloration upon exposure to UV. These materials can be made synthetically by substituting $NaSO_4$ with $NaSeO_4$ or $NaTeO_4$ during the preparation process. [54]

As reported by Norrbo *et al.*, the tenebrescence in hackmanites could be used to measure the UV index and the tenebrescence activation tailored to fit different measuring setups by substituting Na with other alkali metals, such as K and Rb. [7]

2.4. Colors spaces and color representation

Color spaces are mathematical representations to define the absolute values for a material's color. The human eye has a photopic vision that has peaks in the yellow, green and blue regions and the sense of color varies individually. Different approaches have been made to represent the absolute color coordinates of an object. [55]

Chromaticity coordinates are used to establish a chromaticity diagram which includes all the colors that a human can perceive. The outer ribbon goes from 380 to 700 nm, connected by a purple line (Figure 9). The horseshoe-shaped diagram holds the color spaces commonly encountered in paper industry, photomanipulation software and electronics, i.e. ProPhoto RGB, Adobe RGB, sRGB and 2200 matte paper. [55]

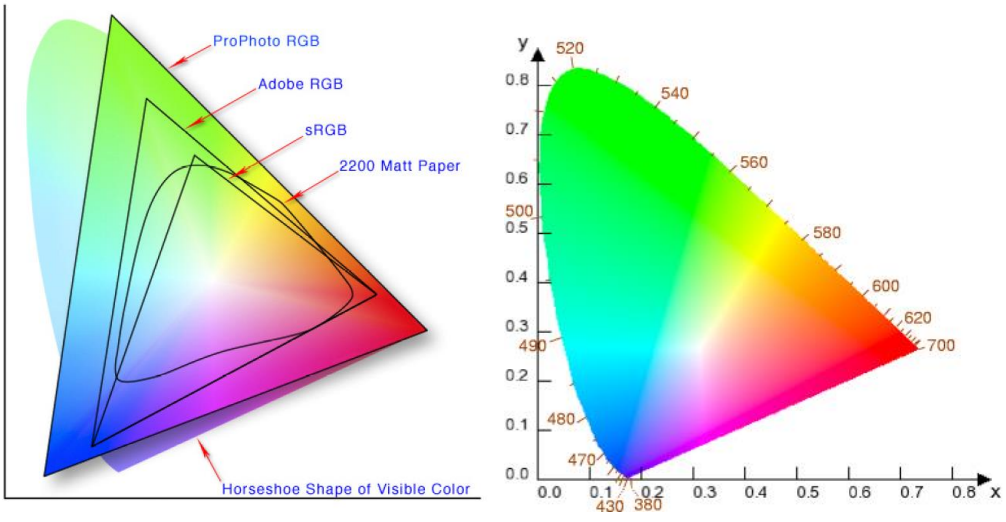

Figure 9. C.I.E. 1931 chromaticity diagrams. Figures by Wikimedia Commons users Cpesacreta and Shizhao, Creative Commons Attribution 2.5 Generic and public domain license, respectively.

In specifying and labeling the color coordinates and attributing them to a chromaticity diagram, different systems have been used. One example is the proprietary Munsell system

(Figure 10) where hue, chroma and grey scale value are presented with a combination of letters and numbers. [55]

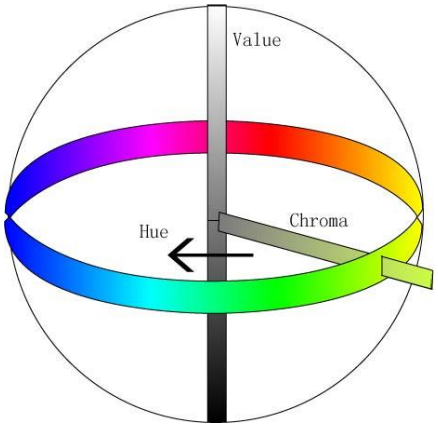

Figure 10. The Munsell color system. Value = grey scale or lightness. Figure by Wikimedia Commons user tsiaojian_lee, public domain license.

The three-dimensional CIE L*a*b* system is an industry standard used in color meters. The object is brightly illuminated with a short flash of light and analyzed with filters. The resulting color coordinates are presented with the parameters L* (lightness), a* (red−green) and b* (blue−yellow). The combined parameters form a system where the origin is the neutral black point (Figure 11). [55]

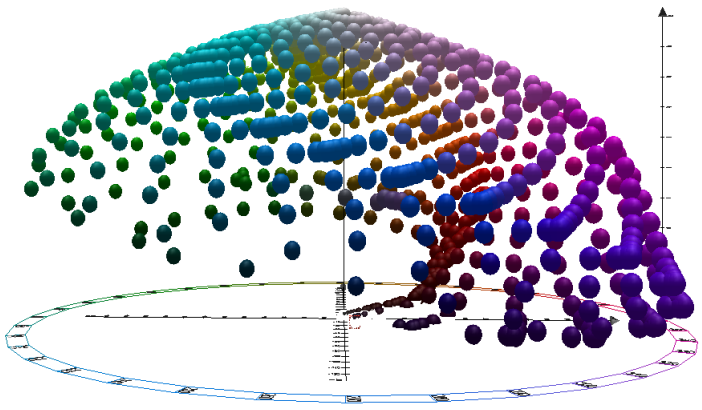

Figure 11. The CIE L*a*b* color system. The neutral black point is the origin. Figure by Wikimedia Commons user Holger Everding, Creative Commons Attribution-Share Alike 4.0 International license.

The RGB color system is used to describe the color values for televisions and other light-generating display equipment. These devices use the red, green and blue (hence RGB) channels to produce the colors for the pixels. Since the color gamuts shown in Figure 9 cannot be filled by a triangle, the RGB system can describe only a part of the color realm. [55]

The CMYK system is similar to the RGB system but is used in the printing industry. The principle is to use cyan, magenta and yellow inks with varying sizes of dots to produce the color. Black color is also added to adjust the lightness. [55]

2.5. X-ray analysis techniques

X-ray analysis techniques are used widely to gain information about solid materials especially when crystal lattices are present. This chapter focuses on the techniques used in the experimental section of this thesis.

2.5.1. X-ray diffraction (XRD)

XRD is a non-destructive qualitative tool used in metallurgy, mineralogy, materials science, biology, biochemistry etc. [56] and can be used to determine e.g. lattice constants, purity, crystallite size, thin film thickness [57, 58]

The XRD setup can consist of a synchrotron source or an X-ray tube where the beam goes either through the sample (transmittance mode) or is reflected from the sample (reflectance mode). The diffracted X-rays are typically detected by a scintillation counter or an imaging plate detector. [57]

The basic principle in an XRD setup is the crystal lattice's interaction with the incident photons in a way that the crystals diffract the X-ray photons to form either constructive or destructive interference. In Figure 12 the S_1 is an incident photon with a wavelength λ being diffracted from an atom. The S_2 is another incident photon with the same wavelength, also being diffracted from an atom residing d away from the other one on another plane in the lattice. If the two photons are in the same phase after the diffraction, they form constructive interference. In other words, if the total path difference is $2d \sin\theta$, constructive interference occurs when $n\lambda = 2d \sin\theta$.

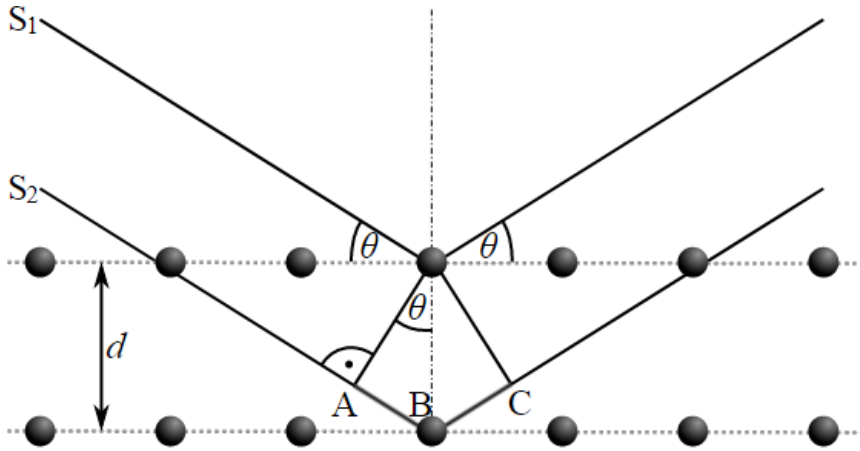

Figure 12. Diffraction's principle. S_1 = incident photon, S_2 = another incident photon. Figure by Wikimedia Commons user Freundchen, Creative Commons CC0 1.0 Universal Public Domain Dedication license.

The diffracted photons forming constructive interference generate a signal-inducing phenomenon (electron excitement, trapping or other) in the reader. The whole diffractogram can be then recorded by moving the detector or using a static detector which comprises of the whole possible diffraction angle range.

2.5.2. X-ray photoelectron spectroscopy (XPS)

XPS is a surface chemistry method used to study the electron binding energies in the material. The solid's photoelectrons residing in the surface of the material are excited, and the detaching electrons' energies are recorded, generating intensity peaks. The binding energies are element-specific and can be used to assess the oxidation state of the element in question or determine the surface's composition. [59]

Because the emitted electrons' energies are to be recorded, the XPS measurements need to be done in vacuum conditions so that the emitted electrons will not collide with air molecules. The photoelectrons residing more than 20−50 Å below the material's surface will not have sufficient energy to reach the detector. [59]

2.5.3. X-ray fluorescence (XRF)

X-ray fluorescence is a non-destructive emission technique to study the composition of the sample. When a material is exposed to X-rays, the elements in the material emit characteristic

X-rays when the electrons are excited. XRF can typically be used to determine all elements except low-Z elements such as Li, H and He. [57]

In XRF the incident X-ray hits the element's electron which is either excited to a higher orbital or completely emitted from the atom. When emission occurs, the hole left by an electron is filled by another electron in a higher orbital. This process emits an energetic X-ray photon which is recorded by the XRF machine's detector. These photon energies are characteristic to each element, thus allowing the assignment of each emission energy to a specific element. [57] The resulting spectrum comprises of peaks at different energies which can be deconvoluted and integrated, allowing the analysis of elemental composition in the sample.

2.5.4. X-ray absorption near edge structure (XANES)

XANES is yet another non-destructive method utilizing synchrotron radiation for characterizing e.g. an element's coordination environment and oxidation state. X-rays can remove inner shell electrons and these electrons have very specific and exact binding energies. If a material exposed to X-rays and the X-ray energy is scanned, the energies where inner electrons are ejected cause sudden rises in the absorption spectrum. These rises are called absorption edges. (Figure 13). Different elements have different binding energies for the orbital electrons, with the K shell having the most tightly bound electrons, the L shell the second most tightly etc. [60-62]

The edge energies are relative to the chemical characteristics of the atoms being probed with X-rays. As the electrostatic model describes, the absorbing element's edge energy increases with oxidation state, i.e. the higher the oxidation state, the higher the energy needed to unbind the electrons. [62, 63] Another feature of the XANES spectrum is the pre-edge peak which results from $1s \rightarrow 3d$ transitions. Thus it is chracteristic for all metals with vacancy in the $3d$ orbital. The pre-edge process shows as a weak peak before the K edge, because the transition is forbidden by the quantum mechanical selection rules. [64] A sulfur's XANES spectrum is shown in Figure 13.

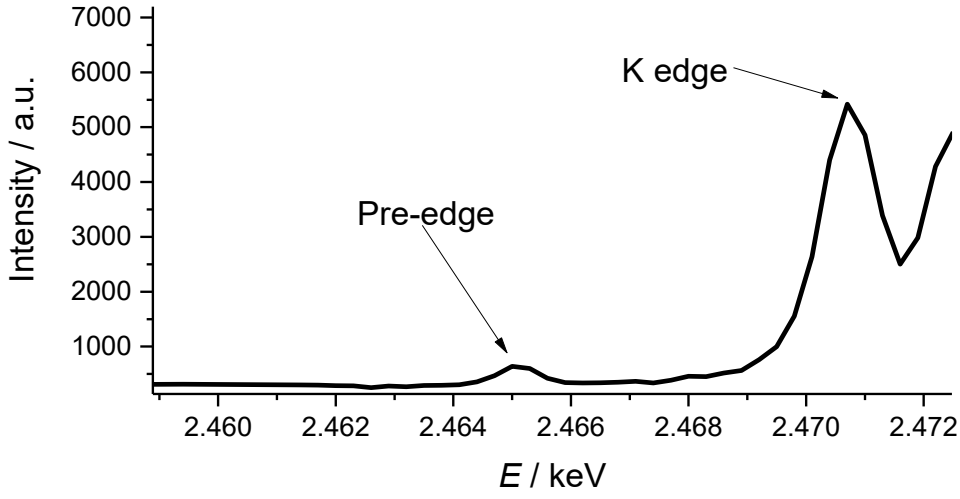

Figure 13. A sulfur's XANES spectrum showing sulfur's pre-edge and K edge.

3. Experimental

The experimental section in this thesis contains all the laboratory work and data plots conducted on all the samples. The section describes the syntheses of the samples, casting them as tapes and the effects caused by different type of radiation in hackmanite.

Materials and methods are integrated in the subsections for consistency. All the relevant data are presented in the sections so that they form packages that can be read not only as a part of the story, but also individually.

3.1. Reagents and substances

The reagents and substances used in this work is given in Table 1. All the substances were measured and weighed with an unused plastic spoon or a capillary pipette with a Mettler AE-100 analytical balance.

Table 1. The reagents and substances used in this work.

Substance	Manufacturer	CAS no	Grade	Lot no
Al_2O_3	Aldrich	1344-28-1		11574-066
LiCl	Acros	7447-41-8	99 %	A010058801
NaCl	J. T. Baker	7647-14-5	> 99.5 %	0425110025
KCl	Merck	7447-40-7	≥ 99.5 %	K48659536 738
RbCl	Sigma	7791-11-9	≥ 99.0 %	

Na_2SeO_4	Sigma	10102-23-5		SLBV3659
NaBr	J.T. Baker	7647-15-6		5110
Na_2SO_3	Merck	7757-82-6	> 99 %	341 TD364449
S	BHD Chemicals Ltd.	7704-34-9		1126720
TiO_2	Merck	13463-67-7		
Zeolite A ($NaAlSiO_4$)	Sigma-Aldrich	1318-02-1		BCBF5787V
FORMIER® 10 (N_2/H_2 mixture (90/10 %))	AGA			
2-butanone	Sigma	78-93-3	> 99.0 %	
Ethanol	Altia	64-17-5	Aa (> 99.5 %)	
Polyvinyl butyral (PVB)	Sigma	63148-65-2		
Benzyl butyl phthalate (BBP)	Aldrich	85-68-7	98 %	308501
Triton X-100	Sigma-Aldrich	9002-93-1		
Disponil FES 993	BASF	68891-38-3		

3.2. Sample preparation

The sample preparation procedure follows the same principle for all the samples, but the reaction-specific parameters differ. The procedure is as follows.

1. The zeolite is dried in a furnace (Nabertherm N3/C8) at 500 °C for 1 h and let to cool in a desiccator.
2. Reagents are weighed on a white paper with an unused plastic spoon for minimal metal contamination.
3. The reagents are ground and stirred in an agate mortar for 10 minutes.
4. The sample is heated in air at a temperature specified in Table 2.
    a. The mixture is transferred to an alumina crucible as an even layer.
    b. The crucible is put into a furnace (Elite TSH12/50/300-2416CG), which is programmed with specific parameters (Table 2).
    c. After the heating the sample is ground in an agate mortar and transferred to the alumina crucible again.
5. The sample is heated in a reducing gas.
    a. The alumina crucible is placed in a quartz reactor, both shown in Figure 14.

Figure 14. Alumina crucible (orange) in a quartz reactor (inlet and outlet not sealed).

b. The reducing gas (N_2/H_2) inlet and outlet tubes are attached to both ends of the quartz reactor. The tubes go from the gas bottle to the reactor via a rotameter (MFG By Fischer & Porter Co 0078-1).
c. The pressure regulator valve (HARRIS 801 30 LPM) is opened from the gas bottle so that the rotameter's ball floats between the numbers 5 and 6. The gas is let to flow for 10 minutes into the reactor and the system is checked for leaks.
d. The furnace (Lindberg Blue/M) is programmed with sample-specific parameters (Table 2).
e. When the cycle is over, the sample is ground in an agate mortar and put into a sample container.

Table 2, Table 3 and Table 4 enlist all the reagents and masses needed in the synthesis of all the samples used in this work. The general synthesis procedure is given in section 3.2. After the synthesis, all the samples are washed to remove the interfering excess NaCl according to the following procedure:

1. The sample is put into an Eppendorf™ tube.
2. 1 ml of quartz-distilled water is added, and the tube is shaken well.
3. The phases are separated with a centrifuge (10 min at 5000 g, Heraeus Biofuge Stratos).
4. The water phase is removed with a pipette.
5. The sample is dried in a desiccator.

Table 2. Reagents and sintering and reduction parameters for $(Li,Na)_8Al_6Si_6O_{24}(Cl,S)_2$ (sample ID LiNaHack), $Na_8Al_6Si_6O_{24}(Cl,S)_2$ (sample ID NaHack20), $Na_8Al_6Si_6O_{24}(Cl,S)_2$ (sample ID NaHack19) and $Na_8Al_6Si_6O_{24}(Cl,Se)_2$ (sample ID SeHack14).

Substance	**$(Li,Na)_8Al_6Si_6O_{24}(Cl,S)_2$**	**$Na_8Al_6Si_6O_{24}(Cl,S)_2$**	**$Na_8Al_6Si_6O_{24}(Cl,S)_2$**	**$Na_8Al_6Si_6O_{24}(Cl,Se)_2$**
Sample no/ID	LiNaHack	NaHack20	NaHack19	SeHack14
Date	11.9.2018	7.10.2018	6.10.2018	1.10.2018
Reagents				
Zeolite, *m* / g	0.700	0.700	0.700	0.700
NaCl, *m* / g	0.12	0.24	0.24	0.70
Na_2SO_4, *m* / g	0.060	0.060	0.060	
Na_2SeO_4, *m* / g				0.24
LiCl, *m* / g	0.12			
Sintering in air				
Step	20→850 °C	20→850 °C	20→850 °C	20→750 °C
Rate, °C/min	3.0	3.0	3.0	3.0
Dwelling time, h	48.0	48.0	48.0	48.0
Cooling	Passive	Passive	Passive	Passive
Furnace	Elite TSH12/50/300-2416CG	Elite TSH12/50/300-2416CG	Elite TSH12/50/300-2416CG	Lindberg Blue/M
Reduction in N_2/H_2				
Step	20→850 °C	20→850 °C		20→750 °C
Rate, °C/min	18.0	18.0		18.0
Dwelling time, h	2.0	2.0		2.0
Cooling	Passive	Passive		Passive
Furnace	Lindberg Blue/M	Lindberg Blue/M		Lindberg Blue/M

Table 3. Reagents and sintering and reduction parameters for $Na_8Al_6Si_6O_{24}(Cl,Se)_2$ (sample ID 5), $Na_8Al_6Si_6O_{24}(Br,S)_2$ (sample ID 6).

Substance	**$Na_8Al_6Si_6O_{24}(Cl,Se)_2$**	**$Na_8Al_6Si_6O_{24}(Br,S)_2$**
Sample ID	5	6
Date	1.10.2018	23.12.2018
Reagents		
Zeolite, *m* / g	0.700	0.700
NaCl, *m* / g	0.70	
Na_2SO_4, *m* / g		0.120
Na_2SeO_4, *m* / g	0.24	
NaBr, *m* / g		0.3734
Sintering in air		
Step	20→750 °C	20→850 °C
Rate, °C/min	3.0	3.0

Dwelling time, h	48.0	48.0
Cooling	Passive	Passive
Furnace	Lindberg Blue/M	Elite TSH12/50/300-2416CG
Reduction in N_2/H_2		
Step	20→750 °C	20→850 °C
Rate, °C/min	18.0	18.0
Dwelling time, h	2.0	2.0
Cooling	Passive	Passive
Furnace	Lindberg Blue/M	Lindberg Blue/M

Table 4. Reagents and sintering and reduction parameters for $(Rb,Na)_8Al_6Si_6O_{24}(Cl,S)_2$ (sample ID RbHack16), $(Rb,Na)_8Al_6Si_6O_{24}(Cl,S)_2$ (sample ID 10), $(K,Na)_8Al_6Si_6O_{24}(Cl,S)_2$ (sample ID 11) and $(K,Na)_8Al_6Si_6O_{24}(Cl,S)_2$ (sample ID 12).

Substance	**$(Rb,Na)_8Al_6Si_6O_{24}(Cl,S)_2$**	**$(Rb,Na)_8Al_6Si_6O_{24}(Cl,S)_2$**	**$(K,Na)_8Al_6Si_6O_{24}(Cl,S)_2$**	**$(K,Na)_8Al_6Si_6O_{24}(Cl,S)_2$**
Sample ID	RbHack16	10	11	12
Date	2.10.2018	2.10.2018	18.9.2018	18.9.2018
Reagents				
Zeolite, *m* / g	0.700	0.700	0.700	0.700
Na_2SO_4, *m* / g	0.060	0.060	0.060	0.060
S, *m* / g		0.0263		0.0263
RbCl, *m* / g	0.4958	0.4958		
KCl, *m* / g			0.3057	0.3057
Sintering in air				
Step	20→850 °C	20→850 °C	20→850 °C	20→850 °C
Rate, °C/min	3.0	3.0	3.0	3.0
Dwelling time, h	48.0	48.0	48.0	48.0
Cooling	Passive	Passive	Passive	Passive
Furnace	Elite TSH12/50/300-2416CG	Elite TSH12/50/300-2416CG	Elite TSH12/50/300-2416CG	Elite TSH12/50/300-2416CG
Reduction in N_2/H_2				
Step	20→850 °C	20→850 °C	20→850 °C	20→850 °C
Rate, °C/min	18.0	18.0	18.0	18.0
Dwelling time, h	2.0	2.0	2.0	2.0
Cooling	Passive	Passive	Passive	Passive
Furnace	Lindberg Blue/M	Lindberg Blue/M	Lindberg Blue/M	Lindberg Blue/M

3.3. Tape casting and reusability of the tape

Tape casting, also known as knife coating or doctor blading, is a process where a thin sheet of ceramic or metal particle suspension fluid is cast on a substrate. In a usual setting the fluid contains volatile non-aqueous solvents, a dispersant, binders and the dry matter.

Commercially cast tapes are usually 0.025−1.27 mm in dry thickness, but some manufacturers report to be able to cast tapes as thin as two microns used in the manufacture of electrical capacitors. The cast tape can be removed from the substrate, if necessary. [65]

The process involves making the suspension and superimposing it onto a surface: generally, a stepper motor-driven moving "blade" casts the slurry on a substrate, but in this work an *ad hoc* tool (Figure 15) was made and used for proof of concept purposes. The casting groove's depth is machined to 200 µm.

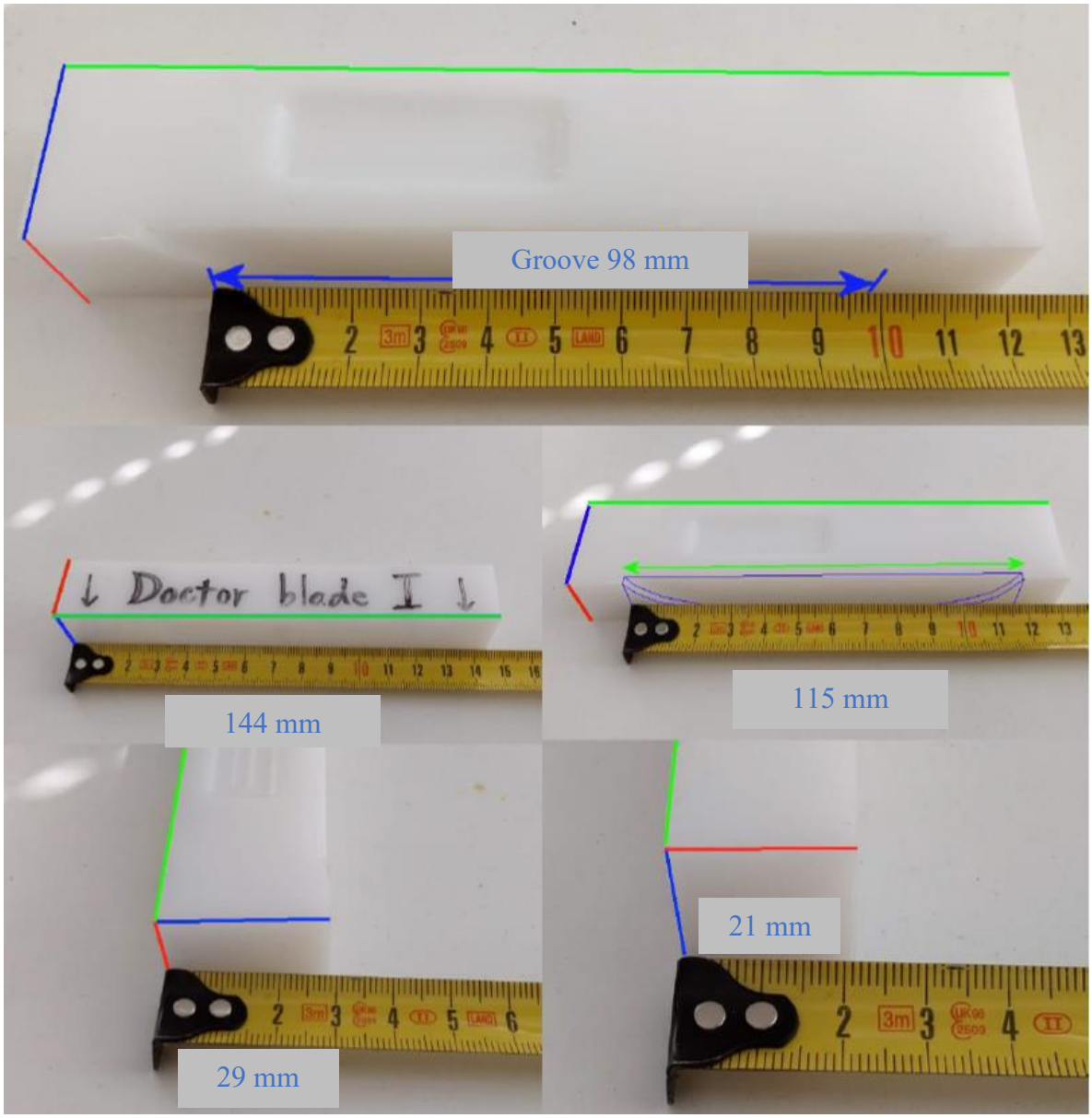

Figure 15. The doctor blade device used in this work.

The first step was to create a suitable suspension recipe so that the slurry would be able to spread onto the substrate easily, but also so that the suspension's viscosity and thus the amount of solvents wouldn't be too high because the dried layer was intended to contain as much dry matter as possible. The dry matter in this case is hackmanite in powdered form.

Various recipes from different scientific literature sources were inspected. Variations are given in Table 5 through Table 7.

Table 5. The suspension recipe used by Kumari *et al.* [66].

Constituent	**Role of constituent**	**Wt %**
ZrO_2	Ceramic powder	57.72
Phosphate ester	Dispersant	0.52
Xylene	Solvent	16.66
EtOH	Solvent	4.45
Cyclohexanone	Homogenizer	0.35
PEG 600	Plasticizer	2.50
BBP	Plasticizer	2.50
PVB	Binder	15.30

Table 6. The suspension recipe used by Abhinay *et al.* [67].

Constituent	**Role of constituent**	**Wt %**
BZT-0.5BCT	Ceramic	65−48
Phosphate ester (Emphos PS21-A)	Dispersant	1.0
Methyl ethyl ketone (E. Merck India Ltd.) + Ethanol (Bengal Chemicals & Pharmaceuticals Ltd. India)	Solvent	25−36
Polyvinyl Butyral (Hipol B-30, Hindustan Inks and Resins Ltd.)	Binder	2.75−7
Polyethylene Glycol (S.D. Fine-Chem Pvt. Ltd.)	Plasticizer	3.74−5.1
Butyl Benzyl Phthalate (Merck-Schuchardt)	Plasticizer	1.5
Cyclohexanone (S.D. Fine-Chem Pvt. Ltd.)	Homogenizer	1.25

Table 7. The suspension recipe developed by Descamps *et al.* [68].

Constituent	Amount
Dry matter	68 %
Binder	2−7 %
Plasticizer	300 % of the binder's concentration
Dispersant	0.8 % of the dry matter's concentration
Solvent	the rest of the suspension, consisting of 72 % trichloroethylene and 28 % ethanol

The binder's role is to create a polymer network around the dry matter particles, while the plasticizer functions as a softening agent for the binder. When combining these two substances the tape becomes resistant against cracking and flaking off when bent. The dispersant is used to deaggregate the particles and homogenize the suspension. [69]

The suspension is made in two stages: first the dry matter, the solvent and the dispersant are mixed together. The addition of other substances follows second because if all the ingredients are mixed at once, the dispersant would lose some effect because of the competitive adsorption of the binder and the plasticizer. [69]

After gathering the boundaries where the weight percentages lie within the recipes, some derivative recipes (Table 8) were tested to see which performs best.

Table 8. Tested recipes for the tape casting process.

Recipe ID	Wt %, ceramic powder	Wt %, PVB	Wt %, BBP	Wt %, 2-butanone	Wt %, ethanol	Wt %, Triton X-100
1	63	5	2.5	21.6	8.4	0
2	50	5	2.5	34.2	13.3	0
3	40	5	2.5	41.4	16.1	0
4	30	5	2.5	48.6	18.9	0
5	20	5	2.5	55.8	21.7	0
6	10	5	2.5	63.0	24.5	0
7	5	5	2.5	66.6	25.9	0
8	41	7	7	32.4	12.6	0
9	40	7	6	30.0	15.0	2

The recipe 9 proved to be the most usable in terms of applicability with the doctor blade device. The suspension's treatment procedure needed to be examined next. The treatments were as follows, and the results are shown in Figure 17. All the tapes were cast onto a projector transparency with a piece of another transparency.

1. No dispersant, mixing with a laboratory spatula, casting onto a projector transparency (polyethylene terephthalate film) with a piece of another transparency.
2. Mixing the ceramic, the solvent and the dispersant with a planetary grinding mill (Philips Minimill PW4018/00) for 10 minutes at speed 1. Mixing BBP and PVB with a spatula.
3. The ceramic powder ground with a planetary grinding mill 10 minutes at speed 1, then mixing the ground powder with the solvent and the dispersant 10 minutes at speed 1 in a planetary grinding mill, and last, mixing BBP and PVB with the suspension 2 minutes at speed 1 in a planetary grinding mill.

   The mill's speed settings are given in Table 9 and the inner dimensions are shown in Figure 16.

Table 9. The mill's settings with corresponding rotation speeds.

	Speed 1	**Speed 5**	**Speed 10**
Motor speed, 1/min	400	1730	3400
Plate speed, 1/min	85	370	720
Ball speed, 1/min	170	740	1440

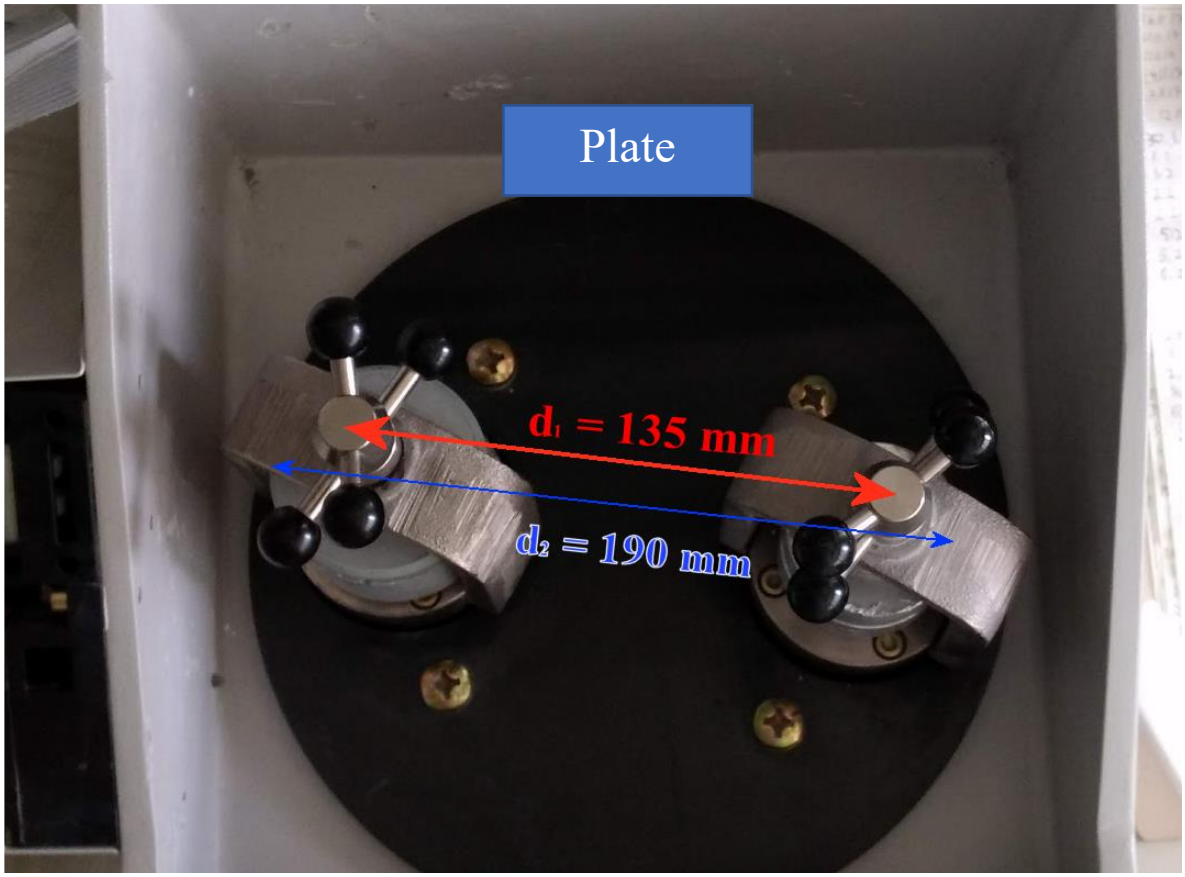

Figure 16. The insides of the planetary grinding mill.

As can be seen from Figure 17, the most homogeneous results were achieved with treatment 3, yet still there was room for optimization: after mixing BBP and PVB the planetary grinding mill's balls contained a blob of elastic white substance on top. After experimenting with only BBP and PVB it was noticed that these two reagents begin to react very fast, forming the aforementioned elastic matter. The recipe was optimized further by raising the final grinding speed to 5. After trying out the new treatment procedure, the white matter was no longer being formed during the grinding.

It was also noted that the casting must be done quickly because the suspension's volatile solvents start to evaporate immediately after opening the mill cup. The suspension is prone to creating a dry layer on top of the liquid very fast with the used solvents, leading to the casting process' failure.

Figure 17. The treatment results. All the tapes are cast onto a PET film with a another piece of the same film a) No dispersant; mixing in a test tube with a laboratory spatula b) Mixing the ceramic powder, the solvent and the dispersant in a planetary grinding mill (Philips Minimill PW4018/00) for 10 minutes at speed 1; mixing BBP and PVB with a spatula c) The ceramic powder ground with a planetary grinding mill for 10 minutes at speed 1; mixing the powder with the solvent and the dispersant for 10 minutes at speed 1 in a planetary grinding mill; mixing BBP and PVB with the suspension for 2 minutes at speed 1 in a planetary grinding mill.

The different recipes and casting procedures are presented in Table 10. In most cases the tape's surface topography was not optimal since it contained unevenness throughout the whole film, especially the films cast on glass.

Table 10. Tape casting tests. All the recipes contain 40 % of powder.

Cast	Powder	Substrate	Stirring	Casting device	Outcome
1	Al_2O_3	Glass, clear	Powder + solvent + Triton X-100 10 min @ speed 5 BBP and PVB 2 min @ speed 5	Doctor blade	Bumpy (Fig. 18 a)
2	Al_2O_3	Glass, dark	Powder + solvent + Triton X-100 10 min @ speed 5 BBP and PVB 2 min @ speed 5	Doctor blade	Bumpy and uneven (Fig. 18 b)
3	$(Li,Na)_8Al_6Si_6O_{24}(Cl,S)_2$:Ti (2 %)	PET plastic	Powder + solvent + Triton X-100 10 min @ speed 1 BBP and PVB 2 min @ speed 1	PET plastic sheet	Slightly uneven, bubbles (Fig. 18 c)
4	$(Li,Na)_8Al_6Si_6O_{24}(Cl,S)_2$:Ti (2 %)	PET plastic	Powder + solvent + Triton X-100 10 min @ speed 1 BBP and PVB 2 min @ speed 1	Doctor blade	Slightly uneven (Fig. 18 d)
5	$(Li,Na)_8Al_6Si_6O_{24}(Cl,S)_2$:Ti (2 %)	PET plastic	All substances in a test tube	Doctor blade	Coarseness; bad surface (Fig. 19 a)

6	Al_2O_3	PET plastic	Powder + solvent + Triton X-100 10 min @ speed 5 BBP and PVB 2 min @ speed 5	Doctor blade	Slightly uneven (Fig. 19 b)
7	Al_2O_3	PET plastic	Powder + solvent + Disponil® FES 993 10 min @ speed 5 BBP and PVB 2 min @ speed 5	Doctor blade	Bumpy and uneven (Fig. 19 b)

The different outcomes of the tape casting tests are shown in Figure 18 and Figure 19. As can be seen from the figures, the surface of the tapes cast on a sheet of glass proved to be uneven. In cast 7 (Figure 19 c) Triton X-100 was replaced with another dispersant, Disponil® FES 993, which also produced a bumpy surface.

The final recipe and procedure to produce the tape was

1. The sample powder is ground in a planetary grinding mill (Philips Minimill PW4018/00) for 10 minutes at speed 1.
2. The following substances are put into the mill and ground for 10 minutes at speed 1:
    a. ceramic powder 40 % (minimum 0.5 g)
    b. 2-butanone 30 %
    c. ethanol 15 %
    d. Triton X-100 2 %
3. The remaining ingredients are put into the mill and ground for 2 minutes at speed 5:
    a. PVB 7 %
    b. BBP 6 %
4. The suspension is taken out from the mill cup with an unused plastic spoon, dropped onto the substrate and cast with the least delay possible with the doctor blade device. The speed of the doctor blade device's movement is kept at ~5 cm s^{-1}.

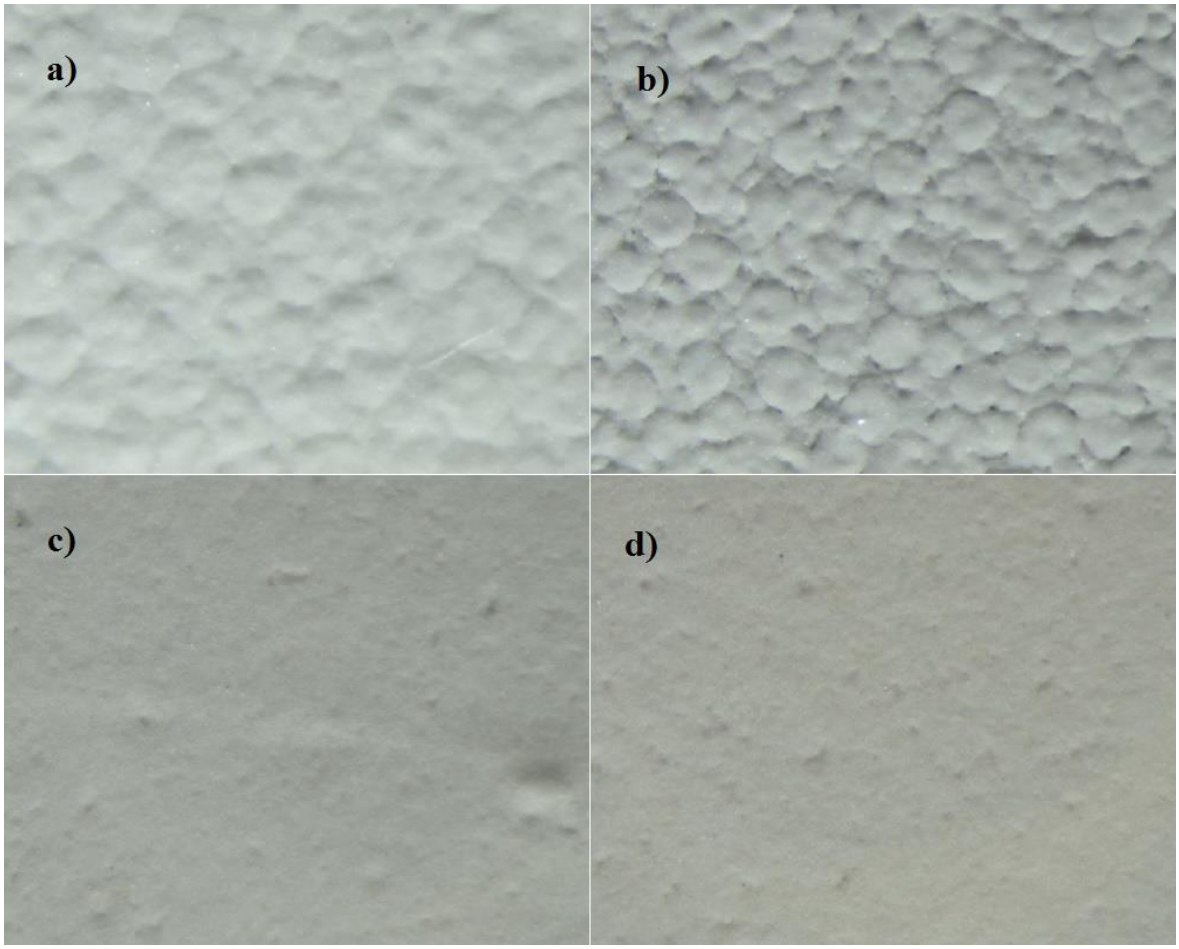

Figure 18. Images taken with a Nikon D5300 DSLR (FW C1.00 L 2.00) and Nikon SMZ800 light microscope. Table 10, a) cast 1 b) cast 2 c) cast 3 d) cast 4. Shutter speed 1/6 s, sensitivity ISO 100, color space sRGB, white balance incandescent, light source an incandescent lamp.

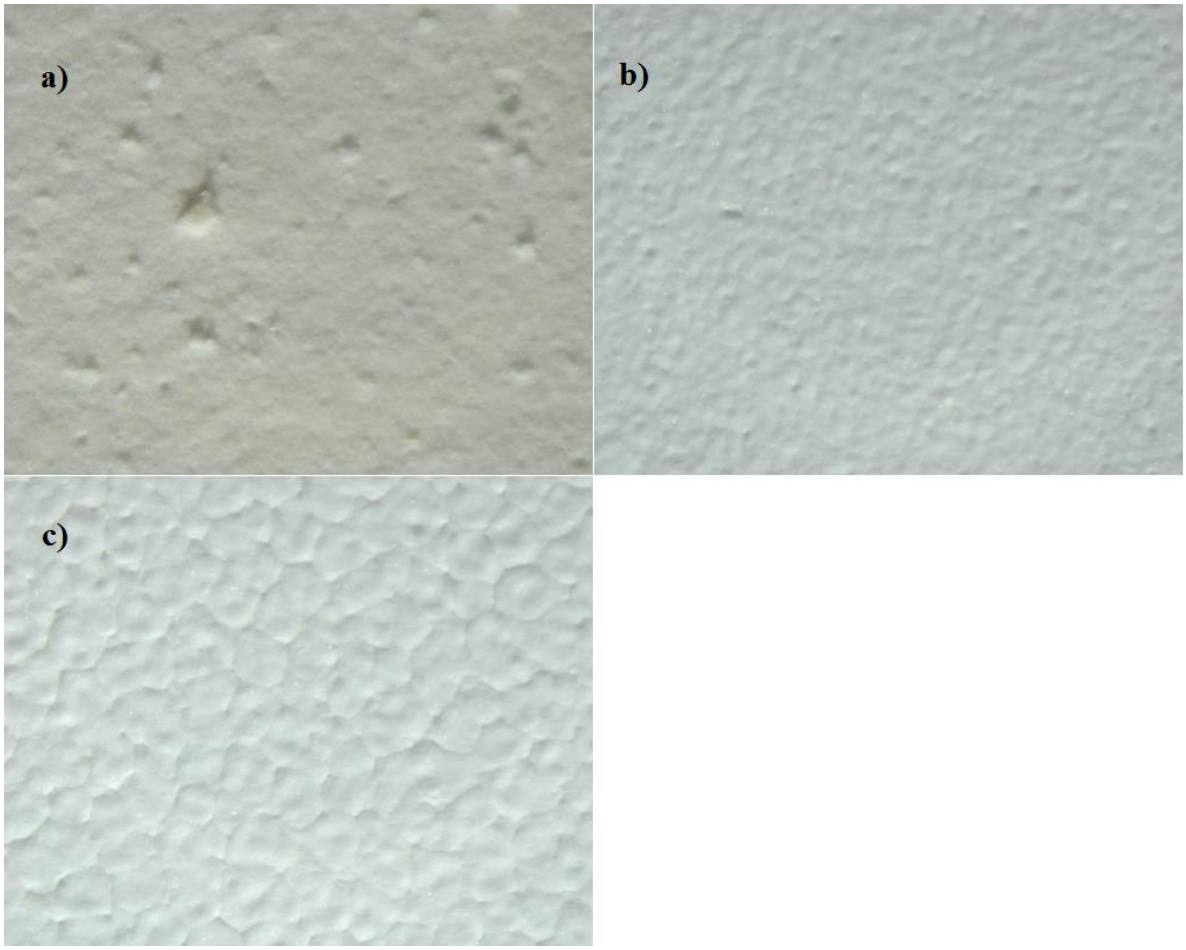

Figure 19. Images taken with a Nikon D5300 DSLR (FW C1.00 L 2.00) and a Nikon SMZ800 light microscope. Table 10, a) cast 5 b) cast 6 c) cast 7. Shutter speed 1/6 s, sensitivity ISO 100, color space sRGB, white balance incandescent, light source an incandescent lamp.

A tape with the powdered $(Li,Na)_8Al_6Si_6O_{24}(Cl,S)_2$:Ti (2 %) sample was cast on a PET film with the aforementioned treatment procedure, and the sample was sent to Åbo Akademi's SEM facility. The rendered images are shown in Figure 20, Figure 21 and Figure 22.

According to Figure 21 the tape's thickness is 77.11 µm (the PET film being 48.52 µm). Since the doctor blade device's casting groove is machined to 200 µm depth, the dried tape shrinks 61 % after drying.

Figure 20 to Figure 22 show that the bulbous-shaped dry matter particles are cast well into the plastic and no loose matter can be seen, thus it can be safely said that the binding effect is achieved with this treatment.

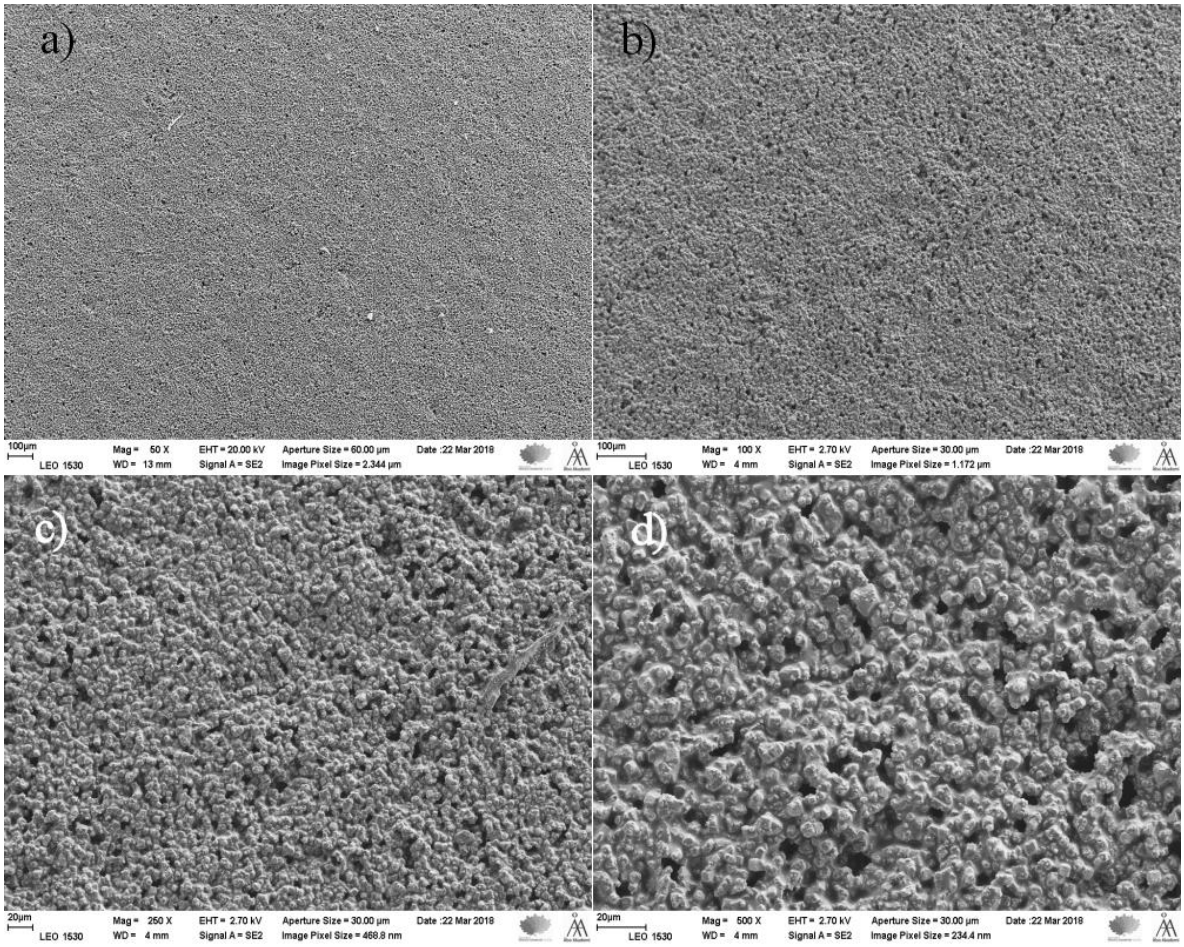

Figure 20. SEM images of the $(Li,Na)_8Al_6Si_6O_{24}(Cl,S)_2$:Ti (2 %) tape. a) 50x magnification b) 100x magnification c) 250x magnification d) 500x magnification.

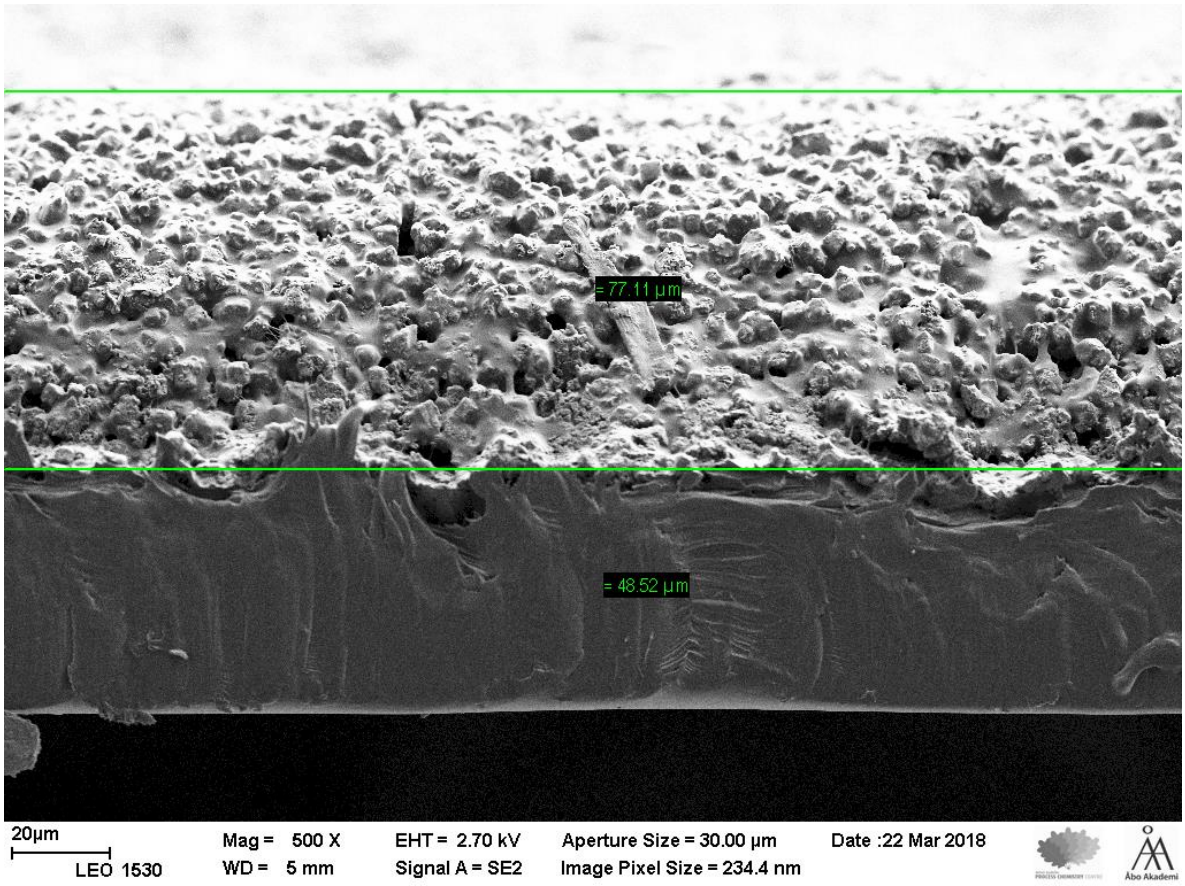

Figure 21. SEM image of the $(Li,Na)_8Al_6Si_6O_{24}(Cl,S)_2$:Ti (2 %) tape, dissected view, 500x magnification.

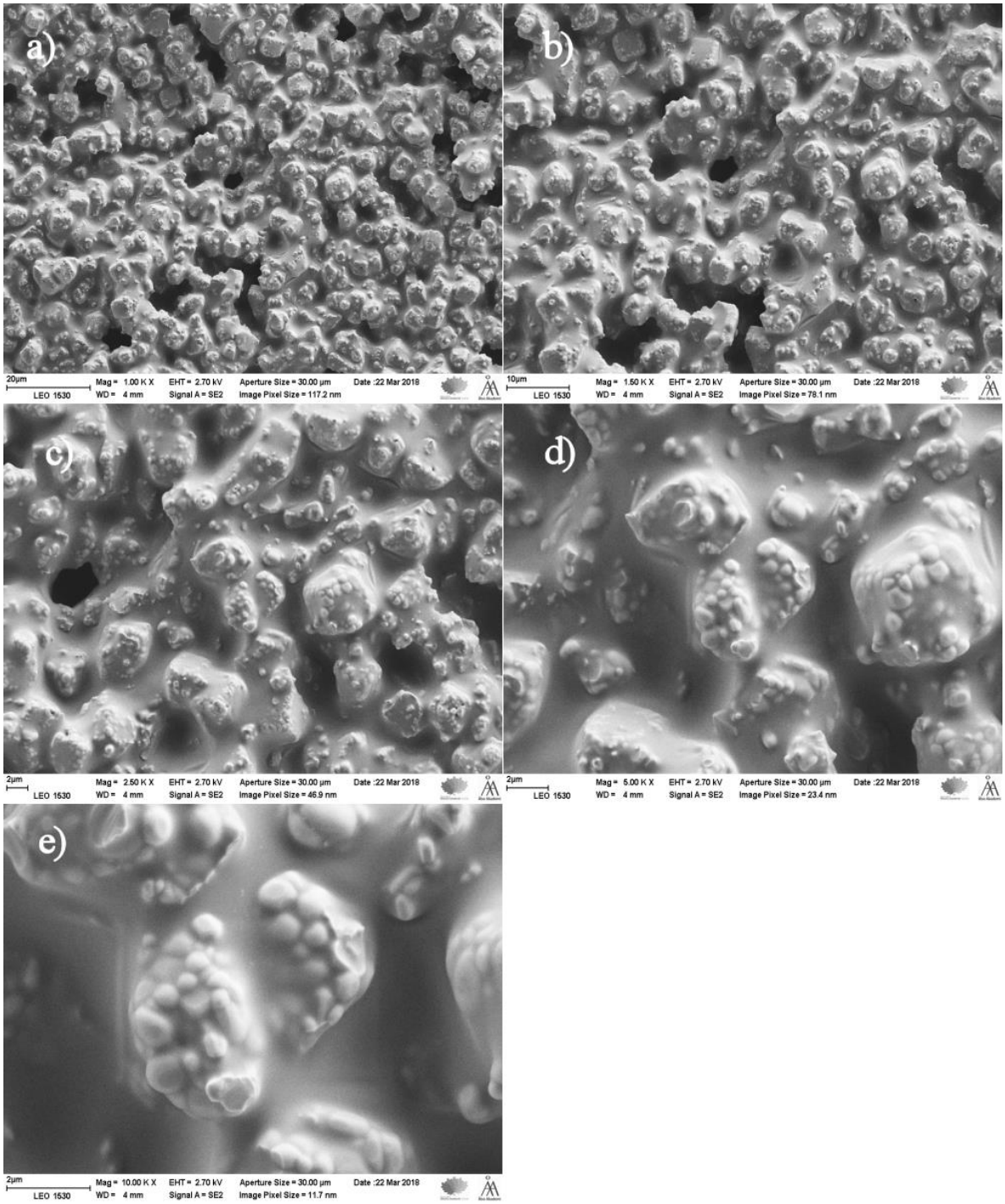

Figure 22. SEM images of the $(Li,Na)_8Al_6Si_6O_{24}(Cl,S)_2$:Ti (2 %) tape. a) 1 000x magnification b) 1 500x magnification c) 2 500x magnification d) 5 000x magnification e) 10 000x magnification.

During the SEM imaging, an energy-dispersive X-ray fluorescence (EDX) spectrum was gathered from the sample as well. The results are shown in Figure 23 and Table 11. In the EDX spectrum the carbon peak originates from the tape's binder and plasticizer which are organic substances.

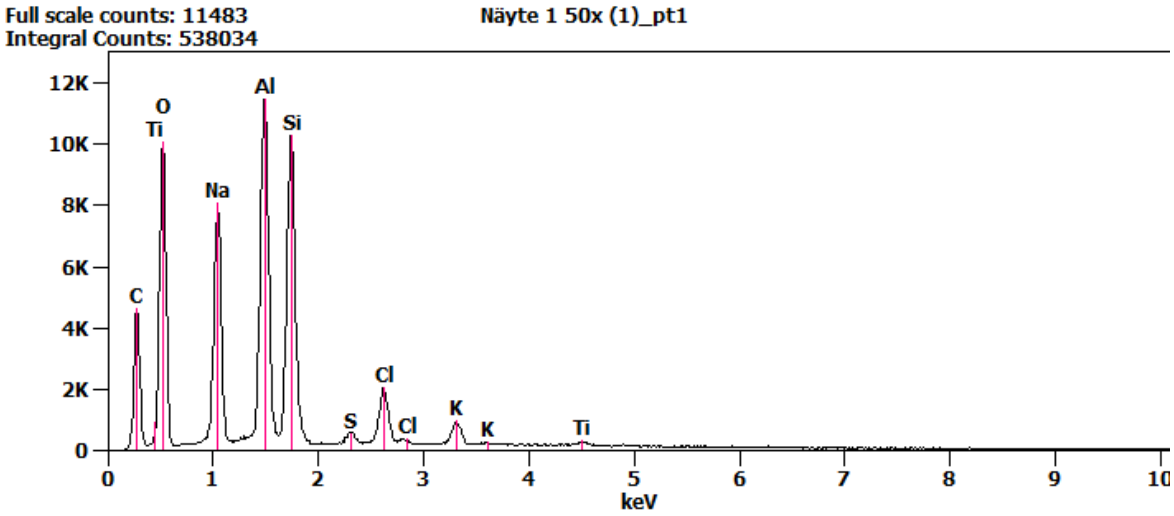

Figure 23. An EDX analysis made from the $(Li,Na)_8Al_6Si_6O_{24}(Cl,S)_2$:Ti (2 %) tape. Näyte 1 is the sample's name.

Table 11. EDX results from the $(Li,Na)_8Al_6Si_6O_{24}(Cl,S)_2$:Ti (2 %) tape.

	O-K	***Na-K***	***Al-K***	***Si-K***	***S-K***	***Cl-K***	***K-K***	***Ti-K***
Weight %	36.43	17.09	18.14	19.83	0.91	4.71	2.12	0.77
Weight % Error (+/- 1 Sigma)	±0.43	±0.10	±0.10	±0.11	±0.06	±0.07	±0.06	±0.07
Atom %	49.17	16.06	14.52	15.25	0.61	2.87	1.17	0.35
Atom % Error (+/- 1 Sigma)	±0.58	±0.09	±0.08	±0.09	±0.04	±0.04	±0.03	±0.03
Formula	O	Na	Al	Si	S	Cl	K	Ti
Compound %	36.43	17.09	18.14	19.83	0.91	4.71	2.12	0.77

The cast tape's reusability is of high importance for cost-effectiveness. Since handling the tape makes it subject to wear and tear, it is important to be able to regain the inorganic powder from the tape and cast it again. To study how the inorganic matter could be regenerated from the tape most efficiently without thermal treatment impacting too much on the sample's properties, a thermogravimetric analysis was carried out with the following

parameters on a Thermogravimeter TA Instruments Q600 using the Universal Analysis 2000 [70] program running on Windows 7:

- Sample $(Li,Na)_8Al_6Si_6O_{24}(Cl,S)_2$ tape, 10 mg
- Temperature 22→1400 °C with 10 °C/min heating
- Air atmosphere 100.00 ml/min

Figure 24 shows that the organic materials (PVB, Triton X-100 and BBP) are most probably evaporated after the 400 °C mark.

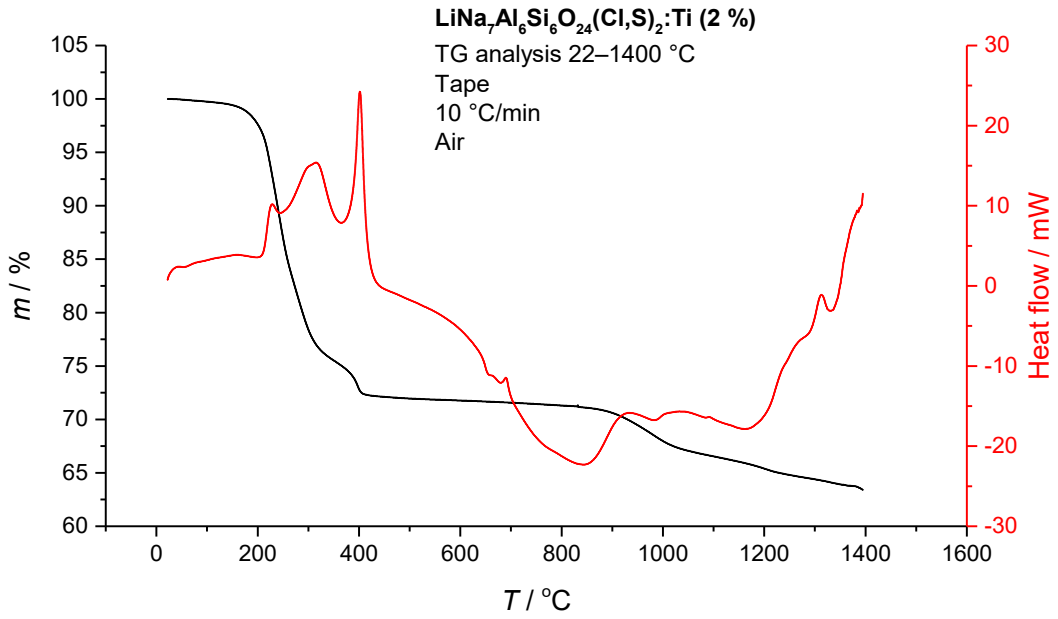

Figure 24. A TG analysis of a $(Li,Na)_8Al_6Si_6O_{24}(Cl,S)_2$ tape.

According to the information obtained from Figure 24, five samples were prepared to examine the depth of tenebrescence in different stages:

- Sample 1: The original synthetized $(Li,Na)_8Al_6Si_6O_{24}(Cl,S)_2$ powder.
- Sample 2: A tape made with sample 1.
- Sample 3: A regenerated powder – sample 2 put into a furnace (Nabertherm N3/C8) for 1 h at 500 °C and the resulting powder was ground in an agate mortar.
- Sample 4: sample 3 heated further for 3 h at 850 °C (Elite TSH12/50/300-2416CG)
- Sample 5: sample 4 reduced again for 2 h at 850 °C (N_2/H_2) (Lindberg Blue/M).

The samples' color-changing properties were studied with an Avantes AvaSpec-HS-TEC spectrometer with an Avantes FC-IR600-1-ME-HTX fiber, the light source being an Ocean Optics LS-1 Cal lamp. The software was AvaSoft [71] running on Windows 7 and the integration time was set to 242.2019 ms with 20 measurements' average per one spectrum. The sample was irradiated with a 5W UVP UVM-57 Handheld UV Lamp 302 nm for 1 min from 5.0 cm away from the sample. The measured spectra are shown in Figure 25. There are noticeable anomalous peaks at the bottoms of the spectra, which is caused by a defect in the detector.

From Figure 25 it can be seen that the tape made from the original powder proved to attain the deepest color, while the original powder got a deeper color than the powder regenerated from the tape at 500 °C for 1 h in air. This made an important discovery that, although the tenebrescence is slightly deteriorated during the process, the powder can be reused after the tape is no longer usable due to mishandling, cracking or other reasons.

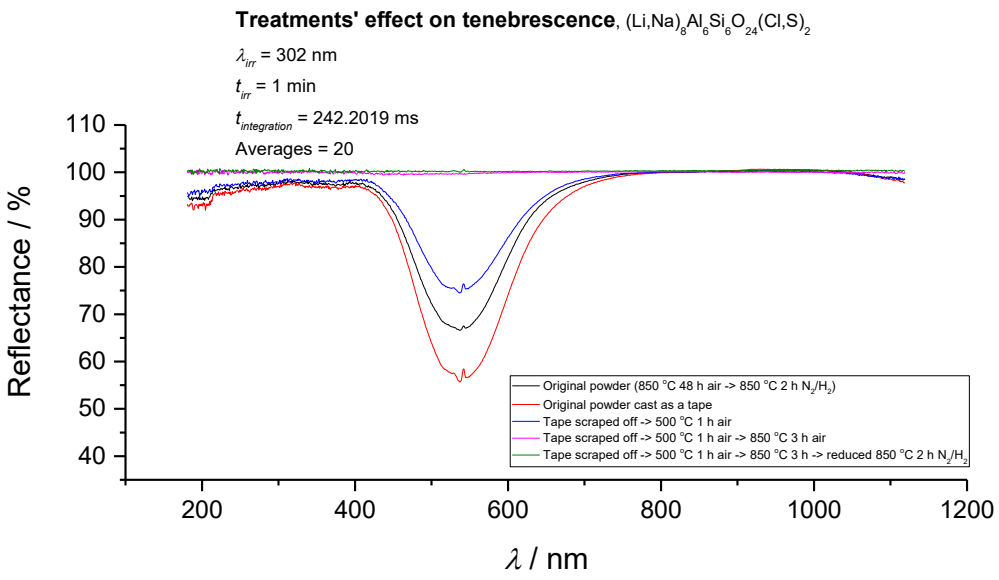

Figure 25. Reflectance spectra of UV-exposed $(Li,Na)_8Al_6Si_6O_{24}(Cl,S)_2$ samples with different treatments.

The results show that re-reducing the sample that has been heated to 850 °C in air is to no avail when trying to create the tenebrescence ability again. To study whether the crystal

structure changes in the transition from 500 °C to 850 °C, a series of XRD measurements were carried out with the following X-ray diffraction setup using the Huber Guinier G670 Data Acquisition Program [72] running on Windows 98 SE:

- Radiation shield Rigaku GeigerFlex
- X-ray source PANalytical FINE FOCUS Cu PW2223/20
  - K-α (1.54060 Å)
  - 1500 W
  - Operation at 40 kV, 30 mA
- Huber Guinier G670 camera with an BaFBr:Eu^{2+} imaging plate
  - Acquisition time 20 min
  - 10 imaging plate scans

The obtained diffractograms shown in Figure 26 demonstrate that the diffraction peaks are at the same places in all samples, but the sample undergone the 850 °C treatment has noticeably shorter peaks in the diffractogram than the two other ones, i.e. FWHM broadens, which can be due to smaller crystallite sizes, microstrain or structural defects caused by the heating procedure.

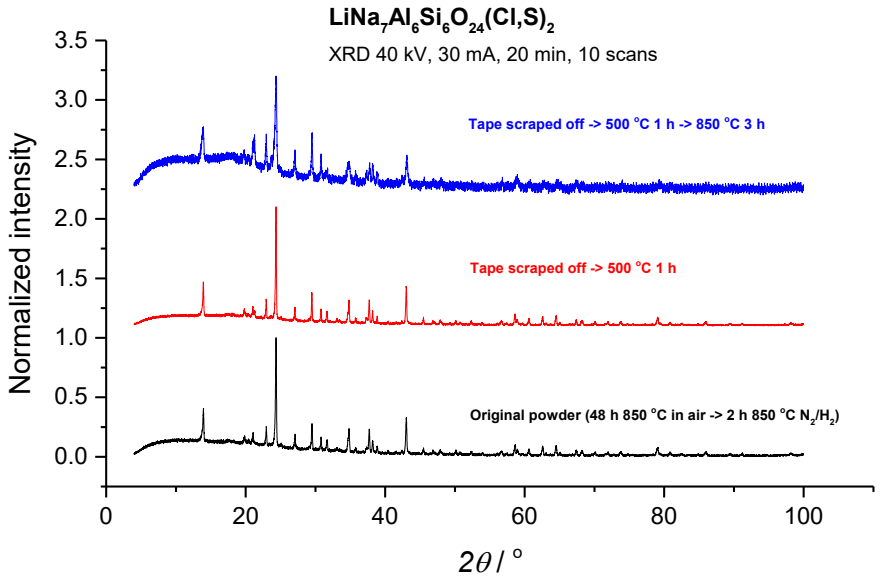

Figure 26. XRD diffractograms of the original powder (black), the regenerated powder (red) and the regenerated powder heated further (blue).

The color-changing ability is not present any more in the sample after being heated in air at 850 °C, not even if the powder is reduced again. Therefore, the powder should preferentially be regained at 500 °C to retain the ability to change its color. Even though the ability remains after the treatment at 500 °C, the color doesn't reach the depth of the original powder. Still, the organic matter can be safely evaporated from the hackmanite's surroundings, allowing the regeneration of the valuable material.

3.4. X-ray-induced effects in hackmanites

Karlsruhe Institute of Technology in Karlsruhe, Germany offered 5 days for measurements to be carried out at the synchrotron facility at ANKA hall's Synchrotron Umwelt-Labor SUL-X beamline. The accelerator is a 110-m 2.5-GeV electron storage ring and the photons are emitted by a wiggler source with the energy range of 2.3−20 keV. [73, 74]

The X-ray measurements were carried out to examine how the synthetized materials change their color under exposure to X-rays and whether there is distinct difference in coloring below and above the sulfur K-edge (2.4720 keV). An Avantes AvaSpec ULS2048CL-EVO spectrometer was used with an optical fiber Avantes FC-IR600-1-ME-HTX to measure the reflectance spectrum of the tape's exposed area. The light source was Ocean Optics LS-1 Cal and the typical sample setup is presented in Figure 27. The software was AvaSoft [71] running on Windows 7.

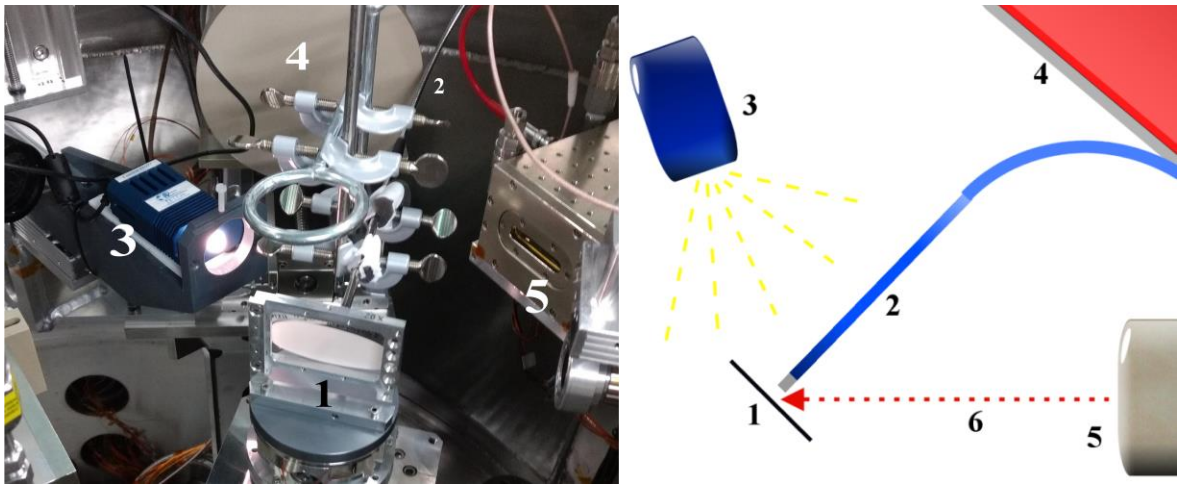

Figure 27. The measurement setup both *in situ* and as a corresponding schematic diagram. The sample tape in its holder (1), spectrometer fiber (2) 10 mm from the sample surface, the

light source (3) 20 cm from the sample surface, X-ray fluorescence detector (4), beamline (5), incident X-rays from the beamline (6).

The original sample exposure and measurement procedure is shown in Figure 28 and explained in detail below.

1. The sample is exposed to 20 keV X-rays for a qualitative color change observation. This can be done in non-vacuum conditions since attenuation of X-rays is minimal in air and should not change the outcome of the experiment.
   1.1. If the sample doesn't show any coloration, the sample is replaced with a next one since nothing can be done to achieve the coloration in this sample.
   1.2. If coloration can be detected under 20 keV exposure, the spectrometer fiber is fixed to this spot and the sample is moved to have the fiber point at a non-irradiated, fresh spot.
      1.2.1. A time series measuring the spectrum's integral is started and the beamline's shutter is opened to expose the spot to X-rays. When the graph is saturated to some extent, the time passed to reach this level is used in subsequent measurements (step 2).
      1.2.2. The time series measurement is carried out with another energy, decided on site.
2. The measurement chamber is vacuumized and the sample is irradiated in darkness with different energies for a time based on step 1.2.1.
3. The sample is taken out of the vacuum to be photographed.
   3.1. If all the irradiated spots are colored, the sample is replaced with a next one.
   3.2. If only some are colored, the following procedure is carried out.
      3.2.1. If all the non-colored spots are above 4 keV, a spectrometer is used in non-vacuum to measure the reflectance spectrum in a finer range near the energy levels where the coloration threshold is. The sample is photographed afterwards.
      3.2.2. If there are colored spots at or below 4 keV, a finer scan near the threshold of coloration is carried out in vacuum and the sample is photographed after the exposure. The spectrometer cannot be used in vacuum.

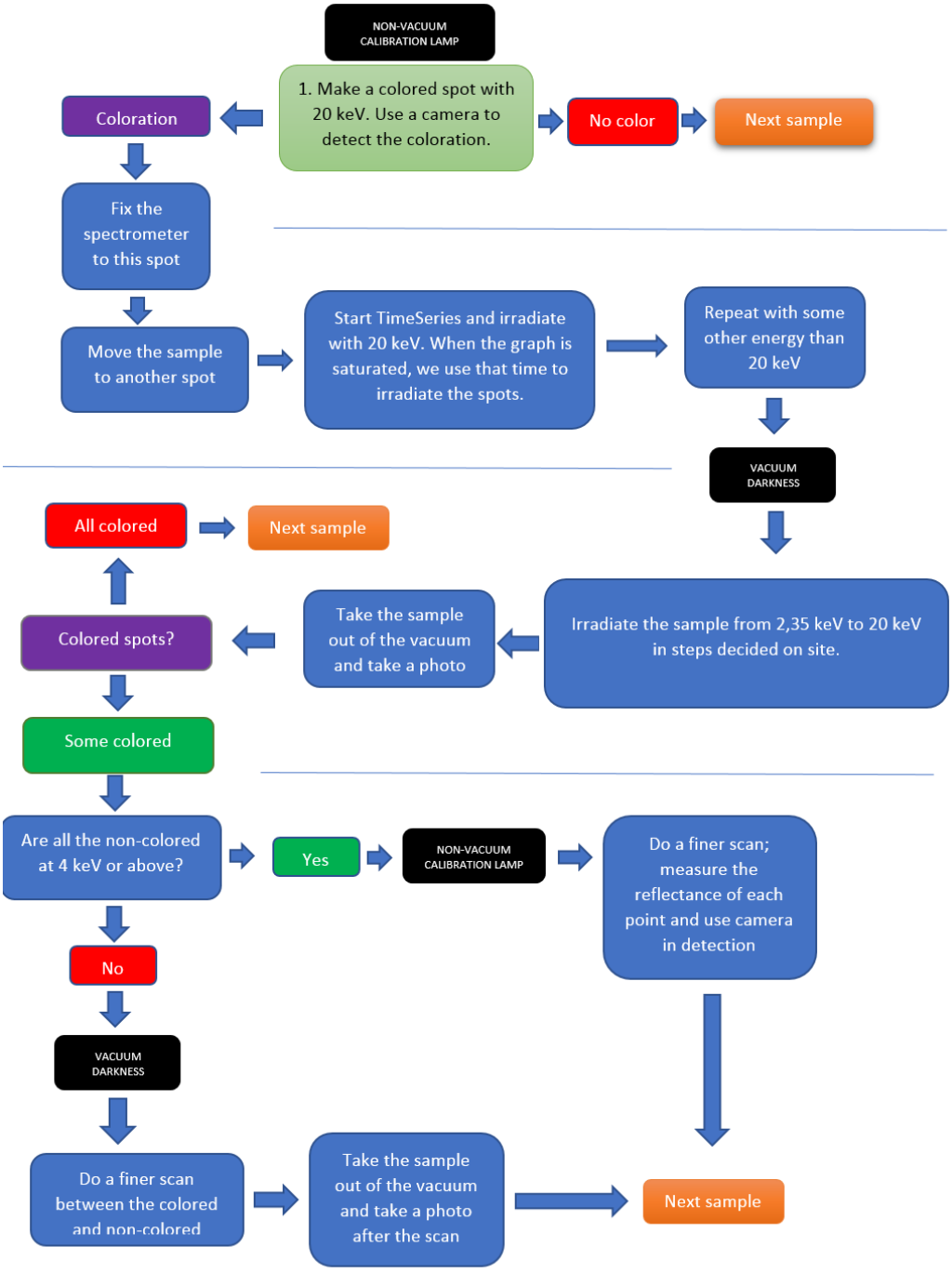

Figure 28. The sample measurement procedure at KIT.

Since X-rays attenuate in air [75], the exposures in the subsequent measurements were carried out in vacuum conditions. With the $(Li,Na)_8Al_6Si_6O_{24}(Cl,S)_2$:Ti (2 mol-%) sample,

the spectrum's integral vs. time measurements were carried out in air. The 7 casts shown in Table 12 were measured at KIT.

Table 12. Samples measured at KIT.

Sample	**ID**
$(Li,Na)_8Al_6Si_6O_{24}(Cl,S)_2$:Ti (2 mol-%) 850 °C 48 h air + 850 °C 2 h N_2/H_2	LiNaHack
$Na_8Al_6Si_6O_{24}(Cl,Se)_2$ 750 °C 48 h air + 750 °C 2 h N_2/H_2	SeHack14
$(Na,Rb)_8Al_6Si_6O_{24}(Cl,S)_2$ 850 °C 48 h air + 850 °C 2 h N_2/H_2	RbHack16
$Na_8Al_6Si_6O_{24}(Cl,S)_2$ 850 °C 48 h air	NaHack19
$Na_8Al_6Si_6O_{24}(Cl,S)_2$ 850 °C 48 h air + 850 °C 2 h N_2/H_2	NaHack20
$Na_8Al_6Si_6O_{24}(Cl,S)_2$ 850 °C 48 h air + 850 °C 2 h N_2/H_2	IN4CL
$Na_8Al_6Si_6O_{24}(Br,S)_2$	IN2Br

3.4.1. $(Li,Na)_8Al_6Si_6O_{24}(Cl,S)_2$, focused beam

The sample LiNaHack was exposed to X-rays in focused (non-collimated) mode. First a time series measurement was carried out to see how different energies affect the coloration. The energies were 5.0, 10.0, 15.0 and 20.0 keV. The spectra for all exposures are presented in Figure 30, Figure 31, Figure 32 and Figure 33 with 3 minute intervals. The spectra not only reveal that the X-ray-induced coloration deepens as a function of time, but interestingly also provide evidence that X-rays are possibly down-converted by the material which exhibits luminescence in the UV region upon irradiation, with 10 keV energy having the most pronounced effect. Since the LS-1 Cal lamp does not emit much UV light (Figure 29), the measurements are not precise in that area, yet it is qualitatively valid to state that there is indeed UV/violet/blue luminescence excited by the X-rays.

Because the reflectance spectra's baselines fluctuate between the measurements, they need to be translated to a standard height. According to Figure 29 it is most sensible to set the baseline in the 800−1000 nm region rather than at the 350−450 nm region, because the amount of IR radiation coming from the calibration lamp is much greater than the UV radiation, i.e. the IR region provides more precision than the UV region.

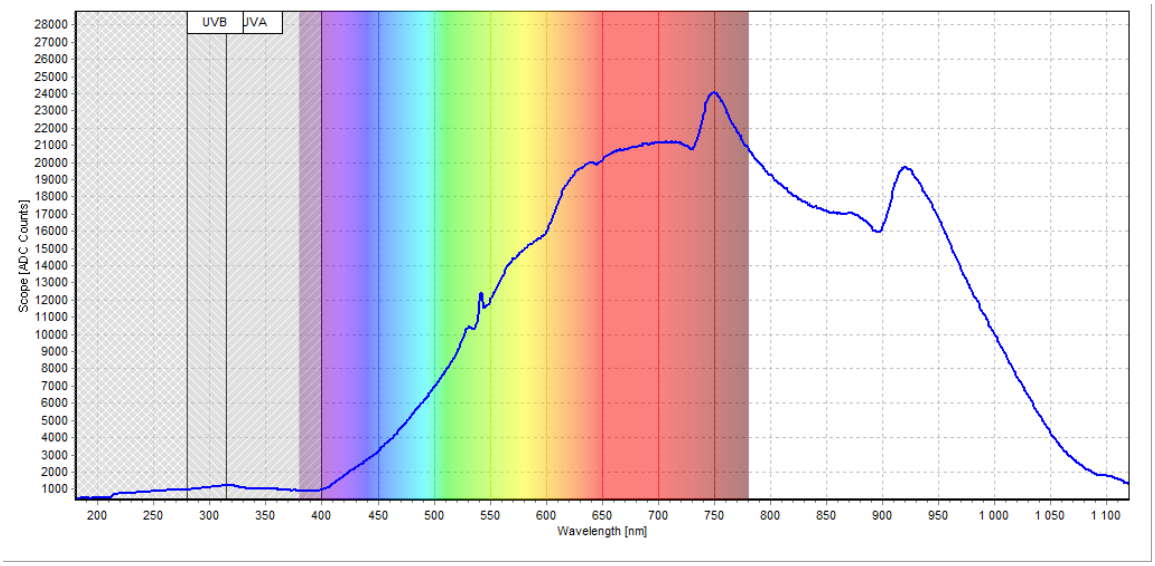

Figure 29. The LS-1 Cal lamp's spectrum measured with the HS-TEC spectrometer.

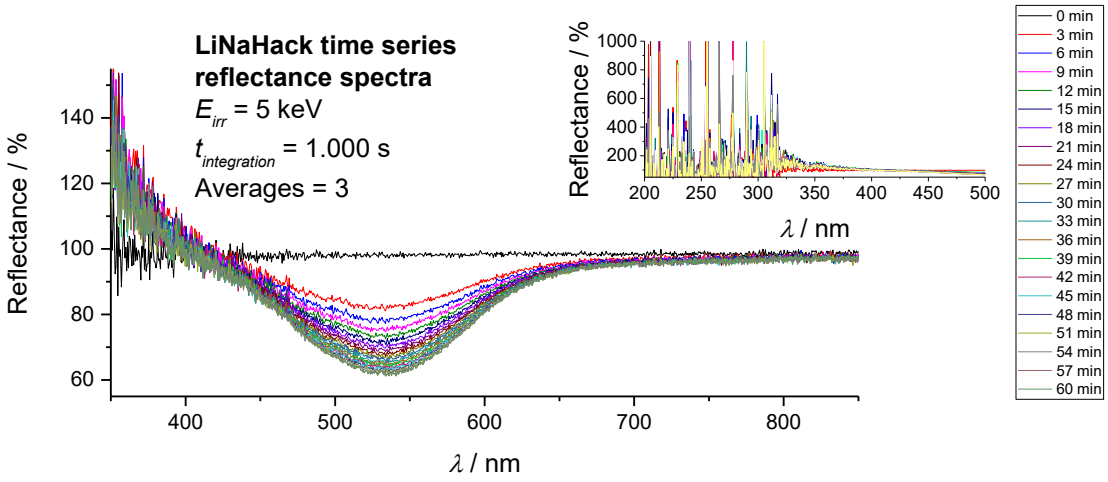

Figure 30. LiNaHack's 5 keV X-ray exposure monitored with reflectance measurements. Inset: the high-energy UV region. Unexposed part of the tape next to the exposed part was used as the white reference.

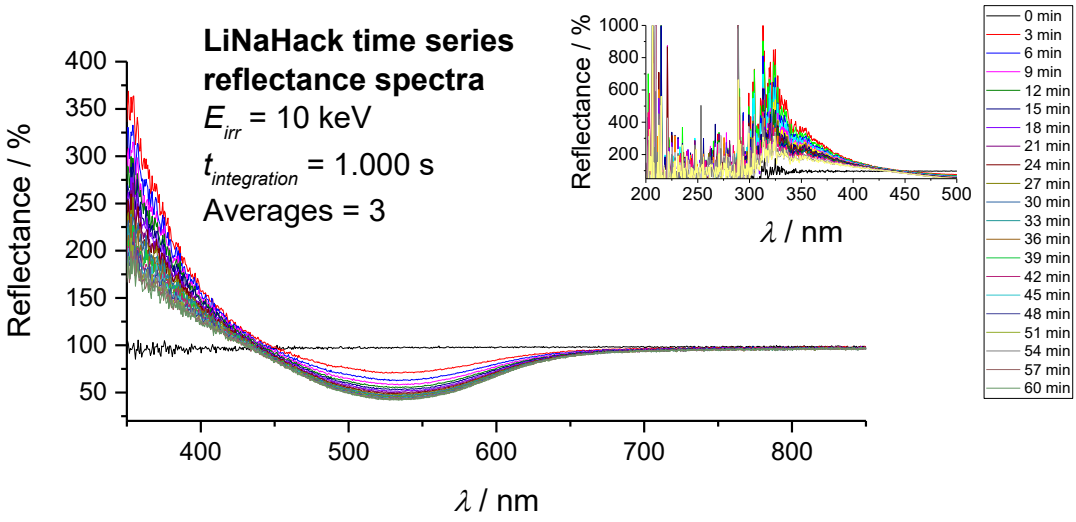

Figure 31. LiNaHack's 10 keV X-ray exposure monitored with reflectance measurements. Inset: the high-energy UV region. Unexposed part of the tape next to the exposed part was used as the white reference.

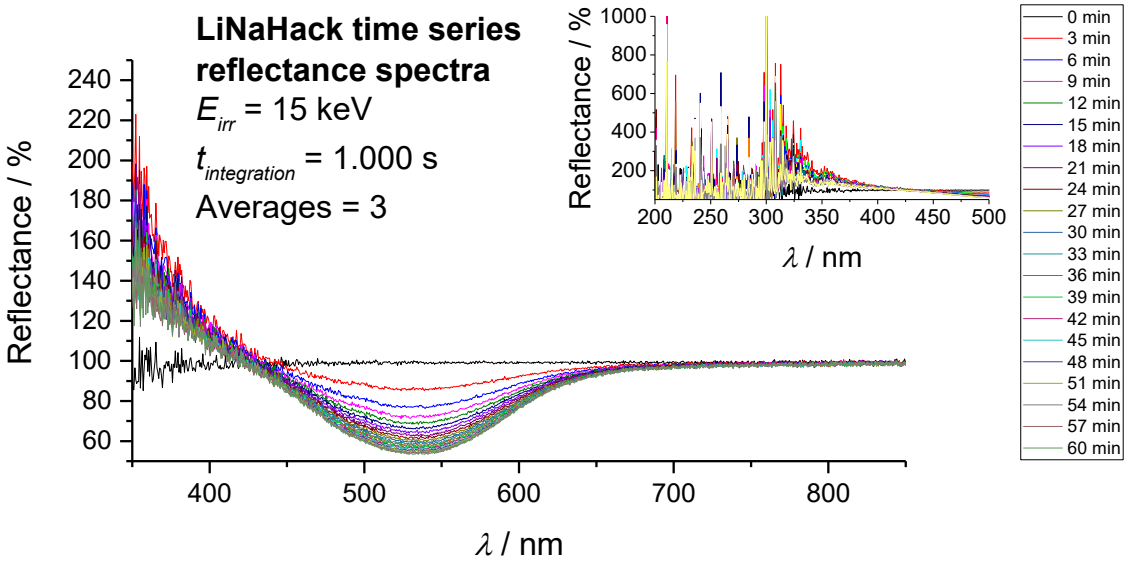

Figure 32. LiNaHack's 15 keV X-ray exposure monitored with reflectance measurements. Inset: the high-energy UV region. Unexposed part of the tape next to the exposed part was used as the white reference.

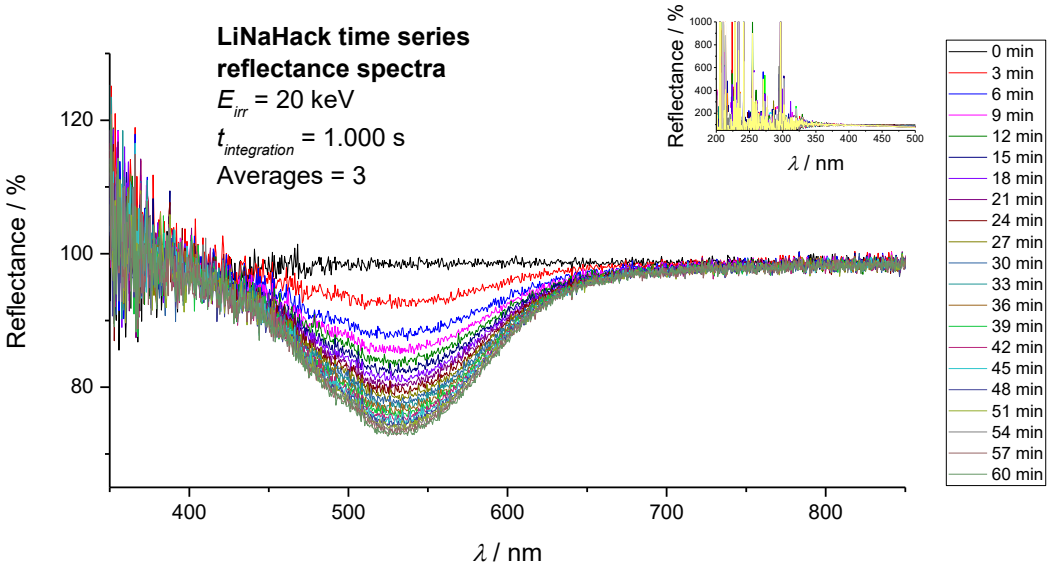

Figure 33. LiNaHack's 20 keV X-ray exposure monitored with reflectance measurements. Inset: the high-energy UV region. Unexposed part of the tape next to the exposed part was used as the white reference.

To calculate how much the color changes per one photon, a baseline treatment was done for all the reflectance spectra: the integral considered is the area residing between the baseline (100 % reflectance) and the spectrum in question (Figure 34). This treatment ultimately gives the value of how large the change in the integral is per one absorbed photon, shown in Equation 6. The higher the value, the more one photon colors the material.

$$\text{Color change efficiency} = \frac{\int_{519.66\ \text{nm}}^{540.68\ \text{nm}} 100\ \%\ \text{reflectance} - \int_{519.66\ \text{nm}}^{540.68\ \text{nm}} \text{sample}}{\text{Absorbed photons}} \qquad \text{(Eq. 6)}$$

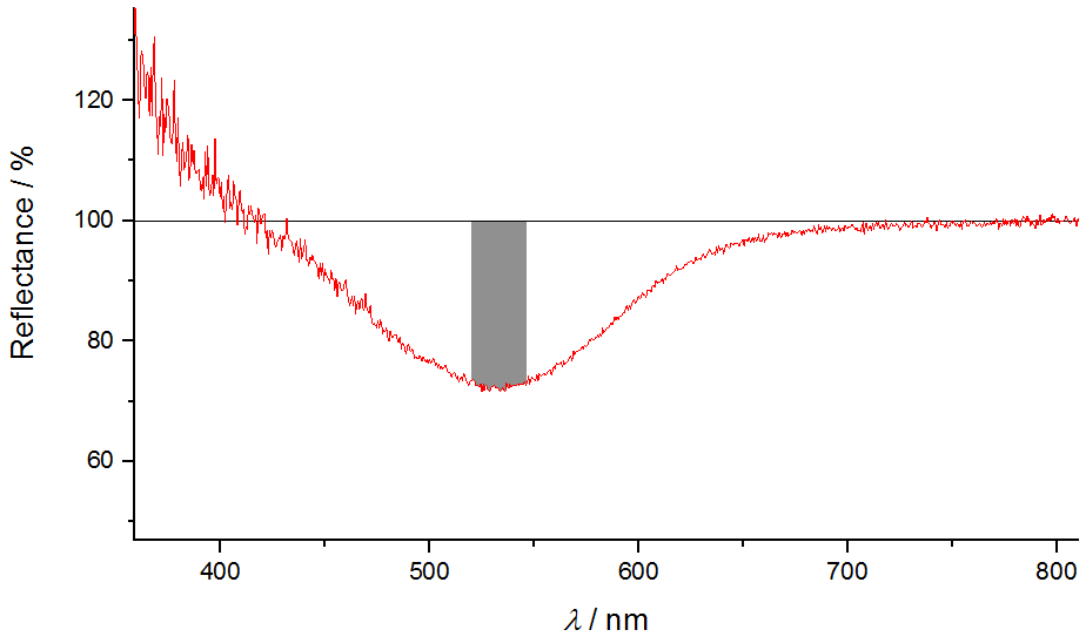

Figure 34. An example reflectance spectrum for illustrative purposes. The grey area between the baseline (519.66−540.68 nm, 100 % reflectance) and the spectrum (519.66−540.68 nm) is used in the calculations. This is the BL-corrected integral.

Figure 35 shows how the reflectance spectrum's integral changes when the sample is exposed to X-rays with the different energies, and Figure 36 shows how much the integral changes with one absorbed photon at each energy level. The absorbed photon values are taken from the synchrotron's measurement data.

According to Figure 35 and Figure 36, the energy causing the most intense color is 20 keV, while 5 keV produces the faintest coloration. This can be justified by imagining it with the measured data:

1. 180 seconds after opening the X-ray shutter the 519.66−540.68 nm integral changes 3600−3406 percent points = 194 pp (3600 pp being the baseline's integral) with 20 keV, while with 15 keV the change is 391 pp, with 10 keV 526 pp and with 5 keV 269 pp.
2. The absorbed photons are $5.6 \cdot 10^{11}$, $7.4 \cdot 10^{12}$, $2.0 \cdot 10^{13}$ and $1.4 \cdot 10^{13}$, respectively.
3. Calculating the amount of color change per one absorbed photon gives $1.5 \cdot 10^{-9}$ pp per photon (20 keV), $3.0 \cdot 10^{-10}$ pp per photon (15 keV), $1.5 \cdot 10^{-10}$ (10 keV) and $1.1 \cdot 10^{-10}$ (5 keV). 20 keV has the highest pp change per photon, thus causing most

coloration per one photon, and 5 keV causes the faintest. The calculations are also given in Table 14 and the data visualized in Figure 36's inset.

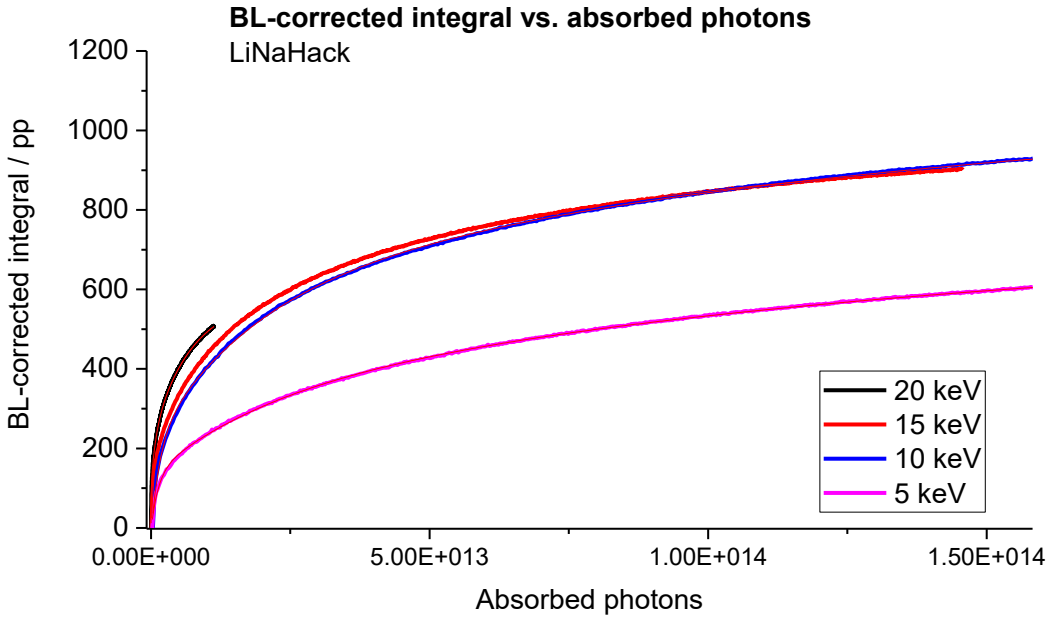

Figure 35. The baseline-corrected integral vs. absorbed photons at each energy level for LiNaHack, with fittings.

The equation for the fitted curves in Figure 35 and the parameters for each energy are given in Equation 7 and Table 13, respectively.

$$y = A_1 * e^{-\frac{x}{t_1}} + A_2 * e^{-\frac{x}{t_2}} + A_3 * e^{-\frac{x}{t_3}} + y_0 \qquad \text{(Eq. 7)}$$

Table 13. Each energy level's curve (Figure 35) fitting parameters for the Equation 7.

	20 keV		15 keV		10 keV		5 keV	
	Value	Standard error	Value	Standard error	Value	Standard error	Value	Standard error
y_0	579.14878	1.0159	958.86918	0.86544	1074.74096	0.47244	741.54066	0.84208
A_1	-115.53097	1.24266	-198.39748	2.64574	-224.08753	3.05452	-137.8138	1.69323
t_1	6.1E+10	1.22E+09	5.21E+11	1.14E+10	1.59E+12	4.08E+10	1.28E+12	2.77E+10
A_2	-110.5979	0.79147	-303.2021	1.35842	-366.35893	1.58965	-419.60162	0.76281

t_2	8.27E+11	1.2E+10	9.91E+12	8.03E+10	1.83E+13	1.66E+11	1.41E+14	9.8E+11
A_3	-359.33691	0.40085	-478.2771	0.94719	-496.7794	1.25362	-189.0961	1.17243
t_3	7.06E+12	5.5E+10	6.87E+13	4.53E+11	1.3E+14	6.12E+11	2.08E+13	2.26E+11
Reduced Chi-sqr	1.73583		4.45482		6.9489		2.61092	
R-Square (COD)	0.99982		0.99983		0.99977		0.99985	
Adj. R-Square	0.99982		0.99983		0.99977		0.99985	

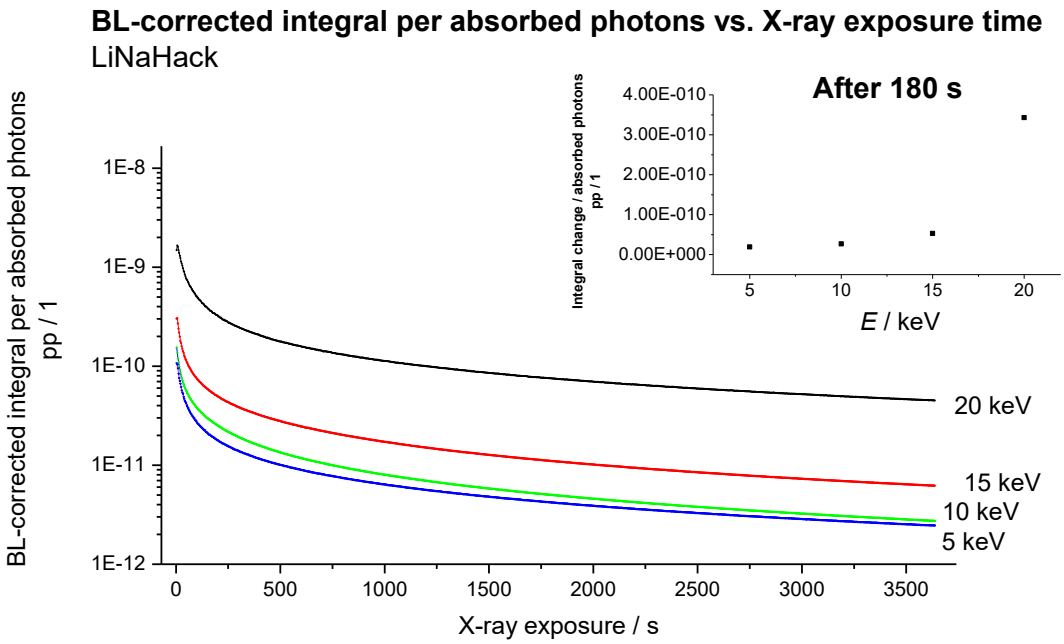

Figure 36. Baseline-corrected integral per absorbed photons during the measurements for LiNaHack. The inset shows the color-changing ability for each energy after an example of 180 s of exposure: 5 keV < 10 keV < 15 keV < 20 keV. The data points in the inset are enlisted numerically in Table 14.

Table 14. Calculations for the coloration efficiency for each energy (after 180 s of X-ray exposure).

***E* / keV**	**BL-corrected integral**	**Absorbed photons**	**BL-corrected integral / absorbed photons**
20	194	5.60E+11	3.46E-10
15	391	7.40E+12	5.28E-11
10	526	2.00E+13	2.63E-11
5	269	1.40E+13	1.92E-11

After the time series measurement, the sample was exposed in dark vacuum to finer energy ranges presented in Figure 37. Each point was exposed to X-rays for 297 s. The photon fluxes were recorded, and the spots were photographed immediately after taking the sample out of the chamber. The reflectance spectra (Figure 38) were measured after 1 week, for which the samples were kept in darkness until the measurement. Besides a small dimple forming at 510 nm, the spectra do not have any anomalies.

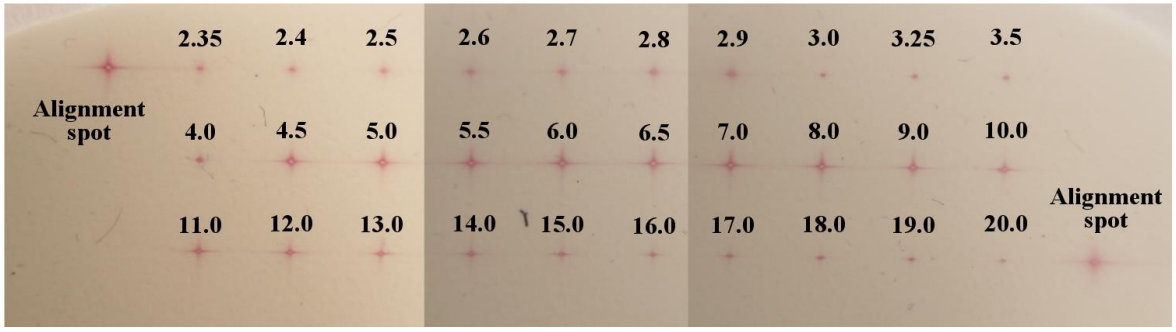

Figure 37. LiNaHack after 5-minute exposures to focused X-ray beams. Numerical values given in keV. Photographed with a Canon EOS 1100D (FW 1.0.4) + Canon EF-S 18–55mm f/3.5–5.6 III + extension tubes, focal length 50 mm, shutter speed ½ s, aperture f/3.5, sensitivity ISO 100, color space sRGB, white balance incandescent, light source an incandescent lamp.

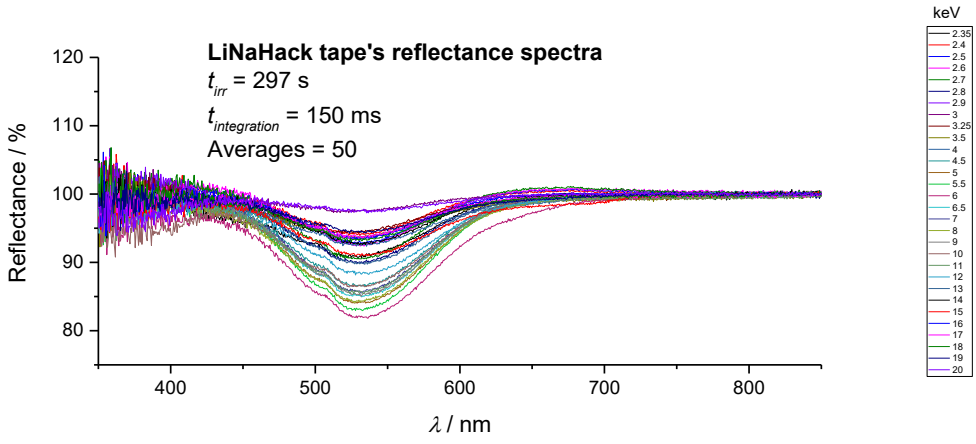

Figure 38. Reflectance spectra measured from the sample tape (Figure 37) after 1 week from the exposures. All the spectra are normalized to 100 % reflectance at 800 nm. Unexposed part of the tape next to the exposed part was used as the white reference.

The efficiency of color change for each energy (Figure 39, blue series) was calculated with Equation 6. Figure 39 is in accordance with Figure 36: 5 keV X-ray photons induce tenebrescence the least, while 20 keV induces it the most in $(Li,Na)_8Al_6Si_6O_{24}(Cl,S)_2$:Ti (2 mol-%). There is a jump in coloration efficiency after 2.9 keV, yet it comes back to the pre-2.9 keV level after 4.0 keV. This can be due to photon flux measurement errors declared by KIT or the fact that the photon fluxes are on a different order of magnitude, which creates variance.

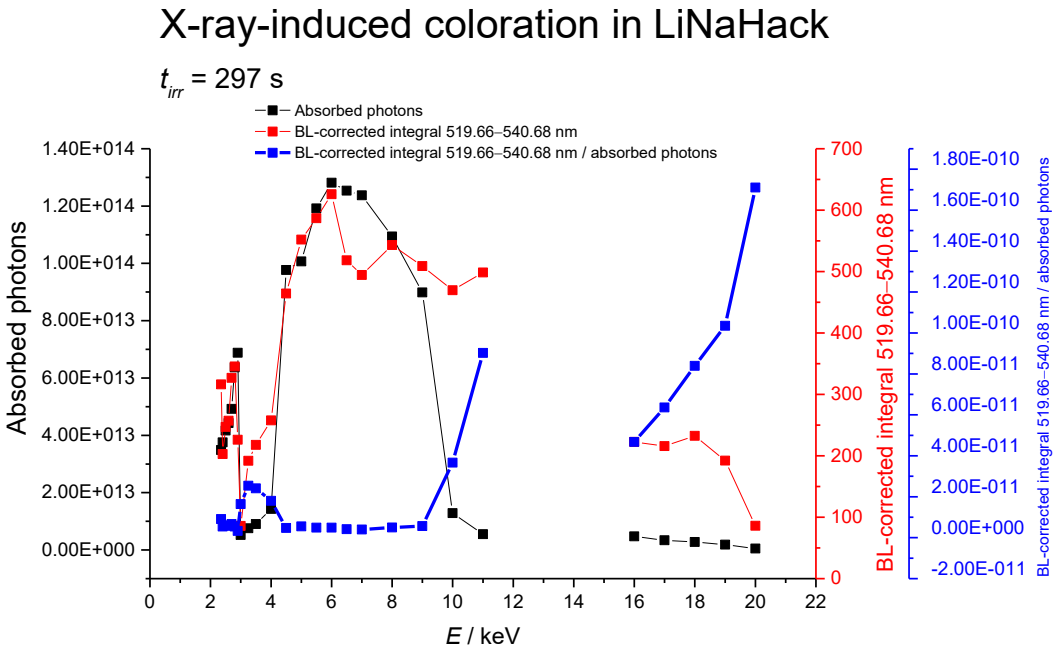

Figure 39. The coloration efficiency of the X-ray-exposed LiNaHack (Figure 37). Outliers and outright false data points (e.g. negative absorbed photons) have been removed from the set.

3.4.2. $Na_8Al_6Si_6O_{24}(Cl,Se)_2$, collimated beam

Se-hackmanite's spectra were recorded as a time series measurement in air using 7 keV X-rays for 5 minutes. Measuring the reflectance spectra of the 180-s exposures presented in Figure 40 proved not to be successful, thus aren't included.

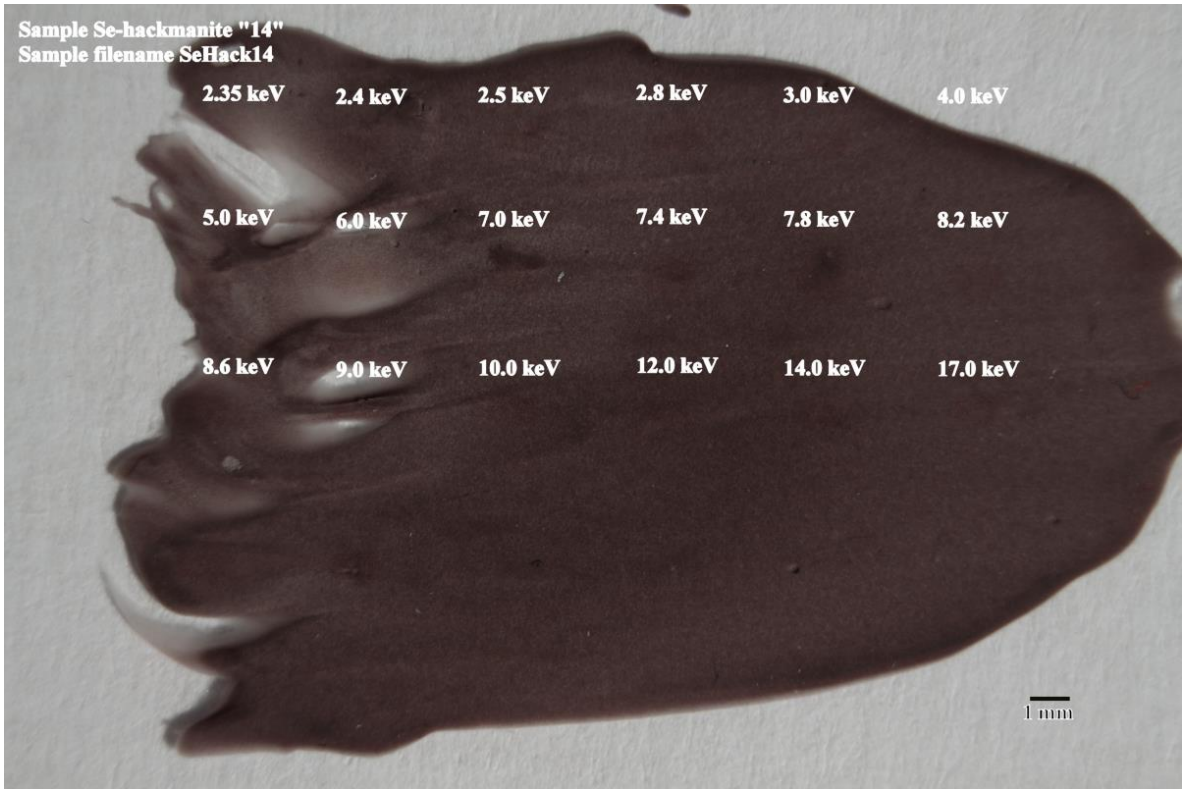

Figure 40. The SeHack14 sample tape exposed to collimated X-ray beams for 180 s. Photographed with a Canon EOS 1100D (FW 1.0.4) + Canon EF-S 18–55mm f/3.5–5.6 III + extension tubes, focal length 50 mm, shutter speed ½ s, aperture f/3.5, sensitivity ISO 100, color space sRGB, white balance incandescent, light source an incandescent lamp.

Se-hackmanite's reflectance spectrum differs from hackmanites that have sulfur in selenium's place: as can be seen from Figure 41, the reflectance spectrum has two pits of interest with minima at 570 nm and 725 nm, contrary to $Na_8Al_6Si_6O_{24}(Cl,S)_2$'s circa 550 nm minimum. Figure 42 shows the ratio of the BL-corrected integrals from both pits during the 5-minute time series exposure experiment. The lower-energy pit (665.19−865.99 nm) shows a larger reflectance contraction per one absorbed 7 keV X-ray photon as can be verified from Figure 41.

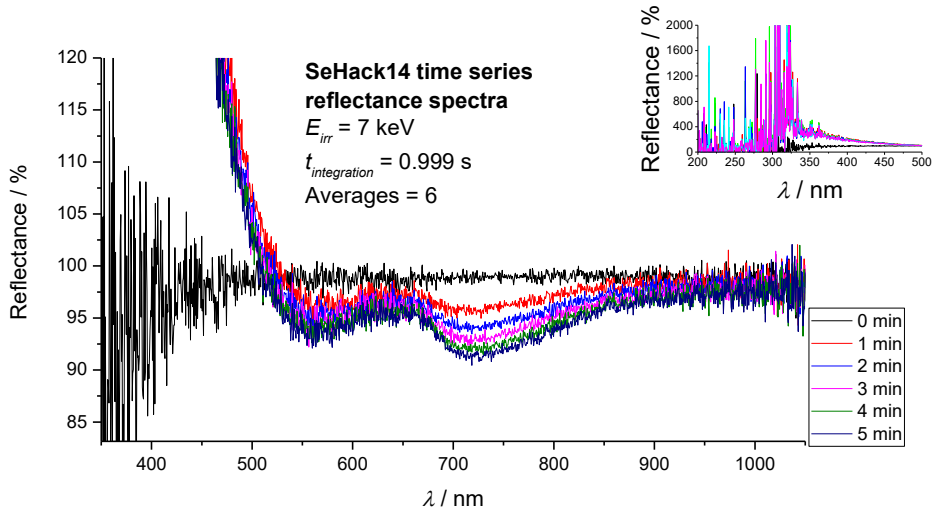

Figure 41. SeHack14's spectra with 1-minute intervals. Inset: high-energy UV region. Spectrometer's integration time was 0.999 s with 6 averages per measurement. Unexposed part of the tape next to the exposed part was used as the white reference.

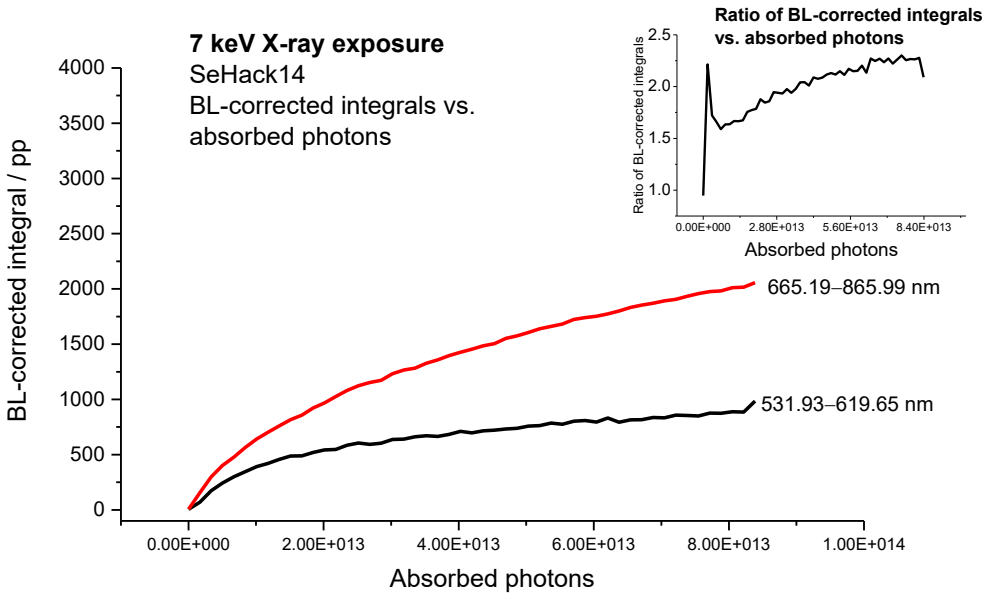

Figure 42. 7 keV X-ray exposure monitored with reflectance measurements on SeHack14: BL-corrected integral vs. absorbed photons. Inset: the ratio between the lower-energy and higher-energy pits in the reflectance spectra plotted against absorbed photons.

From the results it can be stated that selenium hackmanite changes its color during the X-ray exposure. Since the color of the sample is very dark, the color itself cannot be seen clearly, yet still the results indicate that there are vacancies where electrons are promoted by the X-rays.

3.4.3. $(Rb,Na)_8Al_6Si_6O_{24}(Cl,S)_2$, collimated beam

Rb-hackmanite RbHack16 was exposed to a collimated X-ray beam at each energy level in dark vacuum for 180 s. Figure 43 shows the tape after the exposures.

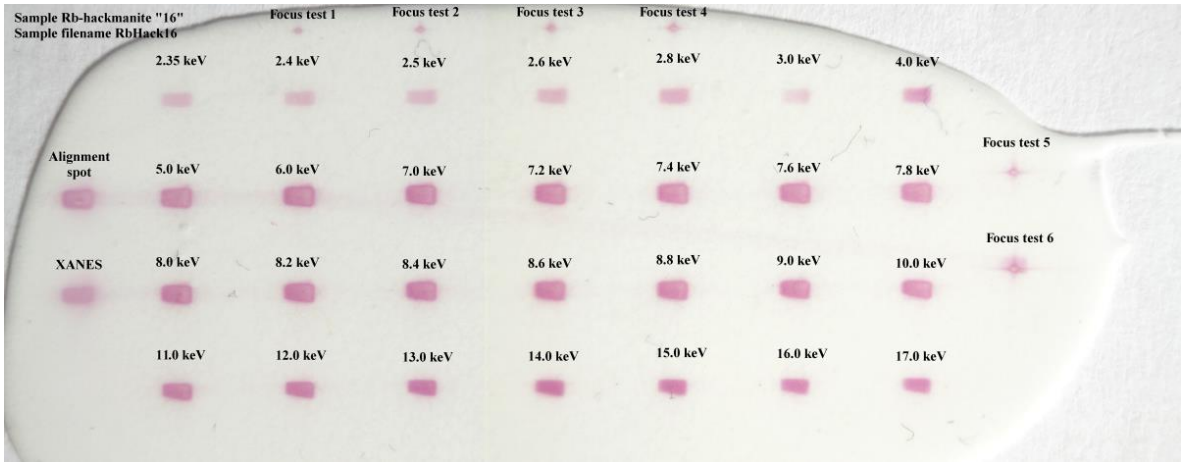

Figure 43. The RbHack16 sample tape exposed to collimated X-ray beams for 180 s at each energy level. Photographed with a Canon EOS 1100D (FW 1.0.4) + Canon EF-S 18–55mm f/3.5–5.6 III + extension tubes, focal length 50 mm, shutter speed ¼ s, aperture f/3.5, sensitivity ISO 100, color space sRGB, white balance incandescent, light source an incandescent lamp.

Figure 44 shows the reflectance spectra measured from the sample tape after 1 week from the exposures. Besides a small dimple forming at 495 nm, the spectra do not have any anomalies. In Figure 45 the absorbed photons, BL-corrected integrals and the BL-corrected integrals divided by the absorbed photons are shown for each keV level. The figure shows the same result as with LiNaHack's time series measurements: the coloration ability is 5 keV < 10 keV < 15 keV < 20 keV.

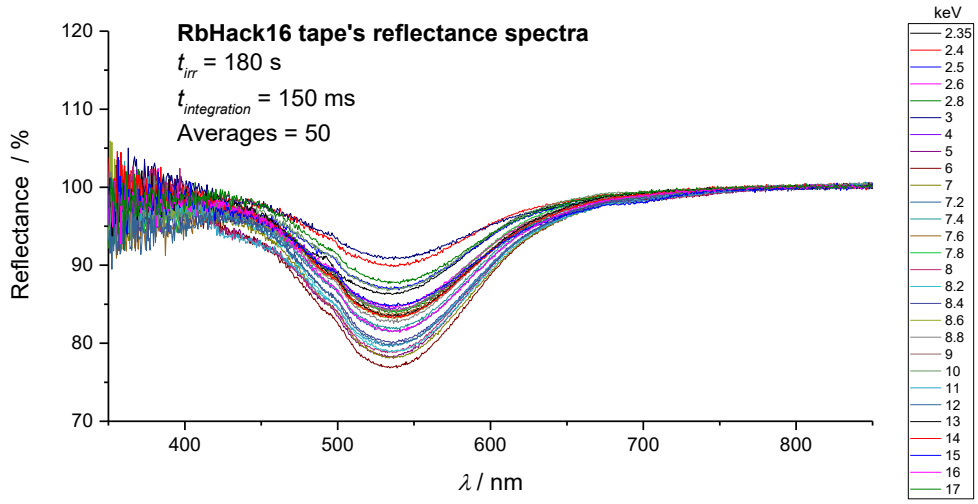

Figure 44. Reflectance spectra measured from the sample tape (Figure 43) after 1 week from the exposures. All the spectra are normalized to 100 % reflectance at 800 nm. Unexposed part of the tape next to the exposed part was used as the white reference.

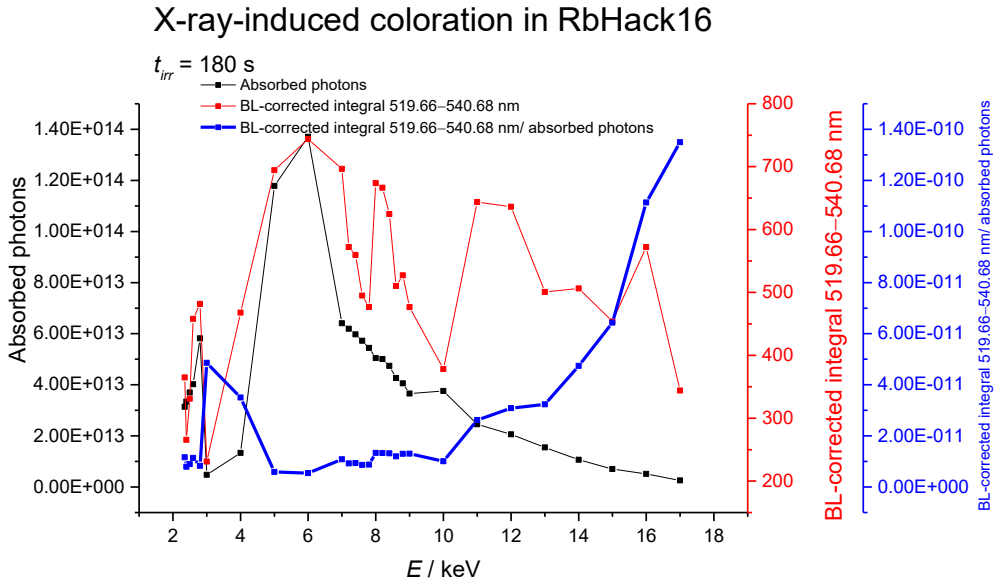

Figure 45. The coloration efficiency of the X-ray-exposed RbHack16 (Figure 43). The reflectance spectra were measured with integration time 150 ms and 50 averages per measurement.

3.4.4. $Na_8Al_6Si_6O_{24}(Cl,S)_2$, non-reduced, collimated beam

NaHack19 is the non-reduced hackmanite which, prior to X-ray exposure, was tested on a cathodoluminescence setup for the color-changing ability. The tenebrescence color is brownish (Figure 46). UV exposure is not enough to generate this coloration. The sample was exposed to a collimated X-ray beam at each energy level in dark vacuum for 180 s.

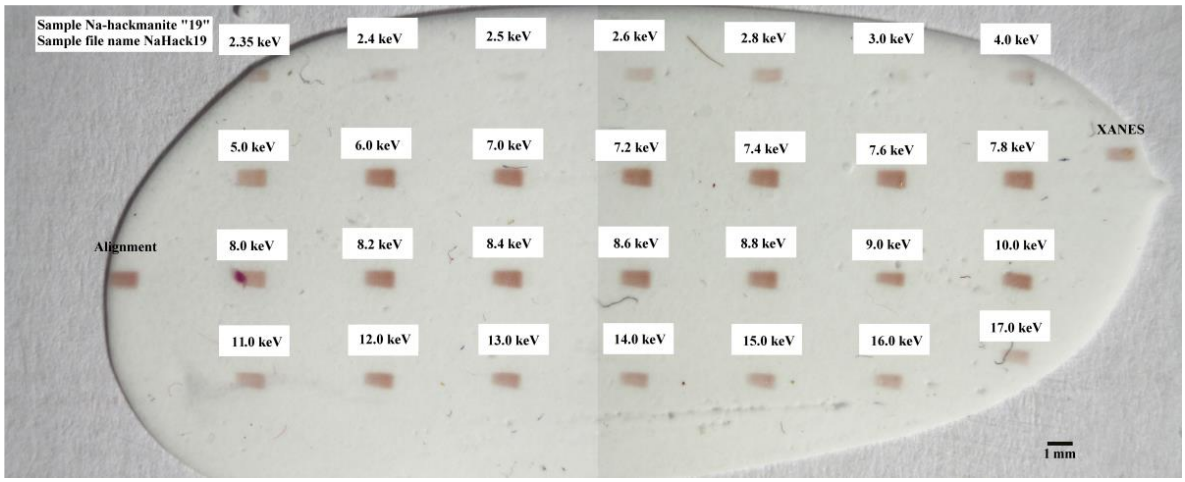

Figure 46. The NaHack19 sample tape exposed to collimated X-ray beams for 180 s at each energy level. Photographed with a Canon EOS 1100D (FW 1.0.4) + Canon EF-S 18–55mm f/3.5–5.6 III + extension tubes, focal length 50 mm, shutter speed 1/6 s, aperture f/3.5, sensitivity ISO 100, color space sRGB, white balance incandescent, light source an incandescent lamp.

In Figure 47 can be seen that the reflectance spectrum's minimum is located at 485 nm. Another light-absorbing minimum can be seen forming at 705 nm. There is a small local peak present at 505 nm.

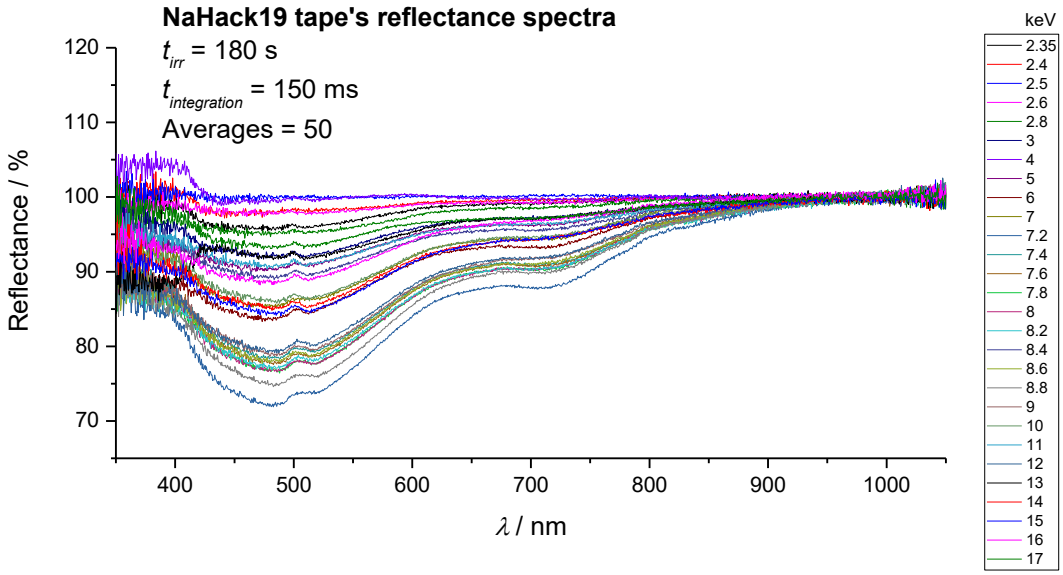

Figure 47. Reflectance spectra measured from the sample tape (Figure 46) after 1 week from the exposures. All the spectra are normalized to 100 % reflectance at 950 nm. Unexposed part of the tape next to the exposed part was used as the white reference.

In Figure 48 the blue series (BL-corrected integral / absorbed photons) show that the coloration ability is alike with LiNaHack and RbHack16 (5 keV < 10 keV < 15 keV < 20 keV). Due to the errors in the synchrotron's photon flux data, some points have been removed from the data series.

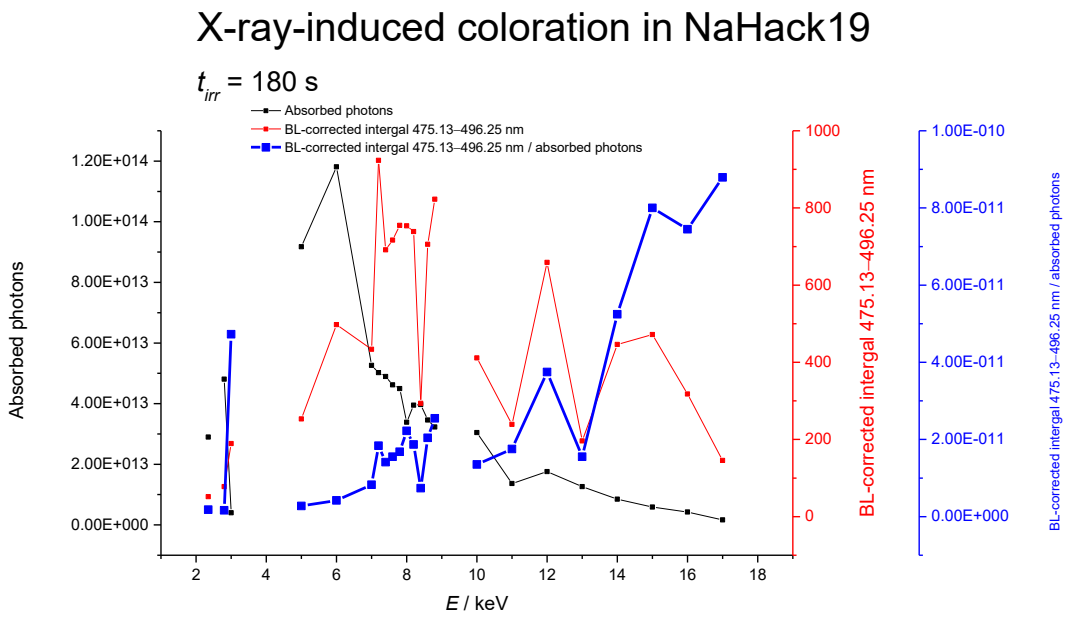

Figure 48. The coloration efficiency of the X-ray-exposed NaHack19 (Figure 46). Outliers and outright false data points (e.g. negative absorbed photons) have been removed from the set.

3.4.5. $Na_8Al_6Si_6O_{24}(Cl,S)_2$, reduced, collimated beam

NaHack20 tape was exposed to a collimated X-ray beam in dark vacuum for 180 s at each energy level seen in Figure 49. The coloration is strong at each energy level and the effects caused by the X-rays can be seen clearly. In addition to the energy level tests, an overexposure test was conducted on the sample to see whether a long exposure to X-rays has unexpected effects on the coloration. In the overexposure experiment, 8 spots were exposed to 6.5 keV X-rays for 200, 300, 400, 500, 600, 1200, 1800 and 3600 s. The 6.5 keV energy level was chosen for the fact that, after a visual survey *in situ*, the coloration for the other samples measured hitherto seemed relatively high at the 6−8 keV level.

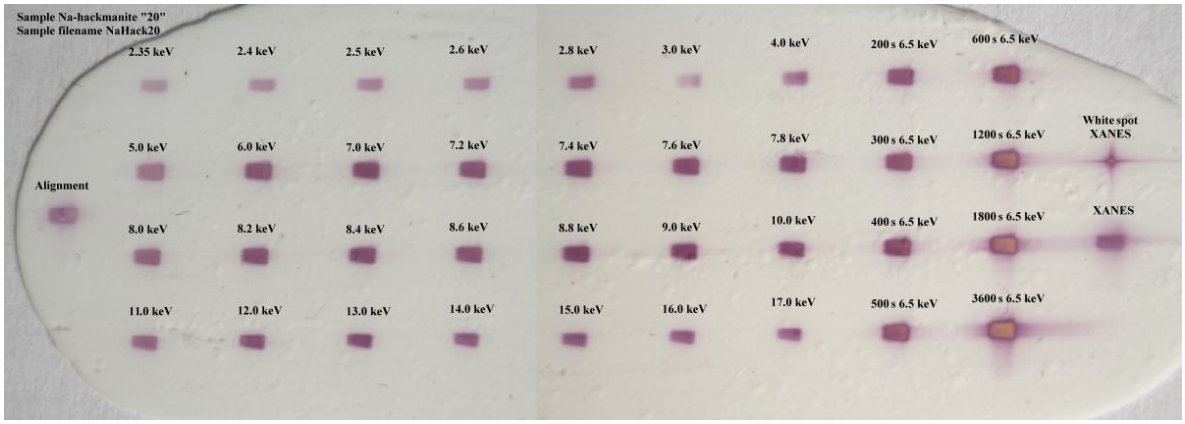

Figure 49. The NaHack20 sample tape exposed to collimated X-ray beams for 180 s at each energy level. An additional X-ray overexposure effect test was executed for 200, 300, 400, 500, 600, 1200, 1800 and 3600 seconds at 6.5 keV. Images taken with a Canon EOS 1100D (FW 1.0.4) + Canon EF-S 18–55mm f/3.5–5.6 III + extension tubes, focal length 50 mm, shutter speed ¼ s, aperture f/3.5, sensitivity ISO 100, color space sRGB, white balance incandescent, light source an incandescent lamp.

In Figure 50 the reflectance spectra show the minimum forming at 540 nm, but a small peak is present in all measurements at 680 nm. The 2.35 keV measurement has a peak at 430 nm, but this is due to a white reference-matching error in the measurement. Figure 51 shows the coloration ability for different keV levels. The results consolidate the conclusions from LiNaHack, RbHack16 and NaHack19, i.e. 20 keV's ability to induce the coloration is the strongest, and lowering the level to 15 keV, 10 keV and 5 keV weakens the coloration.

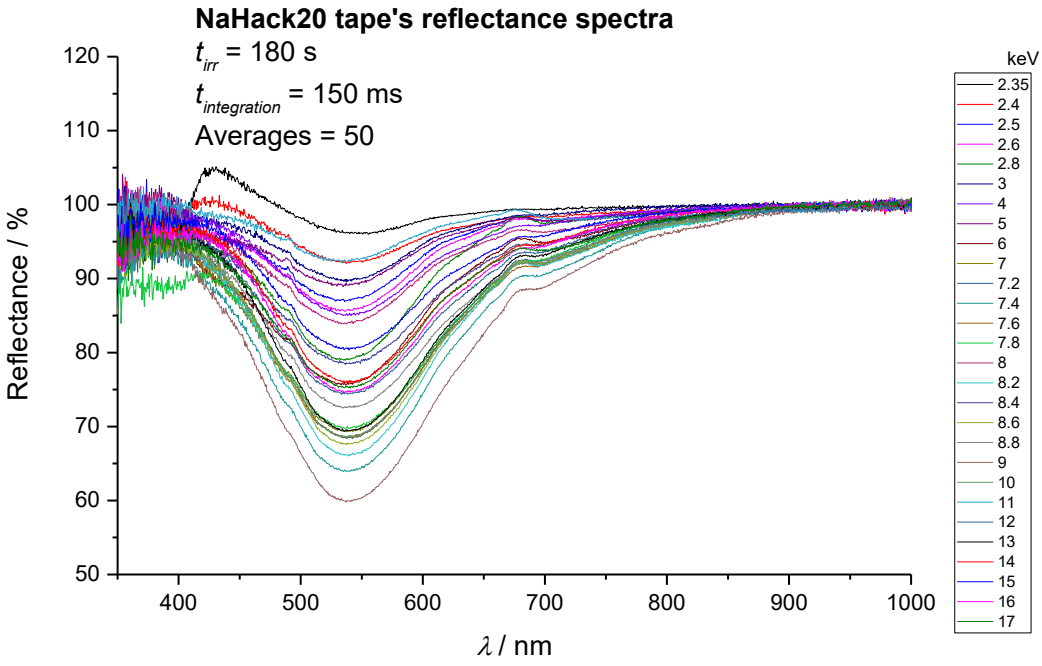

Figure 50. Reflectance spectra measured from the sample tape (Figure 49) after 1 week from the exposures. All the spectra are normalized to 100 % reflectance at 950 nm. Unexposed part of the tape next to the exposed part was used as the white reference.

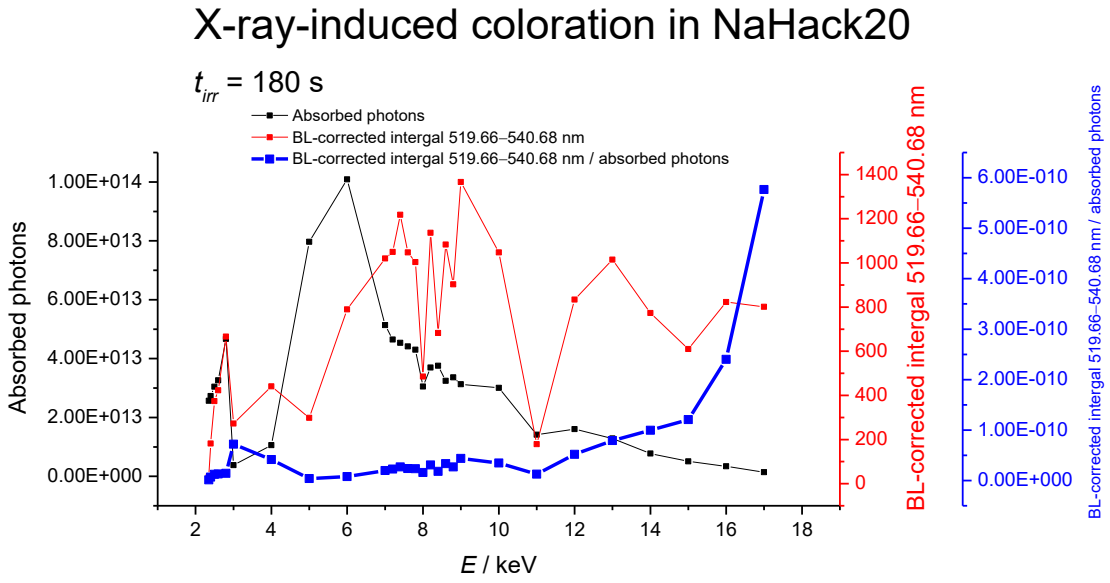

Figure 51. The coloration efficiency of the X-ray-exposed NaHack20 (Figure 49).

The overexposure test spots' reflectance spectra were measured 1 week after the exposure. The results are shown in Figure 52, where it can be noticed that while the global minimum (between 350 and 1050 nm) is at 540 nm, there are some local peaks at 500 nm and 680 nm. The spots exposed for 1800 and 3600 s have another absorbing minimum at 725 nm.

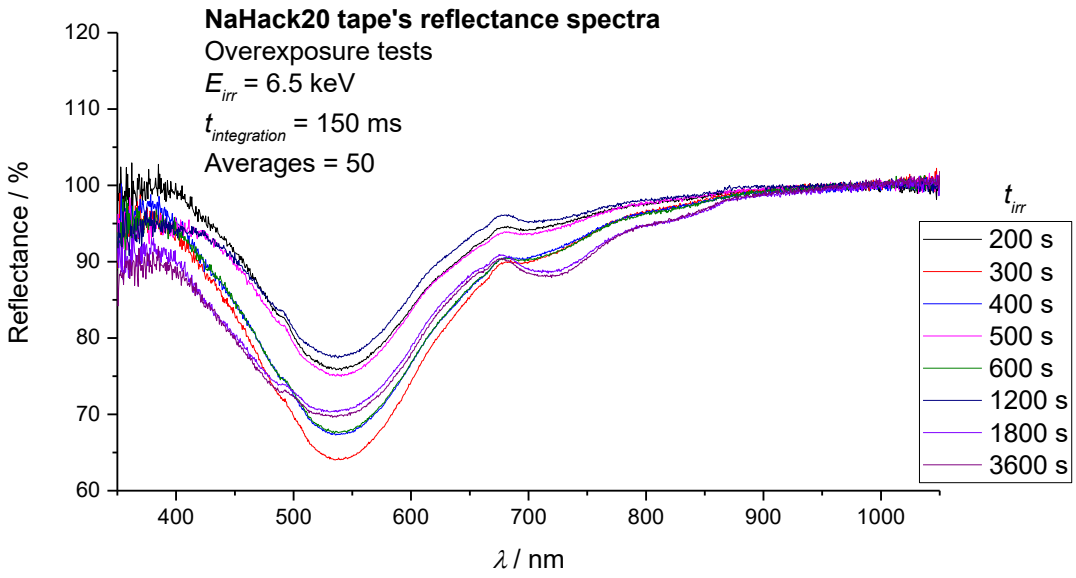

Figure 52. The reflectance spectra of the X-ray overexposure test performed on the NaHack20 sample. Measured 1 week after the exposure, normalized to 100 % at 950 nm. Unexposed part of the tape next to the exposed part was used as the white reference.

Figure 53 shows the coloration behavior of the overexposed test spots. A noticeable feature is that the long exposure has an adverse effect on the coloration: the longer the sample is irradiated, the fainter the coloration of interest (the 540 nm minimum in the reflectance spectrum) gets. This is in accordance with Figure 49 which shows the overexposed points as fainter than others, especially the 3600-s exposed version.

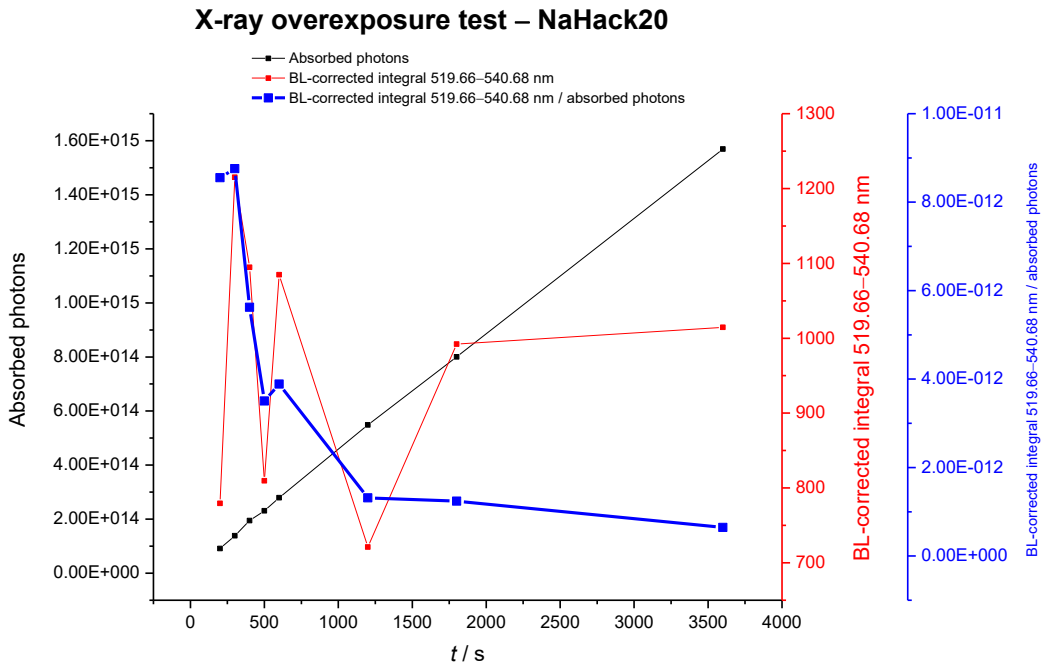

Figure 53. X-ray overexposure tests performed on NaHack20 (Figure 49).

The sample tape was sent to the University of Turku's Department of Geography and Geology for a micro-XRF sweep test shown in Figure 54. The micro-XRF results indicate that there are no apparent fluctuations in the elemental composition throughout the spot. The spot can no longer change color upon X-ray exposure, meaning that the reason lies outside the change of the sample's elemental composition.

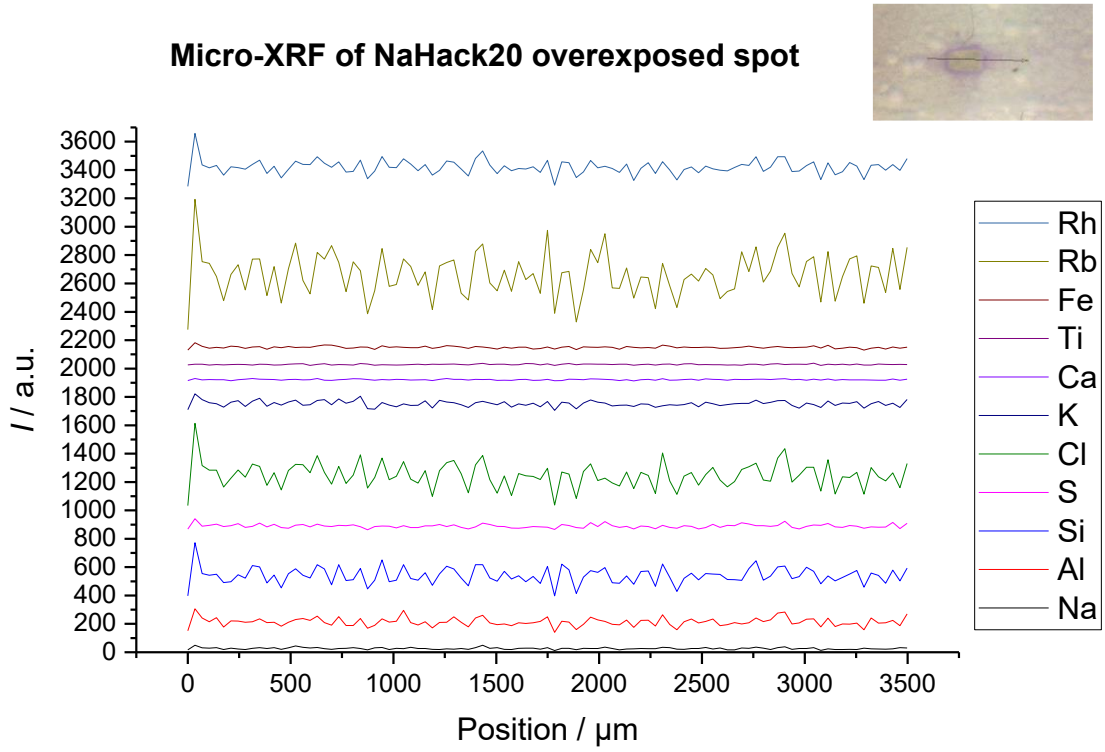

Figure 54. Micro-XRF line sweep conducted on one of the overexposed spots in NaHack20.

3.4.6. $Na_8Al_6Si_6O_{24}(Cl,S)_2$, reduced, focused beam

The third $Na_8Al_6Si_6O_{24}(ClS)_2$ sample IN4CL was exposed to a focused beam in dark vacuum for 180 s at each energy level seen in Figure 55. The tape shows some overexposed spots generated with energy levels with high photon fluxes. In Figure 56 the reflectance spectra show the minimum forming at 530 nm, but a small peak is present in all measurements at 500 nm. Figure 57 shows the coloration ability for different keV levels in the sample. While 5 keV shows to possess a stronger color-changing ability than 10 keV (efficiency numbers are 1.7863 and 1.7478, respectively), the results show that 20 keV photons have the strongest ability to color the sample. 15 keV point was removed with some others due to the erroneous values in the photon fluxes given by the synchrotron.

While the 5 keV and 10 keV coloration results' ratio is different than with other samples, such a small difference can be explained with variance in the reflectance measurements due to the overexposed spot in the center of the 5 keV spot (Figure 55).

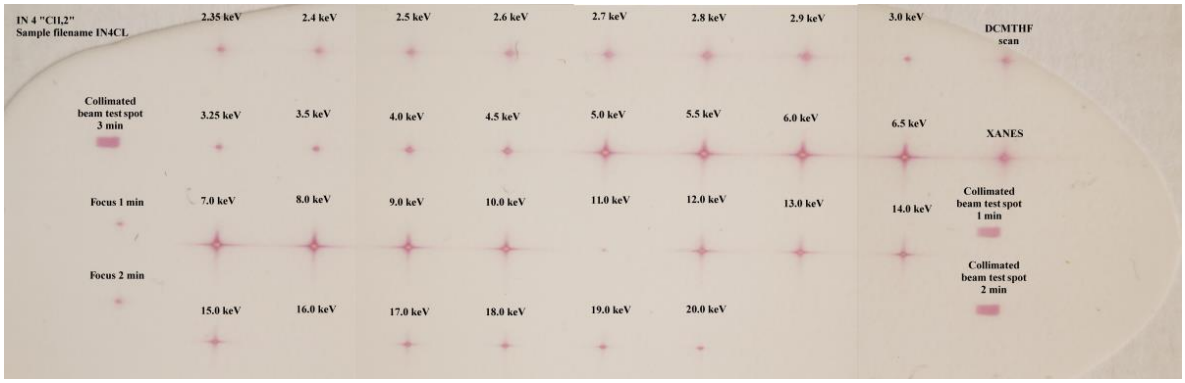

Figure 55. The IN4CL sample tape exposed to focused X-ray beams for 180 s at each energy level. Photographed with a Canon EOS 1100D (FW 1.0.4) + Canon EF-S 18–55mm f/3.5–5.6 III + extension tubes, focal length 50 mm, shutter speed 0.8 s, aperture f/3.5, sensitivity ISO 100, color space sRGB, white balance incandescent, light source an incandescent lamp.

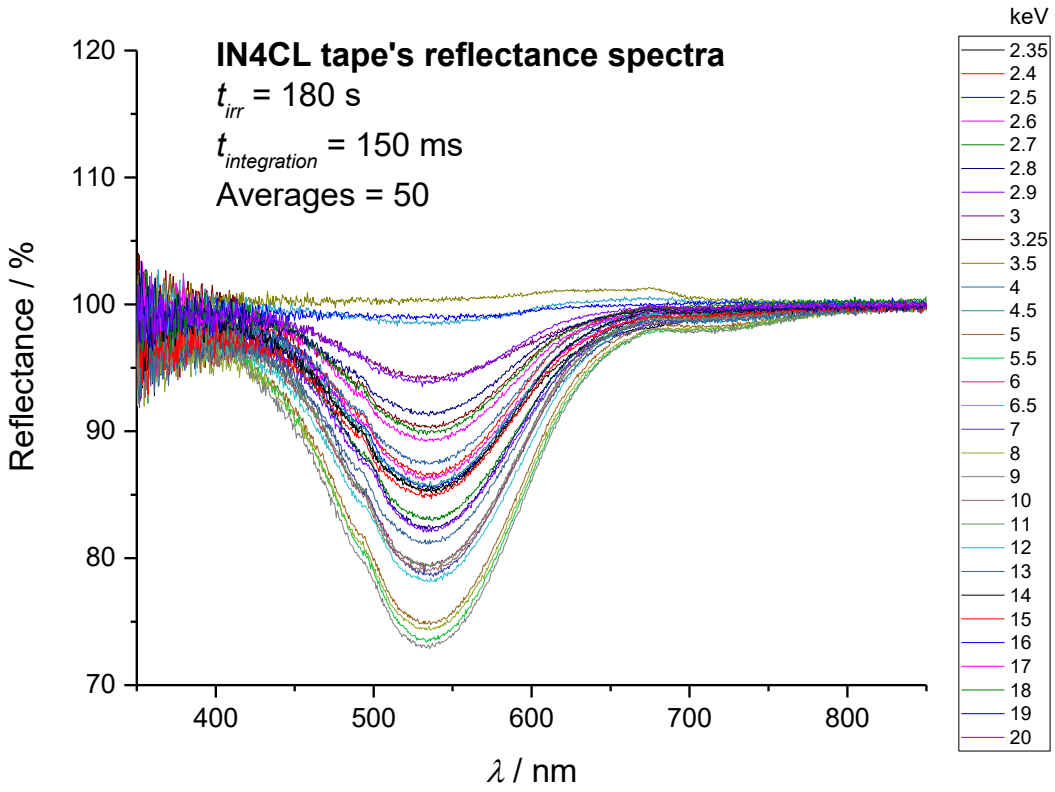

Figure 56. Reflectance spectra measured from the sample tape (Figure 55) after 1 week from the exposures. All the spectra are normalized to 100 % reflectance at 850 nm.

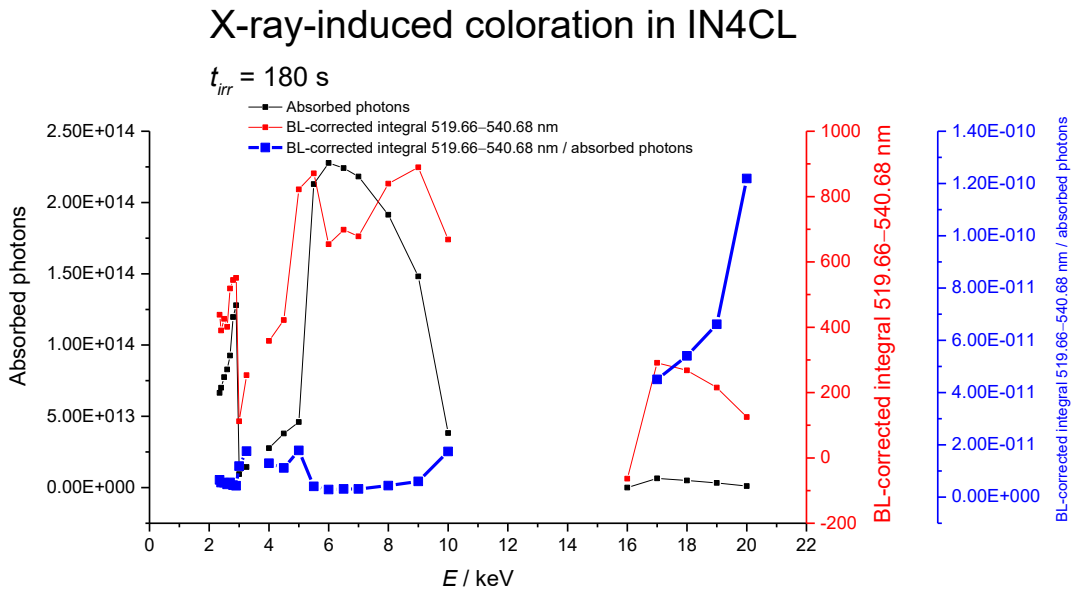

Figure 57. The coloration efficiency of the X-ray-exposed IN4CL (Figure 55). Outliers and outright false data points (e.g. negative absorbed photons) have been removed from the set.

3.4.7. $Na_8Al_6Si_6O_{24}(Br,S)_2$, collimated beam

The IN2Br sample was exposed to a focused beam in dark vacuum for 180 s at each energy level seen in Figure 58. The induced color is bright and strong, which can be noticed from the reflectance spectra's levels in Figure 59. The reflectance spectra are smooth and with no apparent anomalies, and the deep minimum forms at 550 nm.

Figure 60 shows the coloration ability for different keV levels in the sample. In this sample, the coloration efficiency is in accordance with LiNaHack, RbHack16, NaHack19 and NaHack20, meaning that the coloration grows from 5 keV to 20 keV with 5 keV intervals.

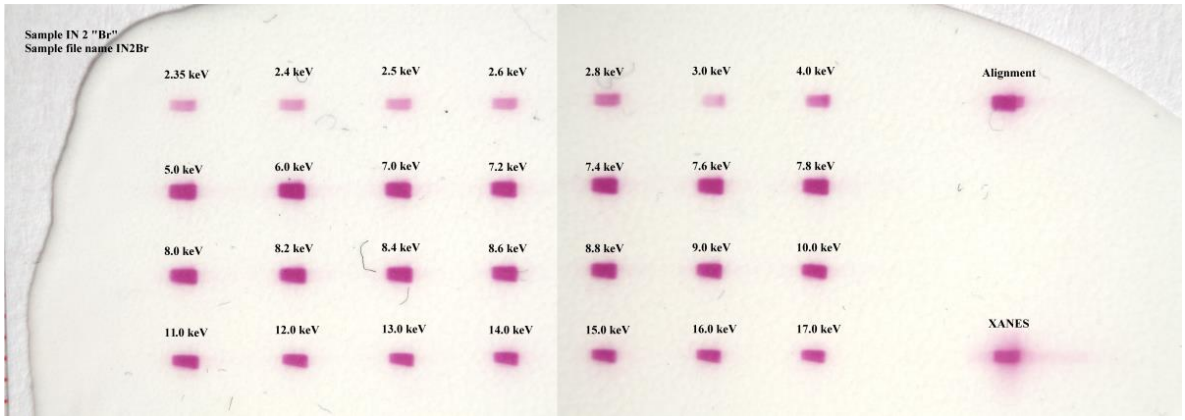

Figure 58. The IN2Br sample tape exposed to collimated X-ray beams for 180 s at each energy level. Photographed with a Canon EOS 1100D (FW 1.0.4) + Canon EF-S 18–55mm f/3.5–5.6 III + extension tubes, focal length 50 mm, shutter speed ½ s, aperture f/3.5, sensitivity ISO 100, color space sRGB, white balance incandescent, light source an incandescent lamp.

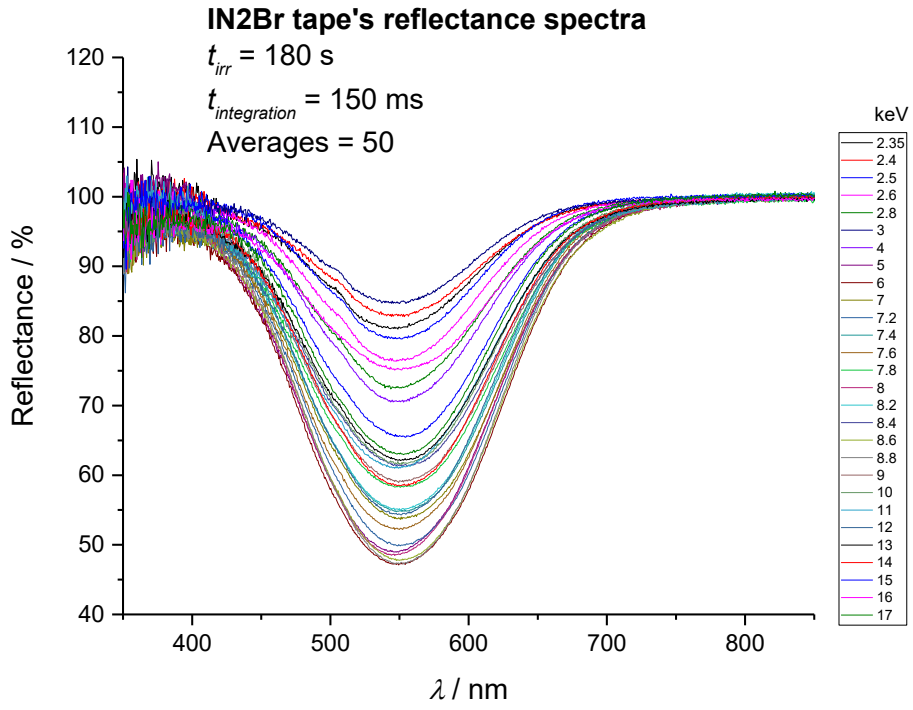

Figure 59. Reflectance spectra measured from the sample tape (Figure 58) after 1 week from the exposures. All the spectra are normalized to 100 % reflectance at 850 nm. Unexposed part of the tape next to the exposed part was used as the white reference.

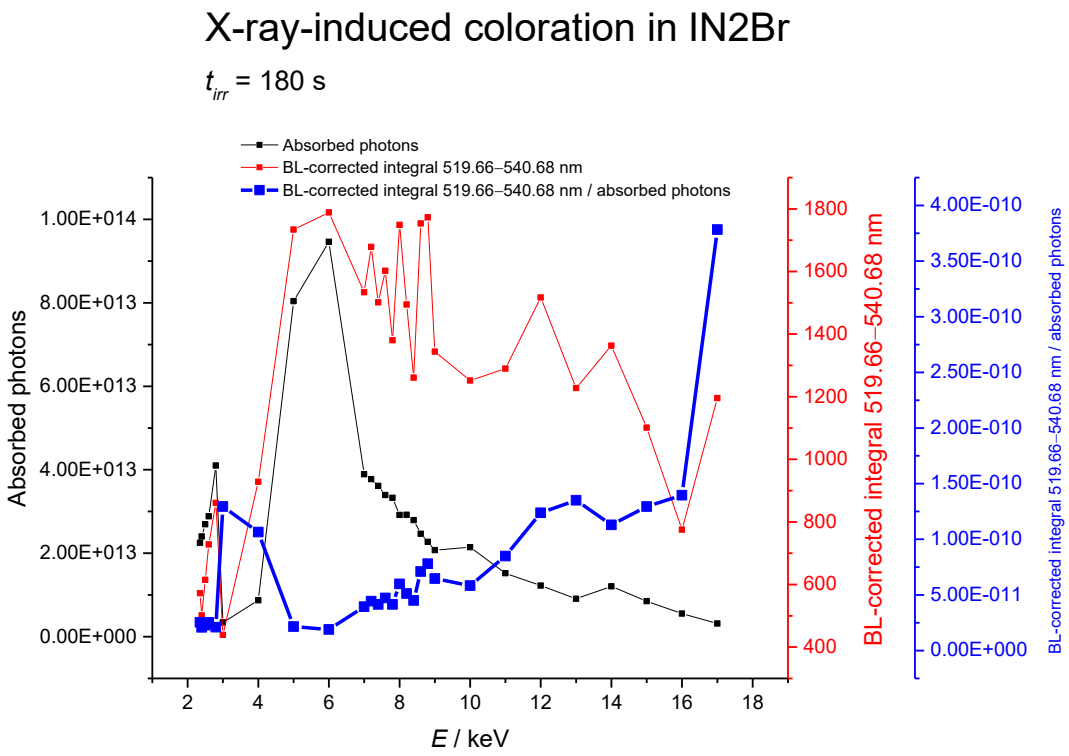

Figure 60. The coloration efficiency of the X-ray-exposed IN2Br (Figure 58).

3.4.8. XANES measurements

In addition to X-ray coloration studies, X-ray absorption near edge structure (XANES) spectra were run from the samples LiNaHack, IN4CL, NaHack19 and IN2Br. The results are shown in Figure 61, Figure 62 and Figure 63.

According to Figure 61, the sample NaHack19 is dominated by the sulfate species [76] with the absorption peak at 2481.6 eV, which is in accordance with the sample's type, i.e. no reduction. IN4CL and LiNaHack also contain some sulfate, which is possibly because the reduction procedure does not reduce the sulfur species thoroughly at all times.

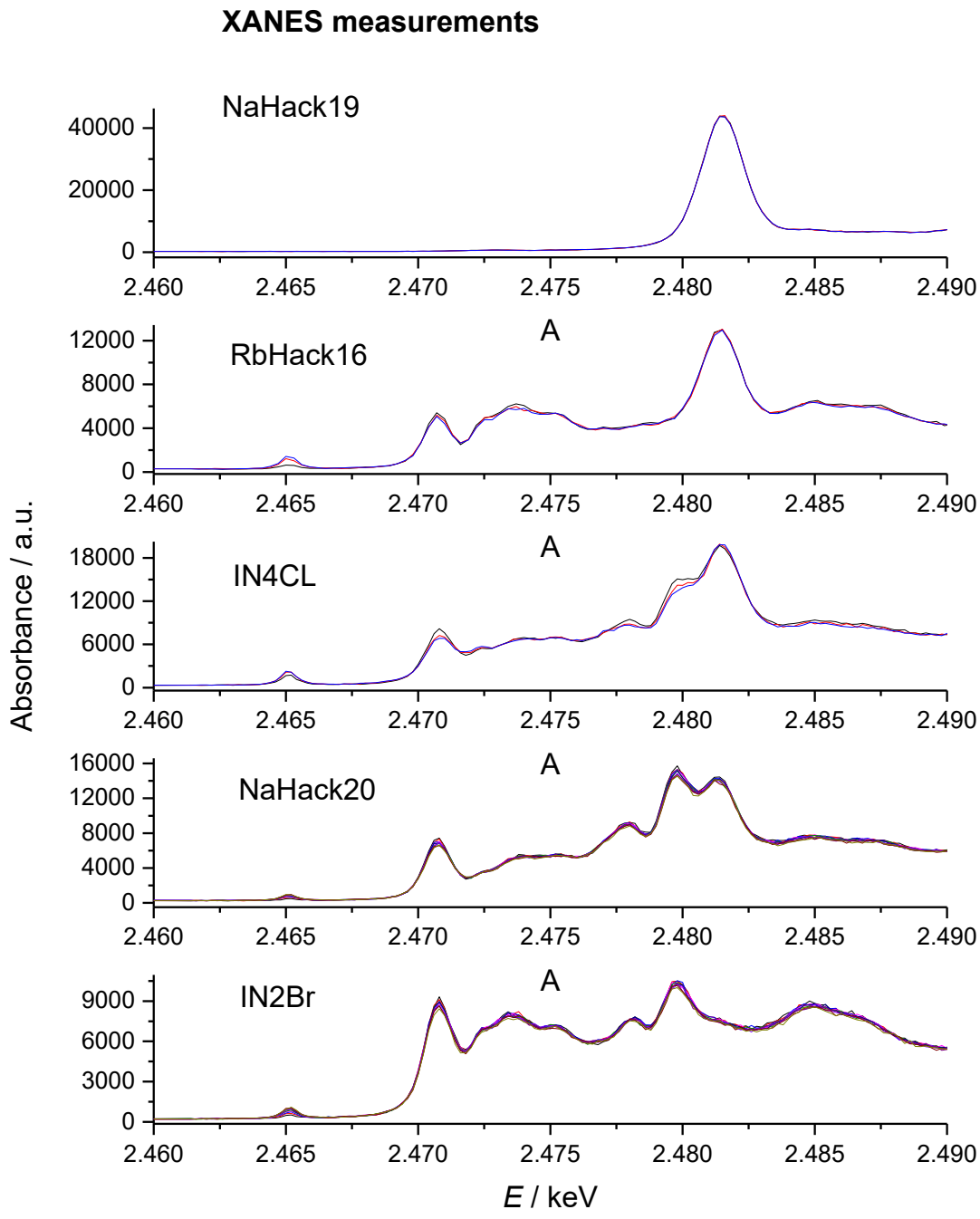

Figure 61. LiNaHack's, IN4CL's, NaHack19's and IN2Br's XANES spectra.

An increasing pre-edge peak manifesting at 2465.2 eV exists in all species except the non-reduced NaHack19. As can be seen from Figure 62, Figure 63, the pre-edge peak grows and saturates, while another peak at 2470.9 eV (Figure 63) decreases.

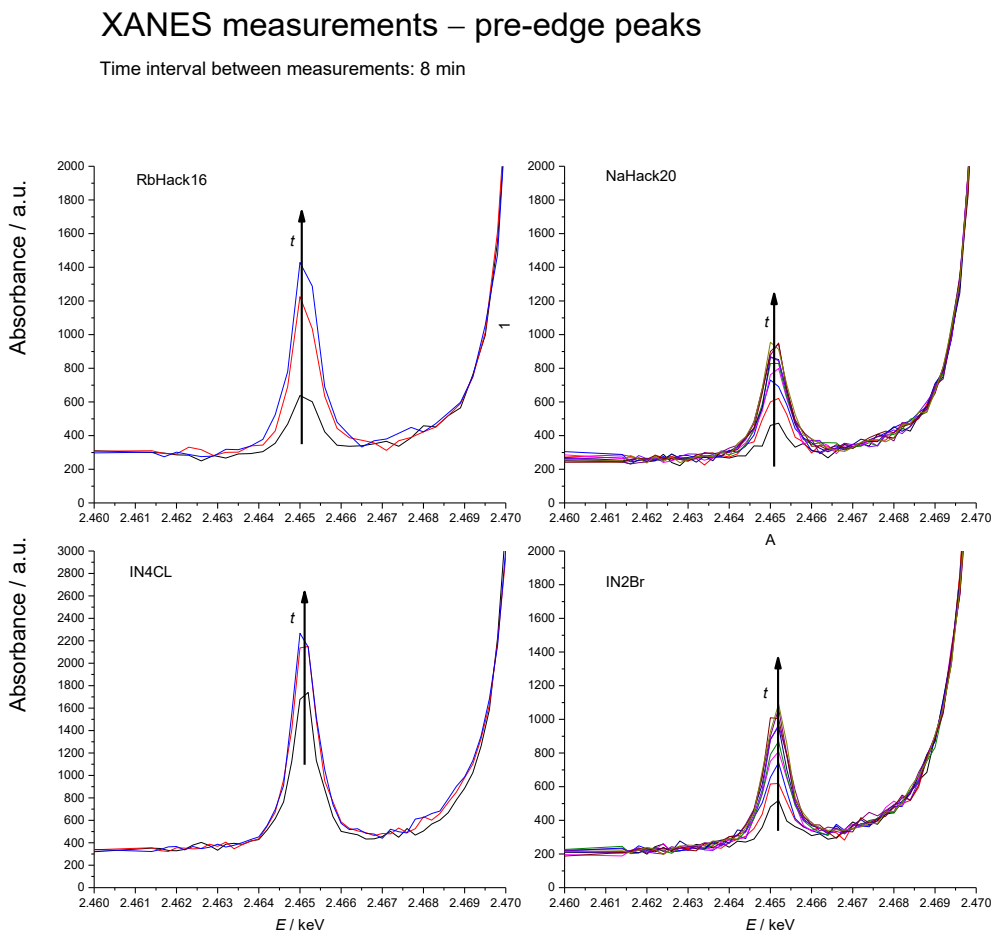

Figure 62. XANES spectra zoomed into the pre-edge region at 2465.2 eV. The pre-edge peak's absorbance grows after each scan.

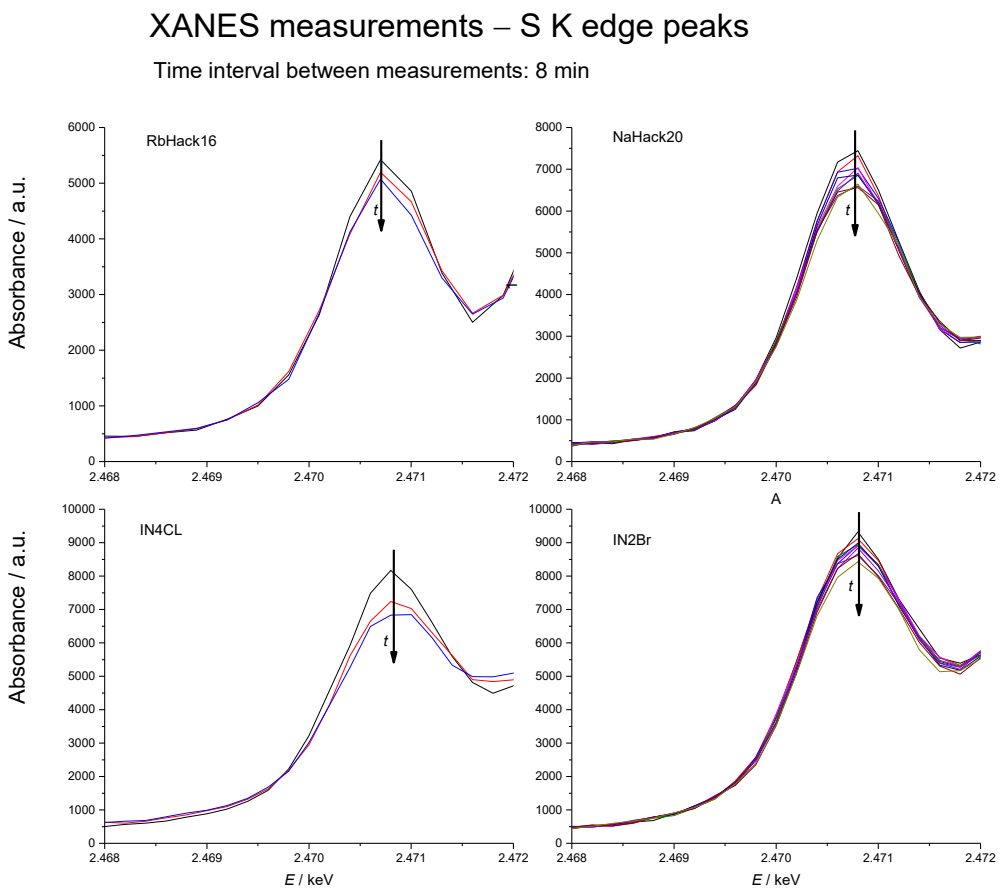

Figure 63. XANES spectra showing the sulfur's K edge peaks at 2470.9 eV. The peaks decrease after each scan.

The increasing of the peak at 2465.2 eV might be caused by the electrons being excited to the traps either from the highest occupied orbital via the highest occupied orbital or directly. The transition probability of the K shell electrons increases as the electrons are excited to the highest occupied orbital band and becomes constant when the occupation is not changing any further: an equilibrium forms with the excited and bleached electrons when visible light is available. [51, 77-79]

The 2470.9 eV peak shows a decrease in intensity. This can be due to the electrons being transferred from the highest occupied orbital to this level, which renders the energy absorption lower.[77]

SeHack14's XANES measurements have been plotted in Figure 64. The figure shows that selenium is present in the material, since selenium's K edge resides at 12.6578 keV [80].

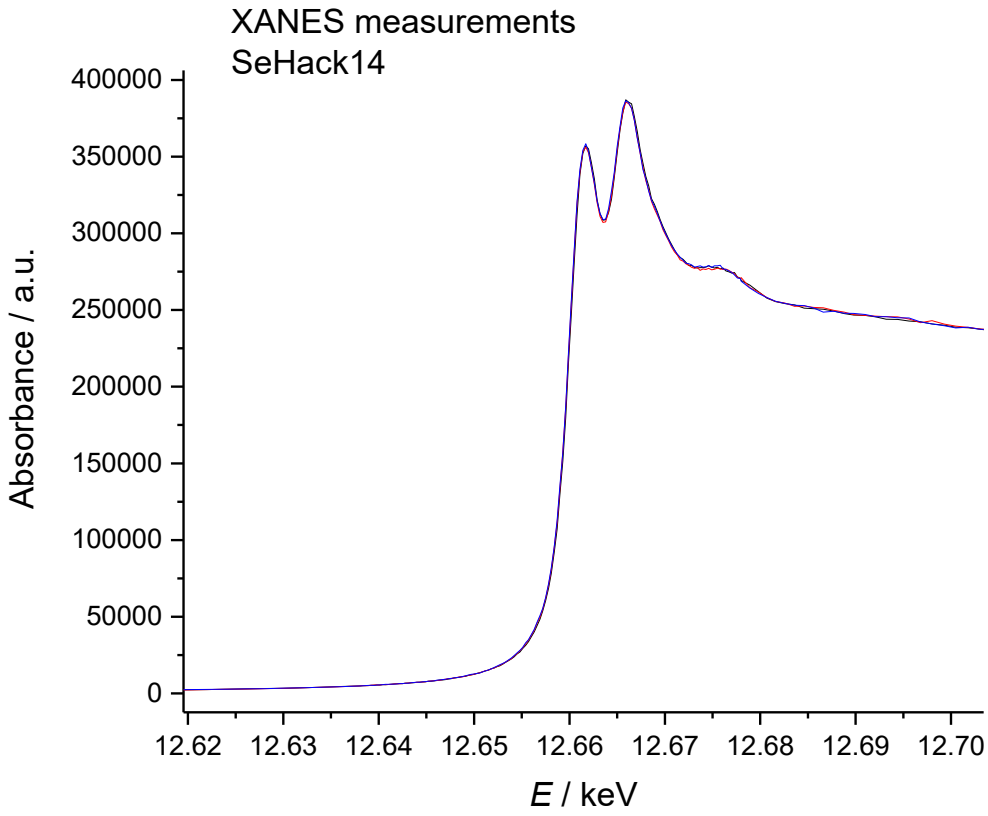

Figure 64. SeHack14's XANES measurements.

3.5. Electron bombardment-induced effects in hackmanites

In addition to X-rays, the hackmanites were exposed to a beam of high-energy electrons with a Nuclide Corp. ELM2EX luminoscope and a Nuclide Corp. ELM2B luminoscope vacuum chamber in University of Turku's Laboratory of Materials Chemistry and Chemical Analysis.

3.5.1. Cathodochromism

For the cathodochromism studies the sample was bombarded with electrons for 1 minute at each voltage from 1 to 11 kV with 1 kV steps and its reflectance spectrum was measured promptly after shutting down the beam. An Avantes AvaSpec-HS-TEC spectrometer was used with an optical fiber Avantes FC-IR600-1-ME-HTX. The light source was Ocean Optics LS-1 Cal and the software was AvaSoft [71] running on Windows 7.

The reflectance spectra shown in Figure 65 show the color deepening with the different voltages. The noise level is rather high, which is due to the cathodoluminescence setup not

allowing to place the optical fiber very close to the sample, and additionally there is a glass separating the sample and the optical fiber because of the vacuum conditions inside the luminoscope.

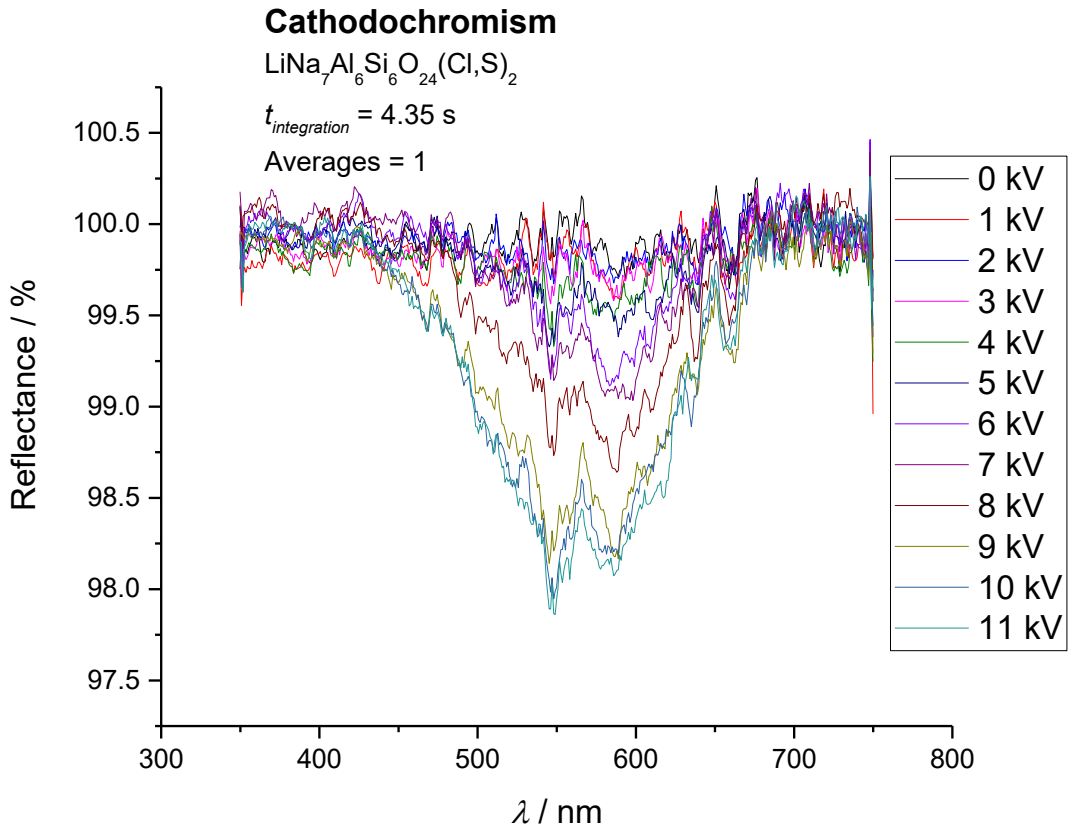

Figure 65. Reflectance measurements during the cathodochromism experiments. Integration time 4.35 s, 1 average per measurement. The spectra are normalized to 100 % reflectance at 700 nm.

After calculating the reflectance spectra's BL-corrected integrals and plotting them against the luminoscope's voltage, it can be seen from Figure 66 that the dependence follows a sigmoidal curve. The fitted line is a guide for the eye, and the results indicate that the dependence is not linear or exponential.

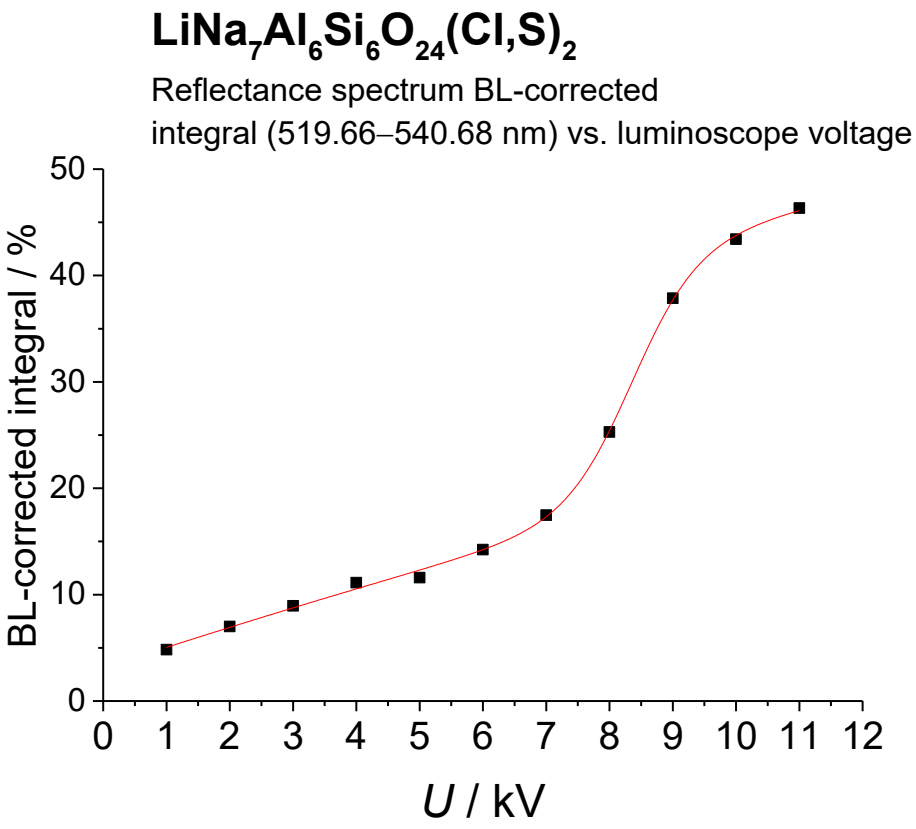

Figure 66. Reflectance spectra's BL-corrected integrals (519.66−540.68 nm) vs. luminoscope voltage. The red line is a guide for the eye.

The luminoscope's current does not behave in a linear fashion when more voltage is applied, thus generating a more intense electron beam at some points and a less intense at some. The available maximum current also changes with the level of vacuum, complicating the experiment's repeatability. By factoring the current with the voltage, a graph shown in Figure 67 can be plotted based on Table 15's data.

Table 15. The cathodochromism results conducted on the luminoscope.

***U* / kV**	***I* / mA**	***P* / W**	**BL-corrected integral 519.66−540.68 nm, pp**
1	0.05	0.05	4.8209
2	0.05	0.10	7.0030
3	0.04	0.12	8.9413

4	0.05	0.20	11.1160
5	0.04	0.20	11.5988
6	0.05	0.30	14.2363
7	0.06	0.42	17.4716
8	0.08	0.64	25.2936
9	0.16	1.44	37.8626
10	0.20	2.00	43.4114
11	0.27	2.97	46.3421

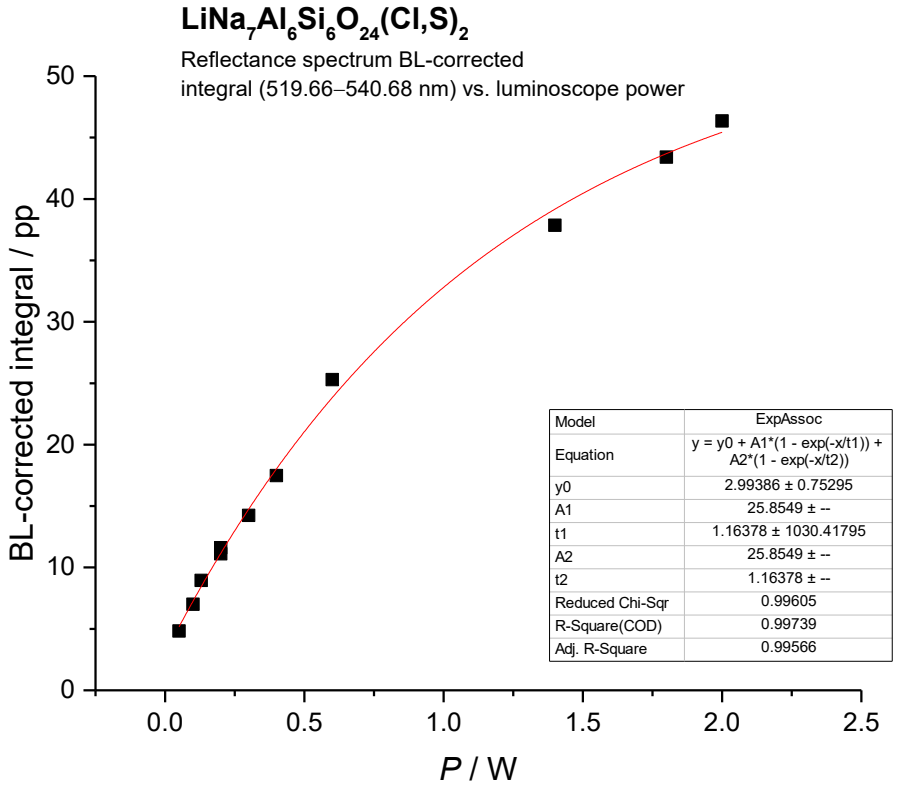

Figure 67. Reflectance spectra's BL-corrected integrals (519.66−540.68 nm) vs. luminoscope power ($P = U_{kV} \cdot I_{mA}$).

Figure 67 is a more likely form of the tenebrescence rise curve than Figure 66. The function saturates at y = 54.7 pp, i.e. at that point an increase in power does not deepen the color any further. The results resemble the ones obtained from the X-ray experiments in section 3.4 and the UV coloration results from the work conducted by Norrbo *et al.* [7].

As shown in Figure 7, some hackmanite samples were successfully colored with the cathodoluminescence setup. All samples were exposed, but only some showed coloration.

The samples that did not show coloration after being exposed to the electron beam did not show coloration with other radiation types either.

3.5.2. Cathodoluminescence

While the cathodochromism-related reflectance spectrum measurements were conducted after shutting down the electron beam with the luminoscope Nuclide Corp. ELM2EX, another study was carried out while the sample was exposed to the electron beam. Both the natural and synthetic hackmanite's cathodoluminescence curves are plotted in Figure 68. The measurements were conducted with an Avantes AvaSpec ULS2048CL-EVO spectrometer coupled with an optical fiber Avantes FC-IR600-1-ME-HTX. The light source was Ocean Optics LS-1 Cal and the software was AvaSoft [71] running on Windows 7.

From Figure 68 can be seen that the 450 nm region is relatively higher in the synthetic one, and also the ascension at 600 nm is present in the synthetic, whereas the natural hackmanite does not show luminescence in that region. Thus, the synthetic species has sites that emit lower-energy photons upon electron bombardment.

The descending level of luminescence during the time series from 1 to 2380 s can be caused by the effect that the traps are saturated with electrons during the bombardment. To rule out the effect of voltage or current increase or decrease on luminescence, the luminoscope's vacuum was allowed to stabilize so that the voltage and current variations would be as low as possible. During the first minutes of the measurements, variations were imperceptible, although from the first measurement to the last, there was detectable, yet elusive crawling of the parameters.

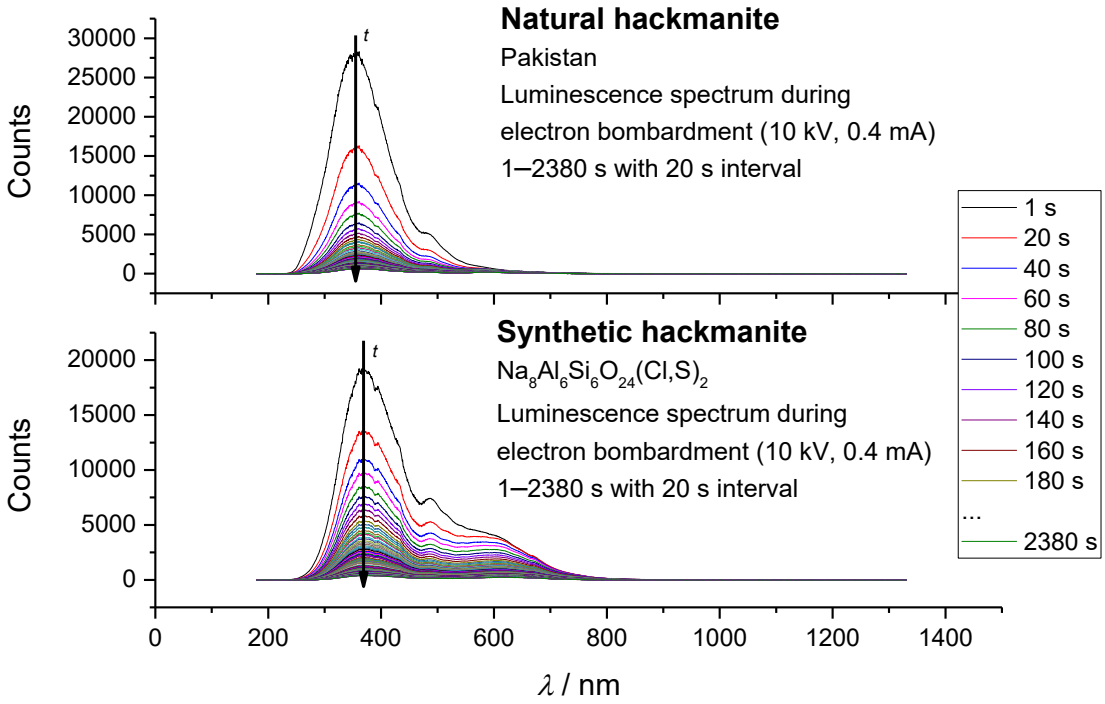

Figure 68. Cathodoluminescence in natural and synthetic hackmanites. The applied voltage was kept at 10 kV and the current at 0.4 mA.

3.6. This chapter is not shown due to non-disclosure obligations

3.7. XPS measurements

To gain more knowledge on the tenebrescence's mechanism and the sulfur species' oxidation states in hackmanite, both a reduced and a non-reduced species irradiated with electron bombardment, X-rays and UV radiation were sent to the University of Turku's Department of Physics and Astronomy for the measurements. Non-irradiated species were used as the reference sample. The samples were irradiated with the Luminoscope Nuclide Corp. ELM2EX (electron bombardment), PANalytical Epsilon 1 XRF analyzer (X-ray exposure) and 5W UVP UVM-57 Handheld UV Lamp 302 nm for at least 3 hours to make the samples colored. All except the UV-exposed unreduced hackmanite showed coloration.

The complete XPS spectrum's shift relative to others is an artifact, which is due to the variations between the samples' electric charges. The charge differences may be caused by

packing differences of the hackmanite crystals in the equipment's sample holder or the samples' ability to discharge.

3.7.1. Reduced hackmanite: electrons, X-rays and UV

The first XPS measurements were conducted on the non-irradiated, electron-bombarded, X-ray-exposed and UV-exposed reduced hackmanite, shown in Figure 69. The results indicate that upon tenebrescence some of the binding energy shifts from the S^{4+} region to the S^{6+} region, meaning that the coloration process consumes electrons in sulfur. The electrons are promoted to the chloride vacancies to form the F center.

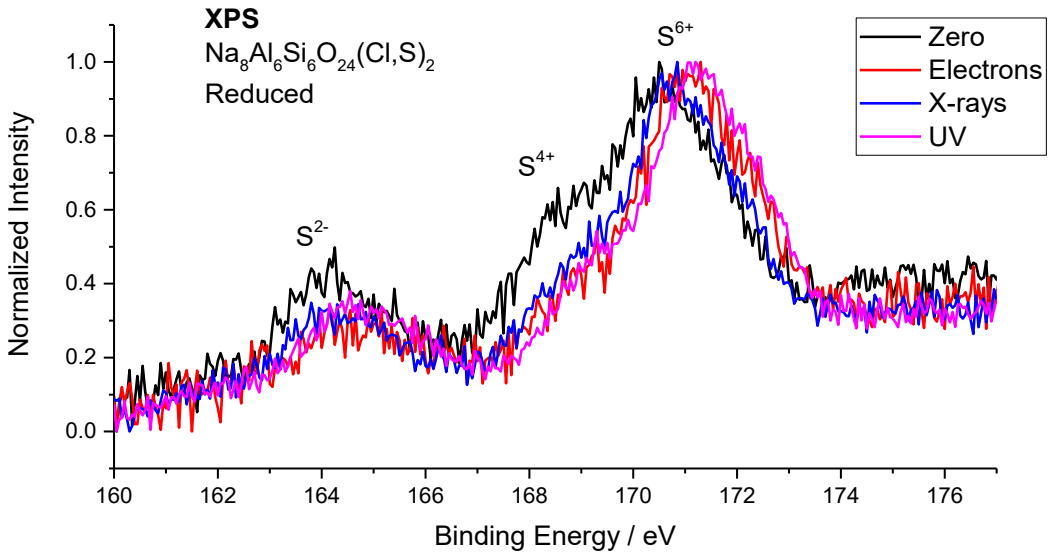

Figure 69. XPS spectra for the non-irradiated, electron-bombarded, X-ray-exposed and UV-exposed reduced hackmanite.

3.7.2. Non-reduced hackmanite: electrons, X-rays and UV

The non-reduced hackmanite samples' XPS spectra are shown in Figure 70. Apart from the shifts caused by the electric charge differences between the samples, there are no noticeable differences between the spectra.

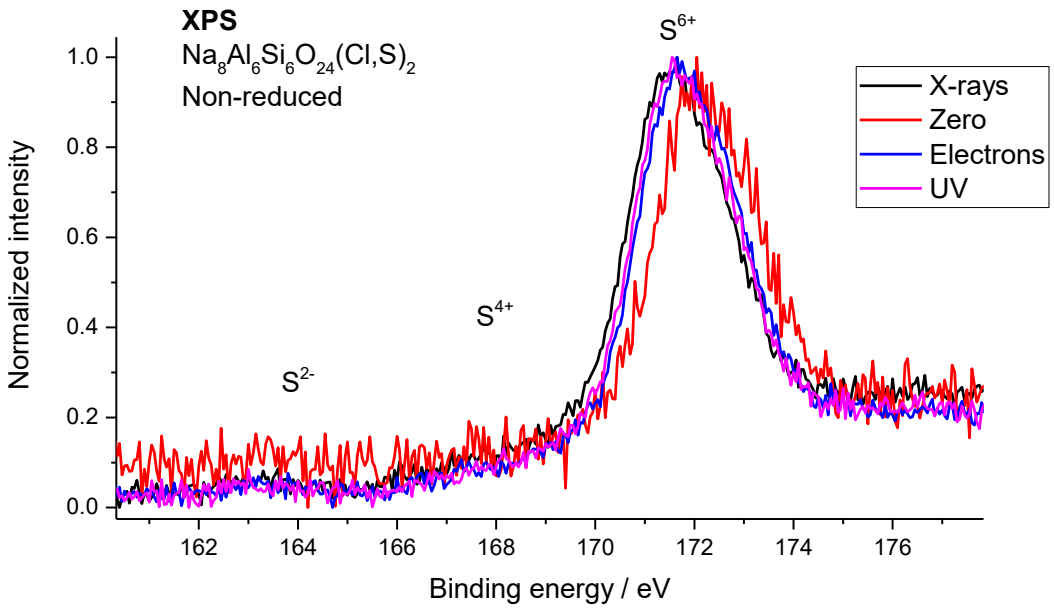

Figure 70. XPS spectra for the non-irradiated, electron-bombarded, X-ray-exposed and UV-exposed non-reduced hackmanite.

3.7.3. This chapter is not shown due to non-disclosure obligations

3.8. This chapter is not shown due to non-disclosure obligations

4. Conclusions and future research ideas

The tape casting process proved to provide an easily manageable and worthwhile medium to study the radiation-induced effects in hackmanites. Handling the tapes was facile and a surprising effect was to notice that the tenebrescence color in this form is deeper than the original powder.

The powder in the tape can be regained by heating the tape to 500 °C. This treatment however has a negative effect on the coloration, and if the tape is heated to 850 °C, the tenebrescence ability is lost completely. This may be due to lattice-related reasons or sulfur leaving the material, which could be validated with a thermogravimeter coupled with a gas analyzer.

The X-ray-induced effects in hackmanite were measured quantitatively, and the most important result was that in every sample the coloration efficiency rises with the photon energy, but considering the amount of photon energy, the coloration efficiency is more uneconomical to UV light. While the coloration can be induced with X-rays, the match in energy levels compared to UV light is inferior. X-ray exposure also exhibits an overexposure effect, in which the coloration fades and eventually can no longer be achieved with exposure to radiation. According to the micro-XRF results the elemental composition does not change in the whiter spot so e.g. X-ray-generated heat-related effects in the organic phase of the tape may be responsible for the overexposure whiteness.

The sulfur K-edge region (2.4720 keV) did not seem to play a role in the coloration efficiency, i.e. the tenebrescence did not show any special characteristics on either side of the K-edge.

Hackmanite with sulfur replaced with selenium shows tenebrescence ability according to the X-ray exposure tests conducted at KIT. More studies are needed to evaluate the properties in more detail in this species of sodalite.

Hackmanite's cathodochromic and cathodoluminescent properties were expertimented with a luminoscope. The coloration shows a logical non-linear curve when exposed to an electron beams with different powers.

The project focused on effects done to hackmanite by several types of radiation. Although some of the results are disappointing in a practical aspect, this thesis founded a basis for a lot of study in the future. Many questions arose and remain unanswered until further studies are conducted. For all we know, hackmanites are a promising and exciting group of materials for future applications.

References

1. Gaft, M., Reisfeld, R., Panczer, G., Modern Luminescence Spectroscopy of Minerals and Materials, Springer International Publishing, Switzerland, 2015.

2. Warner, T. E., Artificial Hackmanite $Na_8[Al_6Si_6O_{24}]Cl_{1.8}S_{0.1}$ by a Structure-Conversion Method with Annealing Under a Reducing Atmosphere, John Wiley & Sons, Ltd, West Sussex, UK, 2011, 240–253.

3. Allan, R., Manual of Mineralogy, Longman, Rees, Orme, Brown, Green & Longman, London, UK, 1834.

4. Baur, W., X. Fischer, R., A historical note on the sodalite framework: The contribution of Frans Maurits Jaeger, *Microporous and Mesoporous Materials,* **116,** 2008, 1–3.

5. Norrbo, I., Gluchowski, P., Hyppänen, I., Laihinen, T., Laukkanen, P., Mäkelä, J., Mamedov, F., Santos, H. S., Sinkkonen, J., Tuomisto, M., Viinikanoja, A., Lastusaari, M., Mechanisms of Tenebrescence and Persistent Luminescence in Synthetic Hackmanite $Na_8Al_6Si_6O_{24}(Cl,S)_2$, *ACS applied materials & interfaces,* **8,** 2016, 11592–11602.

6. Norrbo, I., Carvalho, J. M., Laukkanen, P., Mäkelä, J., Mamedov, F., Peurla, M., Helminen, H., Pihlasalo, S., Härmä, H., Sinkkonen, J., Lastusaari, M., Lanthanide and Heavy Metal Free Long White Persistent Luminescence from Ti Doped Li–Hackmanite: A Versatile, Low-Cost Material, *Advanced Functional Materials,* **27,** 2017, 1606547.

7. Norrbo, I., Curutchet, A., Kuusisto, A., Mäkelä, J., Laukkanen, P., Paturi, P., Laihinen, T., Sinkkonen, J., Wetterskog, E., Mamedov, F., Le Bahers, T., Lastusaari, M., Solar UV index and UV dose determination with photochromic hackmanites: From the assessment of the fundamental properties to the device, *Materials Horizons,* **5,** 2018.

8. International Union of Pure and Applied Chemistry, IUPAC Gold Book – radiation, 2014, URL: https://goldbook.iupac.org/html/R/R05048.html, retrieved May 24, 2019.

9. Wald, L., Solar radiation energy (fundamentals), Encyclopedia of Life Support Systems (EOLSS), Developed under the Auspices of the UNESCO, Eolss Publishers, Oxford, UK, 2007.

10. Chen, W., Gan, W., The Calculation of Solar Gamma-Rays by TALYS, *Chinese Astronomy and Astrophysics,* **36,** 2012, 49–62.

11. Visscher, M. O., Bailey, J. K., Hom, D. B., Scar Treatment Variations by Skin Type, *Facial Plastic Surgery Clinics of North America,* **22,** 2014, 453–462.

12. Meredith, P., Riesz, J., Radiative Relaxation Quantum Yields for Synthetic Eumelanin, *Photochemistry and Photobiology,* **79,** 2004, 211–216.

13. WHO, Skin cancers, 2018, URL: http://www.who.int/uv/faq/skincancer/en/index1.html, retrieved November 9, 2018.

14. Obodovskiy, I., Radiation: Fundamentals, Applications, Risks and Safety, Elsevier, Frankfurt, Germany, 2019, 447–471.

15. Kramar, U., X-Ray Fluorescence Spectrometers, **3,** Elsevier, Oxford, UK, 2010.

16. Ahmed, S. N., Physics and Engineering of Radiation Detection, Elsevier, 2015, 1–64.

17. Sprawls, P., The Physical Principles of Medical Imaging, **2**, Medical Physics Publishing, Madison, USA, 1995.

18. NDT, Sources of Attenuation, 2014, URL: https://www.nde-ed.org/EducationResources/CommunityCollege/Radiography/Physics/attenuation.htm, retrieved Jun 9, 2019.

19. Nave, R., Compton Scattering, 2017, URL: http://hyperphysics.phy-astr.gsu.edu/hbase/quantum/comptint.html, retrieved Jun 7, 2019.

20. Huda, W., Slone, R. M., Review of Radiologic Physics, Lippincott Williams & Wilkins, Philadelphia, USA, 2003.

21. Kónya, J., Nagy, N. M., Chapter 5 – Interaction of Radiation With Matter, Elsevier, Madison, USA, 2018, 85–131.

22. Knoll, G. F., Radiation Detection and Measurement, John Wiley & Sons, USA, 2010.

23. L'Annunziata, M. F., Radioactivity, Elsevier B.V., USA, 2007.

24. Canadian Nuclear Society, Smoke detectors and americium-241 fact sheet, 2008, URL: https://cns-snc.ca/media/pdf_doc/ecc/smoke_am241.pdf, retrieved May 13, 2019.

25. Australian Radiation Protection and Nuclear Safety, Beta particles, 2017, URL: https://www.arpansa.gov.au/understanding-radiation/what-is-radiation/ionising-radiation/beta-particles, retrieved May 27, 2019.

26. Gay, T. J., 6 – Sources of Metastable Atoms and Molecules, **29,** Academic Press, New York, USA, 1996, 95–114.

27. Trajmar, S., Nickel, J. C., Cross-Section Measurements for Electron Impact on Excited Atomic Species, **30,** Academic Press, New York, USA, 1992, 45–103.

28. Massey, H. S. W., Bates, D. R., Applied Atomic Collision Physics, Academic Press, New York, USA, 1982.

29. Harvey, K. C., Slow metastable atomic hydrogen beam by optical pumping, *Journal of Applied Physics,* **53,** 1982, 3383–3386.

30. National Aeronautics and Space Administration, Science Mission Directorate, Tour of the Electromagnetic Spectrum: Gamma Rays, 2010, URL: https://science.nasa.gov/ems/12_gammarays, retrieved May 23, 2019.

31. Obodovskiy, I., Fundamentals of Radiation and Chemical Safety, Elsevier, Netherlands, 2015.

32. Richter, J. R., Kasten, B. B., Zinn, K. R., Adenoviral Vectors for Gene Therapy, Academic Press, San Diego, USA, 2016, 767–802.

33. Sandle, T., Sterility, Sterilisation and Sterility Assurance for Pharmaceuticals, Woodhead Publishing, New Delhi, India, 2013, 55–68.

34. Shalek, R. J., Dosimetry of X-Ray and Gamma-Ray Beams for Radiation Therapy in the Energy Range 10 keV to 50 MeV, National Council on Radiation Protection and Measurements, Bethesda, USA, 1981.

35. Halperin, A., Handbook on the Physics and Chemistry of Rare Earths: Activated thermoluminescence (TL) dosimeters and related radiation detectors, **28,** Elsevier, Oxford, UK, 2000, 187–309.

36. Kozicki, M., Sąsiadek, E., Kadłubowski, S., Dudek, M., Maras, P., Nosal, A., Gazicki-Lipman, M., Flat foils as UV and ionising radiation dosimeters, *Journal of Photochemistry and Photobiology A: Chemistry,* **351,** 2018, 179–196.

37. Chen, R., Pagonis, V., Thermally and Optically Stimulated Luminescence: A Simulation Approach, Wiley, West Sussex, UK, 2011.

38. Visocekas, R., Tunnelling in afterglow, its coexistence and interweaving with thermally stimulated luminescence, *Radiat Prot Dosimetry,* **100,** 2002, 45–54.

39. Kortov, V., Materials for thermoluminescent dosimetry: Current status and future trends, *Radiation Measurements,* **42,** 2007, 576–581.

40. Dong, H., Zhu, H., Meng, Q., Gong, X., Hu, W., Organic photoresponse materials and devices, *Chem Soc Rev,* **41,** 2012, 1754–1808.

41. Irie, M., Fukaminato, T., Matsuda, K., Kobatake, S., Photochromism of Diarylethene Molecules and Crystals: Memories, Switches, and Actuators, *Chem. Rev.,* **114,** 2014, 12174–12277.

42. Armstrong, J. A., Weller, M. T., Structural observation of photochromism, *Chem. Commun.,* 2006, 1094–1096.

43. McGarvey, D. J., Photochromism in view, 2008, URL: https://eic.rsc.org/feature/photochromism-in-view/2020209.article, retrieved May 23, 2019.

44. Zheng, H., Ou, J. Z., Strano, M. S., Kaner, R. B., Mitchell, A., Kalantar-zadeh, K., Nanostructured Tungsten Oxide – Properties, Synthesis, and Applications, *Advanced Functional Materials,* **21,** 2011, 2175–2196.

45. He, T., Yao, J., Photochromism of molybdenum oxide, *Journal of Photochemistry and Photobiology C-photochemistry Reviews,* **4,** 2003, 125–143.

46. Songara, S., Patra, M. K., Manoth, M., Saini, L., Gupta, V., Gowd, G. S., Vadera, S. R., Kumar, N., Synthesis and studies on photochromic properties of vanadium doped TiO2 nanoparticles, *Journal of Photochemistry and Photobiology A: Chemistry,* **209,** 2010, 68–73.

47. Jin, A., Chen, Z., Wang, M., Guo, G., [$Zn(OOCH)_2$(4,4′-bipyridine)]n: A metal-organic-framework (MOF) with x-ray-induced photochromic behaviour at room temperature, *Dyes and Pigments,* **163,** 2019, 656–659.

48. Kiss, Z. J., Phillips, W., Cathodochromism in Photochromic Materials, *Physical Review,* **180,** 1969.

49. Ouseph, P. J., Groskreutz, H. E., Photochromic materials as radiation detectors, *Nuclear Instruments and Methods,* **113,** 1973, 469–471.

50. Williams, E. R., Simmonds, A., Armstrong, J. A., Weller, M. T., Compositional and structural control of tenebrescence, *Journal of Materials Chemistry,* **20,** 2010, 10883–10887.

51. Medved, D. B., Hackmanite and its tenebrescent properties, *American Mineralogist,* **39,** 1954, 615–629.

52. Hassan, I., Grundy, H. D., Handbook of Mineralogy, 1983.

53. Hassan, I., Antao, S., B. Parise, J., Sodalite: High-temperature structures obtained from synchrotron radiation and Rietveld refinements, *Mineralogical Magazine,* **68,** 2004.

54. Reinen, D., Lindner, G., The nature of the chalcogen colour centres in ultramarine-type solids, *Chemical Society Reviews,* **28,** 1999, 75–84.

55. Darvell, B. W., Chapter 24 – Light and Colour, Elsevier, Duxford, UK, 2018, 596–632.

56. Tedesco, C., Brunelli, M., 2.04 – X-ray Powder Diffraction, Elsevier, Oxford, UK, 2017, 45–73.

57. Toney, M. F., 4.1 – XRD: X-Ray Diffraction, Elsevier, Boston, USA, 1992, 198–213.

58. Iwashita, N., Chapter 2 – X-ray Powder Diffraction, Elsevier, Boston, USA, 2016, 7–25.

59. Aziz, M., Ismail, A. F., Chapter 5 – X-Ray Photoelectron Spectroscopy (XPS), Elsevier, Amsterdam, Netherlands 2017, 81–93.

60. Boffito, D. C., Neagoe, C., Cerrato, G., Boffito, C., Chiarello, G. L., Bianchi, C. L., Rigamonti, M. G., Benamer, A., Patience, G. S., Chapter 11 – Spectroscopy, Elsevier, Amsterdam, Netherlands, 2018, 339–383.

61. Zhang, M., XANES: Theory, 2013, URL: https://chem.libretexts.org/Bookshelves/Physical_and_Theoretical_Chemistry_Textbook_Maps/Supplemental_Modules_(Physical_and_Theoretical_Chemistry)/Spectroscopy/X-ray_Spectroscopy/XANES%3A_Theory, retrieved May 24, 2019.

62. Penner-Hahn, J. E., X-ray Absorption Spectroscopy, John Wiley & Sons, New Jersey, USA, 2005.

63. Kirby, J. A., Goodin, D. B., Wydrzynski, T., Robertson, A. S., Klein, M. P., State of manganese in the photosynthetic apparatus. 2. X-ray absorption edge studies on manganese in photosynthetic membrane, *J. Am. Chem. Soc.,* **103,** 1981, 5537–5542.

64. Shulman, G. R., Yafet, Y., Eisenberger, P., Blumberg, W. E., Observations and interpretation of x-ray absorption edges in iron compounds and proteins, *PNAS,* **73,** 1976, 1384–1388.

65. Twiname, E. R., Mistler, R. E., Tape Casting and Lamination, Elsevier, Oxford, UK, 2001, 9083–9088.

66. Kumari, K., Sasidharan, K., Sapna, M., Natarajan, R., Dispersion and rheological studies of Y-PSZ tape casting slurry, *Bull Mater Sci,* **28,** 2005, 103–108.

67. Abhinay, S., Mazumder, R., Seal, A., Sen, A., Tape casting and electrical characterization of $0.5Ba(Zr_{0.2}Ti_{0.8})O_3–0.5(Ba_{0.7}Ca_{0.3})TiO_3$ (BZT–0.5BCT) piezoelectric substrate, *Journal of the European Ceramic Society,* **36,** 2016, 3125–3137.

68. Descamps, M., Ringuet, G., Leger, D., Thierry, B., Tape-casting: Relationship between organic constituents and the physical and mechanical properties of tapes, *Journal of the European Ceramic Society,* **15,** 1995, 357–362.

69. Li, H., Epelbaum, E., Batentschuk, M., Winnacker, A., Tape casting of storage phosphor $BaFBr:Eu^{2+}$ for X-ray imaging, *Materials Science & Engineering B,* **96,** 2002, 313–319.

70. TA Instruments, Universal Analysis 2000 **v4.5A,** 2007.

71. Avantes, AvaSoft **v8.7.1.0,** 2017.

72. Huber, Guinier G670 Data Acquisition Program **v4.0 build 30,** 2001.

73. Karlsruhe Institute of Technology, Test Facility and Synchrotron Radiation Source at KIT: Beamlines, 2016, URL: https://www.anka.kit.edu/766.php, retrieved May 20, 2019.

74. Karlsruhe Institute of Technology, Institute for Beam Physics and Technology (IBPT): Accelerator, 2017, URL: http://www.ibpt.kit.edu/1712.php, retrieved May 20, 2019.

75. Smoot, G. F. X-ray Test Facility Calculation, URL: https://www.exul.ru/education/1/30.pdf, retrieved May 20, 2019.

76. Almkvist, G., Boye, K., Persson, I., K-edge XANES analysis of sulfur compounds: an investigation of the relative intensities using internal calibration, *Journal of synchrotron radiation,* **17,** 2010, 683–688.

77. Göttlicher, J., email, Some S K XANES spectra, Oct 11, 2018.

78. Curutchet, A., Le Bahers, T., Modeling the Photochromism of S-Doped Sodalites Using DFT, TD-DFT, and SAC-CI Methods, *Inorganic chemistry,* **56,** 2017, 414–423.

79. Goettlicher, J., Kotelnikov, A., Suk, N., Kovalski, A., Vitova, T., Steininger, R., Sulfur K X-ray absorption near edge structure spectroscopy on the photochrome sodalite variety hackmanite, **228,** 2013, 157–171.

80. Merritt, E. A., X-ray Absorption Edges, 2010, URL: http://skuld.bmsc.washington.edu/scatter/AS_periodic.html, retrieved May 26, 2019.

81. Mikrolab, TLD Reader/Analyser **v0.9.401,** 2001.

82. Konica Minolta, SpectraMagic™ DX **v1.22.0004,** 2018.

83. Nikon®, Capture NX-D **v1.5.2,** 2014.

84. Jasc®, Paint Shop Pro™ **v7.00,** 2000.

85. FlukeView®, FlukeView® Forms **v3.8.0003,** 2014.